Spring 5-5-2018

Molecular Mechanism of Early Amyloid Self-Assembly Revealed by Computational Modeling

Mohtadin Hashemi
University of Nebraska Medical Center

Follow this and additional works at: https://digitalcommons.unmc.edu/etd

   Part of the Biochemistry Commons, Biophysics Commons, Computational Neuroscience Commons, and the Structural Biology Commons

MOLECULAR MECHANISM OF EARLY AMYLOID SELF-ASSEMBLY REVEALED BY COMPUTATIONAL MODELING

by

Mohtadin Hashemi

A DISSERTATION

Presented to the Faculty of

the University of Nebraska Graduate College

in Partial Fulfillment of the Requirements

for the Degree of Doctor of Philosophy

Pharmaceutical Sciences Graduate Program

Under the Supervision of Professor Yuri L. Lyubchenko

University of Nebraska Medical Center

Omaha, Nebraska

April, 2018

Supervisory Committee:

Howard E. Gendelman, M.D.   Alexey V. Krasnoslobodtsev, Ph.D.

Luis A. Marky, Ph.D.   Simon Sherman, Ph.D.

Dedicated to my mother,

"Her hands held me gently from the day I took my first breath.

Her hands helped to guide me as I took my first step.

Her hands held me close when the tears would start to fall.

Her hands were quick to show me that she would take care of it all"

Dedikeret til min mor,

"Det første billede af en engel man ser,

er det samme som et billede af mor der ler.

Det er mor der redder en fra drømme i den mørke nat

fordi hendes børn er hendes mest værdifulde skat.

Det er hende der guider og beskytter

og hende der vejleder og lytter"

تقدیم به مادرم، دریای بی‌کران از فداکاری و مهر:

اول به هزار لطف بنواخت مرا

آخر به هزار غصه بگداخت مر

چون مهره مهر خویش می‌باخت مرا

چون من همه از شدم بینداخت مر

ACKNOWLEDGEMENTS

My thanks are also extended to current and former faculty members and my fellow students for their patience and help through my PhD study. I would like to acknowledge Ashley Calhoon, Jamie Cook, Renee Kaszynski, Michelle Parks, Elaine Payne, and Katina Winters from the College of Pharmacy and Cody Phillips, Terri Vadovski, and Vanessa Wilcox from Graduate Studies for their assistance with all administrative aspects of my education.

I would like to thank David Swanson and his team at the Holland Computing Center for advice and training with regards to the NU supercomputers. I am grateful towards Phillip Blood, Markus Dittrich, and Marcela Madrid and their colleagues at the Pittsburg Supercomputing Center for training and advice on the special purpose supercomputer Anton and Anton2.

I would like to acknowledge the NSF and NIH funding sources for making my research possible. Furthermore, I would like to thank the UNMC Graduate Assistantship, Bukey memorial fellowship, and the UNMC Graduate Fellowship for providing financial support during my research.

Above all, I would like to thank my family for their endless patience and support; for taking time out of their busy lives to help me with any issue that arose, and for sharing their joy and happiness during the times I needed it the most. I am indebted to my wife for her endless and unconditional support, encouragement, love, and the many sacrifices she has made; she is the wind that carries my dinghy through the journey that is life.

The simulations in this dissertation were performed using my personal μ–cluster; Crane and Tusker at Holland Computing Center of the University of Nebraska, which receives support from the Nebraska Research Initiative; Comet at San Diego Supercomputer Center and Stampede at the Texas Advanced Computing Center, through the Extreme Science and Engineering Discovery Environment (supported by National Science Foundation ACI-1053575 for XSEDE); and the special purpose supercomputers Anton and Anton2, provided by the Pittsburgh Supercomputing Center through Grant R01GM116961 from the National Institutes of Health. Anton machines at PSC were generously made available by D.E. Shaw Research.

Some passages in this dissertation have been quoted, with permission, verbatim from the following sources: DOI: 10.1039/c6nr06850b, DOI:10.1038/s41598-017-02454-0, DOI: 10.1038/srep45592, and DOI: 10.1101/295782.

MOLECULAR MECHANISM OF EARLY AMYLOID SELF-ASSEMBLY REVEALED BY COMPUTATIONAL MODELING

Mohtadin Hashemi, Ph.D.

University of Nebraska Medical Center, 2018

Supervisor: Yuri L. Lyubchenko, Ph.D., D.Sc.

Protein misfolding followed by the formation of aggregates, is an early step in the cascade of conformational changes in a protein that underlie the development of several neurodegenerative diseases, including Alzheimer's and Parkinson's diseases. Efforts aimed at understanding this process have produced little clarity and the mechanism remains elusive.

Here, we demonstrate that the hairpin fold, a structure found in the early folding intermediates of amyloid β, induces morphological and stability changes in the aggregates of Aβ(14-23) peptide. We structurally characterized the interactions of monomer and hairpin using extended molecular dynamics (MD) simulations, which revealed a novel intercalated type complex. These finding suggest that folding patterns of amyloid proteins define the aggregation pathway.

Computational analysis was then used to characterize the dimerization of full-length Aβ peptide and reveal their dynamic properties. Aβ dimers did not show β-sheet structures, as one may expect based on the known structures of Aβ fibrils, rather dimers are stabilized by hydrophobic interactions in the central hydrophobic regions. Comparison

between Aβ40 and Aβ42 showed that overall, the dimers of both alloforms exhibit similar interaction strengths. However, the interaction patterns are significantly different.

A novel aggregation pathway, able to describe aggregation at physiologically relevant concentrations, was elucidated when aggregation of amyloid proteins was performed in presence of surfaces. Computational analysis revealed that interaction of a monomer with the surface is accompanied by the structural transition of the monomer; which can then facilitate binding of another monomer and form a dimer. Compared to our previous data we observed an almost five-fold faster dimer formation.

Further investigation of the surface-mediated aggregation revealed that lipid membranes promote aggregation of α-syn protein. MD simulations demonstrate that α-syn monomers change conformation upon interaction with the bilayers. On POPS, α-syn monomer protrudes from the surface. This conformation on POPS dramatically facilitates assembly of a dimer that remains stable over the entire simulation period. These findings are in line with experimental data.

Overall, the studies described in this thesis provide the structural basis for the early stages of the misfolding and aggregation process of amyloid proteins.

CONTENTS

LIST OF FIGURES

LIST OF ABBREVIATIONS AND ACRONYMS

Aβ	Amyloid β
AD	Alzheimer's disease
AFM	Atomic force microscopy
aMD	Accelerated molecular dynamics
AMBER	Assisted model building with energy refinement
APP	Amyloid precursor protein
APS	1-(3-Aminopropyl)silatrane
α-Syn	α-Synuclein
CD	Circular dichroism
CG	Coarse grained
cMD	Conventional molecular dynamics
CoM	Center-of-mass
DLPE	1,2- didodecanoyl-sn-glycero-3-phosphoethanolamine
dPC	Dihedral principle component
DSSP	Defined secondary structure of protein
FRET	Förster resonance energy transfer
FTIR	Fourier transformed infrared spectroscopy
GROMACS	Groningen machine or chemical simulations

HCC	Holland computing center
HD	Huntington's disease
HS-AFM	High-speed AFM
IDP	Intrinsically disordered protein
INTFF	INTERFACE force field
MC	Monte Carlo
MCP	Monte Carlo pulling
MD	Molecular dynamics
NAC	Non-amyloid component, residues 61-95 of α-syn
NMR	Nuclear magnetic resonance
PBS	Phosphate-buffered saline
PD	Parkinson's disease
PDB	Protein data bank
PME	Particle mesh Ewald
POPC	1-palmitoyl-2-oleoyl-sn-glycero-3-phosphocholine
POPS	1-palmitoyl-2-oleoyl-sn-glycero-3-phospho-L-serine
PSC	Pittsburgh supercomputing center
REMD	Replica exchange molecular dynamics
Rg	Radius of gyration

RMSD   Root mean square deviation

SDSC   San Diego supercomputer center

SLB   Supported lipid bilayer

SMD   Steered molecular dynamics

SPM   Scanning probe microscopy

ssNMR   Solid-state NMR

STD   Standard deviation

TACC   Texas advanced computing center

TAPIN   Tethered approach for probing inter-molecular interactions

TIRF   Total internal reflection fluorescence microscopy

XSEDE   The extreme science and engineering discovery environment

LIST OF CONTRIBUTORS

Chapter 3. Mohtadin Hashemi, Dr. Sibaprasad Maity, and Dr. Yuri L. Lyubchenko conceived and designed the project. Mohtadin Hashemi implemented all simulations and analysis. Dr. Maity performed single-molecule measurements and analysis. The chapter is based on DOI:10.1038/s41598-017-02454-0.

Chapter 4. Mohtadin Hashemi, Dr. Yuliang Zhang, Dr. Zhengjian Lv, and Dr. Lyubchenko conceived and designed the overall study. Mohtadin Hashemi performed all the simulations and analyzed simulation data. Dr. Zhang contributed to validation of simulation data. Dr Lv performed analysis of experimental data. The chapter includes data reproduced from DOI: 10.1039/c6nr06850b, with permission from the Royal Society of Chemistry.

Chapter 5. Dr. Lyubchenko designed the project. Mohtadin Hashemi performed the molecular dynamics analysis; Dr. Maity performed experiments with Aβ(14-23); Dr. Siddhartha Banerjee performed experiments with Aβ(42); and dr. Lv performed experiments with α-synuclein. The chapter is based on DOI: 10.1038/srep45592.

Chapter 6. Mohtadin Hashemi, Dr. Lv, and Dr. Lyubchenko conceived and designed the experiments. Mohtadin Hashemi performed computational analysis. Dr. Lv, Dr. Banerjee, and Karen Zagorski performed AFM studies. Dr. Jean-Christophe Rochet characterized α-synuclein protein. The chapter is based on DOI: 10.1101/295782.

Chapter 1.   INTRODUCTION

Proteins have a wide variety of functions within the cell, including structural, biochemical, and as components in the signaling pathways (1-3). Most proteins assume a fold, and ultimately a structure, in a functional conformation while performing their biological function. However, either during folding, or from an already folded structure, proteins can form a so-called misfolded structure (4). A unique property of misfolded protein conformations is their propensity to self-assemble into nanostructures of various morphologies termed aggregates; this can happen *in vivo* as well as *in vitro* (4-9). Aggregated proteins often lack the biological activity of the correctly folded proteins and are often associated with pathological conditions. In humans these diseases are termed protein aggregation disorders and include Alzheimer's (AD), Parkinson's (PD), and Huntington's diseases (HD) (10-14).

Alzheimer's disease is a fatal chronic neurodegenerative disease, and the most common form of dementia, associated with loss of memory and other cognitive abilities (12, 15-17). Diagnosis of AD is very difficult and usually happens at later stages of the disease through cognitive testing, advanced brain imaging methods, and familial health history. At this stage, major parts of the brain are extensively damaged. In the United States, AD is the sixth leading cause of death and has seen a ~55% increase in death rate from 1999 to 2014 (18).

Recent data shows that approximately 5.2 million Americans suffer from AD (18), accounting for a significant fraction of global AD patients, approximately 46 million (19). The incidence of AD is expected to increase dramatically in the next decade, primarily because of the aging population and the fact that prevalence of neurodegenerative disorders, including AD, increase with age. The medical care provided for American AD patients alone are estimated to cost $226 billion *per annum*, with 68% paid by Medicare and Medicaid (20). With the dramatic increase in number of patients and the cost of care, a frantic search for interventions is ongoing. However, all efforts so far have failed; there is no treatment to arrest or reverse the progression of AD, there is no cure.

1.1 Amyloid Aggregation Progression

Alzheimer's disease is associated with the spontaneous self-assembly and aggregation of amyloid β proteins (21). These aggregates form large insoluble inclusions within the AD brain, called amyloid plaques, and are the pathological hallmarks of the disease (15, 22). Amyloid β is the byproduct of proteolytic cleavage of amyloid precursor protein (APP) when processed by β- and γ-secretases (23). There are two principle alloforms of amyloid β proteins, Aβ40 and Aβ42, defined by the number of residues; with the former being the most abundant and the latter the most aggregation prone and neurotoxic (16, 24-29). The amyloid cascade hypothesis implicates the aggregation of Aβ proteins as the causative agent of AD (30). However, efforts aimed at understanding this process have produced little clarity and the mechanism of self-assembly remains elusive.

Evidence of similarities of features of aggregates extracted from AD patients with those of Aβ aggregates assembled *in vitro* provide support for the use of *in vitro*

aggregation studies to understand Aβ structural dynamics *in vivo* (31-34)005. Several studies have shown that Aβ42 is the variant implicated in the development of AD, due to its kinetics of aggregation (5, 25, 26, 35-37). These studies demonstrated that Aβ42, compared to Aβ40, nucleates much faster and rapidly forms fibrillar aggregates. A mechanism for this aggregation has been proposed: the protein, from a monomeric state, undergoes transformation and is able to form transient oligomeric species (38, 39). 008aThese oligomers can aggregate further and ultimately form fibrillar aggregates, termed amyloid fibrils (31, 33, 34).

Amyloid fibrils are very stable and have been characterized by AFM (40-42), electron microscopy (43-45), NMR (33, 34, 46), and X-ray crystallography (6, 47). These structural studies revealed that fibrils consist of long, ordered, β-structures that stack in a perpendicular fashion. Fibrils are stabilized by H-bonds and van der Waals interactions, with most fibrils having a twist along the fibril axis that enhances the side-chain and electrostatic interactions (48). Interestingly, Aβ monomers are largely unstructured (49-51).

Solid-state NMR (ssNMR) studies of amyloid fibrils revealed that cross β-structures with either a parallel or an anti-parallel arrangement of monomers are the common structural features of fibrils (52, 53). Another feature of fibrils is the presence of β-hairpin motifs (54, 55), such as the turn-like structure from residues 26 to 30 in Aβ42 fibrils (31). Furthermore, the morphology of fibrils depends on the environmental conditions under which they were assembled; geometrical conformations such as S-shape (33) and U-turn (31) have been observed in aggregation studies performed *in vitro*.

Chapter 1: Introduction

1.2 Toxicity of Amyloid Aggregates

Several hypotheses have been proposed to explain the toxicity and role of Aβ aggregates in the progression of AD, with the amyloid cascade hypothesis receiving recognitions as the principal mechanism of toxicity (56). However, recent findings have caused the hypothesis to be revised to account for the toxicity of Aβ oligomers; in fact, recent findings implicate oligomers as the most neurotoxic species (38, 57-63).

The toxicity of Aβ oligomeric species have been attributed to intracellular, membrane, and receptor-mediated mechanisms (64-66). Oligomers can cause synaptic dysfunction through specific interactions with essential receptors (67-69), or by introducing defects in the plasma membrane through direct interactions, leading to formation of pores and or channels (70, 71). In addition, accumulation of intracellular Aβ oligomers may happen simultaneously with one or more of the extracellular pathways (64, 72-75). However, the formation and mechanism of toxicity of the intracellular aggregates are not well understood.

1.3 Oligomeric Species

One of the elements in the amyloid hypothesis is the progressive increment in aggregation order, going from monomers to oligomers and finally to fibrils (39). However, unlike fibrils the oligomeric species are very transient and their structural characteristics at molecular level are unknown. Various morphologies have been ascribed to oligomers, from spherical aggregates to filamentous (76, 77). It is proposed that oligomers form the critical entities, called nuclei, needed to transition to proto-fibril states before finally fibrillating (57).

Recent findings show that synthetic Aβ is able to faithfully reproduce the characteristics of the oligomers obtained from patients, e.g. resistance to SDS and enzymatic degradation (53, 78-84). Spectroscopic characterization of Aβ oligomers revealed that they are composed of random coil secondary structure, which is able to transition to β-structure as the aggregation progresses (57, 85-87). Furthermore, the structure of a Aβ40 monomer, stabilized by an antibody, containing β-structures suggests that the β-hairpin structure could be an intermediate during Aβ aggregation (88). It has also been proposed that this conformation is an early folding event during Aβ aggregation (89, 90). Interestingly, comparison between the oligomerization of Aβ40 and Aβ42 led to the discovery of a different aggregation pathway depending on alloform (91). For Aβ40 oligomers up to tetramers were observed, whereas Aβ42 yielded oligomers up to dodecamers. These results are in line with previous findings where oligomers had been stabilized by cross-linking (35).

Recent studies have demonstrated that single-molecule approaches are an effective method to study oligomers (92-95). Single-molecule techniques, such as AFM (96-100), tethered approach for probing inter-molecular interactions (TAPIN) (101, 102), and FRET (86), have shown that the early stage oligomers exhibit prolonged lifetimes and stabilities. Novel features of the interaction and self-assembly of Aβ40 and Aβ42 peptides were determined using single-molecule AFM-based force spectroscopy (97). It was found that the Aβ peptides are stabilized by mutations in the C-terminal region, the VPV (G33V-V36P-G38V) mutation stabilizes and, for Aβ40, dramatically change the behavior of the peptide. Another major discovery of the force spectroscopy studies was the high stability

of the amyloid dimers. Findings which suggest that dimerization requires conformational transitions within monomers that enable them to form stable complexes (97, 99, 100).

Single-molecule fluorescence techniques have been used to characterize *in vitro* aggregation of Aβ40, revealing a heterogeneous distribution of small oligomers with dimer-tetramers being the most abundant (103). Furthermore, Sarkar *et al.* showed that the oligomer chemical shifts are very different from fibrils, in particular the N-terminal and the central segment (residues 22-29) (86). These finding are in line with data from Ahmed *et al.*, which show that oligomers have disordered molecular conformations (57). Furthermore, these oligomers were reported to have very solvent accessible N-termini and possess turn structures.

1.3.1 Computational studies

One of the most challenging tasks in the study of proteins, including amyloid proteins, is the determination of structure. Highly dynamic properties of the majority of amyloid proteins, and transient features of their oligomeric species, complicate the use of standard tools of structural biology, i.e. NMR and X-ray crystallography. In such situations, computational tools become indispensable in the pursuit of knowledge about the structural and dynamic properties of complex biological molecules. Computer simulations act as a bridge between experiment and theory by predicting molecular interactions, dynamics, and properties. These predictions can be used to gain insight into experimentally observed behaviors or to provide details obscured in experiments, such as dynamics of protein-protein interactions.

Unlike fibrils, there are no structural data available for oligomers; standard tools of structural biology fail to characterize the early stages of self-assembly due to their

transient nature and heterogeneity; leaving many questions about their formation unanswered (104, 105). Computational simulations have been utilized to supplement the novel single-molecule techniques used to probe early stages of aggregation and, in some cases, elucidate the dynamics and mechanism of aggregation (100, 106-110). Due to the computational cost, the majority of studies of Aβ oligomers have focused on characterizing the structures and dynamics of several key segments of amyloid proteins associated with aggregation.

One of the earliest studies of protein aggregation using an atomistic approach was performed on the Aβ(16-22) fragment (111). The study showed that Aβ(16-22) undergoes several structural transitions whereupon it is able to form conformations with antiparallel β-sheets. Later studies adopted similar approaches to characterize the aggregations of other amyloidogenic peptides (100, 112, 113). Common for all these studies was the observation that the peptides first collapse into disordered aggregates, and later these aggregates undergo structural transitions that reorder the inter-peptide interactions and allow for the emergence of conformation with ordered structures, e.g. α-helices and β-sheets.

Simulation of the Aβ(16-22) and Aβ(25-35) fragments revealed that the two peptides follow different aggregation pathways (114). The Aβ(16-22) initially assumes a disordered oligomeric conformation, in which all hydrophobic residues are shielded from the solvent, and then undergoes a transition to a β-structured oligomer. The Aβ(25-35) peptide on the other hand forms a stable tetrameric oligomer and β-structured aggregates. Moreover, these aggregates coexist with less ordered oligomers. A longer fragment, Aβ(17-42) primarily showed a fibril like conformation with a strand-turn-strand motif (115). Similarly, the Aβ(21-30) fragment forms a hairpin structure (116).

Computational studies of the dynamics of Aβ42 lead to the discovery that, in an aqueous environment, the peptide mainly assumes α-helical structure (117). However, the helices are not stable and transition between structured and unstructured conformations multiple times. Further studies showed that Aβ42 is more structured compared to Aβ40 and has a less flexible C-terminal segment (107). These findings are in line with the comparison of Aβ40 and Aβ42 by Yang and Teplow, which showed that Aβ42 forms more stable conformations that tend towards β-structure and stable C-terminus (118).

More recent simulations of the full-length Aβ have revealed that the size and distribution of the early aggregates for Aβ40 and Aβ42 vary, the most common oligomer being dimers for the former and pentamers for the latter (119, 120). These results qualitatively reproduce the main features of oligomer size distributions measured experimentally. Furthermore, Aβ42 displayed turn and β-hairpin structures that are absent in Aβ40. Other differences between the alloforms was an N-terminus β-strand in Aβ40 but not in Aβ42.

1.4 Significance

Protein misfolding followed by the formation of aggregates, is an early step in the cascade of conformational changes in a protein that underlie the development of a number of neurodegenerative diseases, including Alzheimer's and Parkinson's diseases. Little progress has been made in the treatment of these diseases, due to the lack of knowledge about the self-assembly process. Moreover, the main toxic species remains disputed, primarily due to the lack of a precise mechanism of neurotoxicity. However, recently it has

become apparent that oligomers, rather than fibrillar aggregates, are the toxic amyloid species.

While there have been an increasing number of reports published within the last five years about oligomeric species, the structure of amyloid oligomers has yet to be elucidated. Consequently, the structures of different oligomers and how specific amyloid oligomers contribute to neurotoxicity remain unclear. Leaving the fundamental questions related to the mechanism of oligomer self-assembly and dynamics unanswered. Which, in turn, has impeded the progress in the development of treatment for these diseases.

The results presented in thesis elucidate the molecular mechanism of the initial aggregation processes of amyloid peptides and characterize the structural dynamics of the early aggregates. Moreover, we identified a novel pathway, involving interactions with surfaces, for the spontaneous self-assembly of amyloid proteins in the physiological concentration range, that eliminates the discrepancy between protein concentrations *in vivo* and *in vitro*.

The availability of structures of the early oligomers, and their conformational dynamics, as well as the surface-mediated aggregation pathway advance our knowledge of the aggregation process and helps identify new targets for preventive and therapeutic interventions. Furthermore, the available structure and simulation methodologies enable the development of therapeutics targeted to specific structures and or aggregation states.

Chapter 2.   METHODS

In this chapter a general description of the computational approaches used in the thesis is provided. Specifics of each approach, where relevant, have been given in the methods section of each subsequent chapter.

2.1 Molecular Simulations

Two main branches of simulation techniques exist, molecular dynamics (MD) and Monte Carlo (MC) (121). While MD is more resource demanding, it provides the dynamic behavior of a system over time. Although MD simulations do not model the underlying physics exactly, they provide a close approximation that captures a wide range of critical biological processes and reveal the atomistic behavior of biomolecules at microsecond timescales (122-127).

In MD simulations, a series of step-by-step iterations of computational algorithms are used to obtain atomic trajectories by numerically solving equations of motion using empirically derived parameters called force field. Force fields describe the atomic properties and behavior of molecules using the potential energy of the system as a function of its spatial arrangement, and take into account bonded (bonds, angles, and dihedral terms) and non-bonded (Coulombic electrostatics and van der Waals interactions) contributions (121). The calculations are based on classical law of motion, which has been adopted to algorithmically be calculated using the force,

$$\vec{F_i} = m_i \cdot \vec{a_i} \qquad i = 1, 2, \dots N$$

which gives the force of the i'th particle. Force can also be derived from the gradient of the potential,

$$\vec{F_i} = -\nabla V(\vec{r_i})$$

$V(\vec{r_i})$ is the potential energy of the system. Combining the two yields,

$$m_i \frac{\partial^2 \vec{r_i}}{\partial t^2} = -\frac{\partial V(\vec{r_i})}{\partial \vec{r_i}}$$

which is the equation of motion used, in most MD programs, to obtain molecular trajectories. The power of this seemingly simple approach becomes apparent when studying dynamic processes, such as elongation of an amyloid fibril (128). Nguyen *et al.* utilized atomistic MD simulations to characterize the interactions of a monomeric Aβ(16-22) with a preformed fibril arranged in an anti-parallel β-sheet. They were able to elucidate the process in which the monomer, initially unstructured, interacts with the fibril and rapidly undergoes structural transition to an ordered conformation with β-structures. Following the transition, the fibril-bound monomer then undergoes a slow conversion to an anti-parallel β-structure. Interestingly, the monomers of the fibril also undergo conformational changes during the incorporation of the free monomer. The characterization of this elongation mechanism, termed the dock-lock mechanism, was made possible solely due to MD simulations.

2.1.1 Force Field Parameters for Amyloids

Force fields were originally developed to describe the folding and dynamic behavior of structured proteins, i.e. proteins that have very stable conformations (122). This is in part due to the large body of data available in form of NMR and X-ray crystal structures. Each iteration of the force fields has been tailored to better reproduce these data (129). However,

amyloid proteins are intrinsically disordered proteins (IDPs) and have very little or no regular structure, which may pose a challenge for these force fields (130).

AMBER Force Field

One of the most widely used protein force fields is the AMBER family of force fields. These force fields have been shown, in several studies, to reproduce experimentally observed behavior with a phenomenal degree of accuracy (129). Furthermore, several studies have shown that the AMBER force fields are able to reproduce the characteristics of amyloid proteins and peptides better than other force fields; in particular the secondary structure and arrangement (NMR chemical shifts and coupling constants) of the molecules (50, 100, 118, 131-136). Together with the fact that it is one of the best force field for structural protein, the AMBER99SB-ILDN force field outperforms other force fields, in best describing the behavior of amyloid peptides and proteins (137).

Water Model

Another important factor when performing biologically relevant MD simulations is the inclusion of a biologically relevant environment, i.e. aqueous environment (138). This is critical for amyloid proteins because hydration is very important during for the aggregation (139-141). Several studies have shown that the water model used during simulations is critical for the aggregation behavior of amyloids (142-144). The different water models cause differences in protein structure due to their attributes, e.g. polarity or H-bonding capability, which in amyloid proteins translate to different conformations and compactness; in the case of more polar water models the proteins will be more compact and have less solvent accessible surface.

The choice of water model is not trivial, as most force fields are parametrized using a specific water model; using a different model may cause over- or underestimation of molecular interactions. The AMBER force fields are parametrized using TIP3P water model (145). Recent benchmark studies have shown that this combination of protein force field and water model is suited when describing the interaction and dynamics of amyloids (144).

MARTINI Force Field

Biological ensembles often contain hundreds of thousands of atoms and operate on the time scale of microseconds. However, current computational capabilities impose limitations on how large or for how long a system can be investigated; either simulate a very small system for the timescale of the molecular event or simulate a large system for a very short time. To overcome this problem, many approaches have been developed to accelerate the sampling of the protein conformational landscape. One such approach is the use of coarse grained (CG) descriptions of the molecular system.

Coarse graining involves simplification of the molecular system and interactions and comes with the trade-off of accuracy for computational efficiency. The MARTINI force field is one of the most well characterized CG force fields for proteins and lipids (146, 147). Briefly, MARTINI uses a 4:1 mapping scheme, which replaces 4 heavy atoms with 1 CG pseudoatom. Each pseudoatom carries the physico-chemical characteristics of the heavy atoms it replaces; e.g. hydrogen bonding capability, charge, and polarity.

MARTINI has successfully been used to conduct extensive simulation studies of the amyloid aggregation process (148, 149). In particular very large systems, e.g. the

intermediate processes involved in progression from early oligomers to mature fibrils can be investigated (150).

2.2 Accelerated Molecular Dynamics Simulations

One of the major hurdles in MD simulations is the fact that simulation rarely reach beyond few microseconds, which often leads to an insufficient exploration of the conformational landscape, especially if the molecular system is trapped in a local energy minimum. Consequently, many properties of the biological system may remain unexplored. This fact has led to the development of mathematical algorithms that allow enhanced sampling of the conformational space. One such approach is the accelerated MD (aMD) approach (151).

Accelerated MD is an approach that improves the conformation sampling by reducing the energy barriers in a molecular system. This is done by modifying the potential energy of the system through application of a boost energy when the system energy has fallen below a certain threshold, while leaving the energy levels above the threshold un-modified (151). As a result, energy barriers that may exist, and act as traps during simulation, can be overcome and allow the system to sample conformations that were not accessible during conventional MD (cMD).

Recent investigation of bovine pancreatic trypsin inhibitor revealed that the sampling efficiency of 500ns aMD simulation is equivalent to 1ms unbiased cMD simulation (152). Furthermore, comparison with experimental data showed that chemical shifts as well as structurally important water molecules were reproduced faithfully.

2.3 Monte Carlo Pulling and Validation of the Models

Single-molecule force spectroscopy is a valuable tool in characterization of amyloid protein interactions (97). However, the method does not yield any data regarding the molecular structure of the proteins being examined. Traditionally, steered MD (SMD) simulations have been used to elucidate the force-dependent behavior of the molecular system being pulled in the force spectroscopy experiments (100). However, this poses a major problem, because the applied pulling rates (apparent pulling force) are in the range of nanometers/nanosecond, while experiments are conducted at typically hundreds of nm/s – a 10^7 difference. Recent development of a Monte Carlo based approach, using the PROFASI package (153), allowed pulling simulations at rates of hundreds of ns/nm, which led to the structural characterization of amyloid proteins that exhibited high dissociation forces (154).

The initial MC approach was limited to simulations with only one protein chain and worked by measuring the change in energy of a virtual spring attached to the Cα atoms of N- and C-terminal residues of the protein chain (153). This was modified, in the lab, to extend to two protein chains and any Cα pair; which made possible the characterization of force-induced dimer dissociation (108). More importantly, this allowed, for the first time, the identification and validation of simulated structures obtained from MD simulations based on comparison of characteristic force and rupture patterns. In the modified approach two springs are used, each attached to one Cα atom; during simulations the Cα atoms are pulled apart via the virtual springs along a vector. The energy of the springs is provided by,

$$E_{tot} = E(x) + \frac{k}{2}[L_0 + vt - L(x)]^2$$

where $E(x)$ is the energy of conformation x in the absence of an external force, k

is the spring constant, t is the MC step, L_0 is the initial distance between the two

Cα atoms, $L(x)$ is the distance between the two Cα atoms for conformation x, and v is the

pulling velocity with v=0.1fm/MC step being equal to 600nm/s.

Chapter 3.   EFFECT OF INTRAMOLECULAR FOLDING ON THE AMYLOID SELF-ASSEMBLY

3.1 Introduction

The self-assembly of amyloid proteins into aggregates is currently considered the main molecular mechanism leading to the development of Alzheimer's disease and other amyloid-type neurodegenerative diseases (155-157). As described in Chapter 1, the aggregation process is accompanied by a change in the secondary structure of the monomers, eventually leading to the assembly of the fibrillar structures found in amyloid plaques (158-160).

Recently, Maiti *et al.* have identified β-hairpin structures in Aβ40 oligomers using surface enhanced Raman spectroscopy and solid-state NMR (87). Similarly, a turn like conformation has been found in Aβ42 oligomers within residues 25-29 (57). Furthermore, the structure of a β-hairpin conformer of an Aβ40 monomer suggests that the hairpin structure could be an intermediate during Aβ aggregation (88). Together, these findings suggest that the β-hairpin structure is a common motif in amyloid aggregates, however the role of the hairpin conformation in the assembly of oligomers and during the aggregation process remains elusive. Hence, studying the structure of these aggregates and elucidating the mechanism of how the self-assembly process occurs is crucial for the development of appropriate diagnostic tools and therapeutics for amyloid diseases.

In the current study, we address the question of how the hairpin-type secondary structure of amyloid β contributes to the amyloid self-assembly process. A β-hairpin structure was constructed by connecting two Aβ(14-23) monomers with a turn forming YNGK tetrapeptide. Single-molecule studies revealed that the hairpin fold plays a dramatic

role in the self-assembly process of Aβ(14-23) peptides. The Aβ(14-23) hairpin formed more stable complexes compared to those formed by Aβ(14-23) monomers. Computational modelling of the Aβ(14-23) hairpin and monomer complexes revealed a novel sandwich type structure in which the monomer intercalates into the hairpin, which is accompanied by an increased stability. The role of such transiently formed hairpin folds on the aggregation process of amyloid proteins is discussed.

3.2 Materials and Methods

3.2.1 Experimental Approaches

Sample preparation and experimental characterization procedures are described in detail in ref. (161). Briefly, two peptides were used for all experiments: the monomer, CHQKLVFFAED, and the hairpin, CHQKLVFFAED-YNGK-HQKLVFFAED. Aggregation experiments were carried out using 100μM peptide solutions in 10mM sodium phosphate buffer (pH 7.0) and incubating for 3 days at room temperature. Single-molecule force spectroscopy was carried out on an Asylum Research MFP-3D (Oxford Instruments, Santa Barbara, CA) using silicon nitride probes (MSNL, Bruker, CA) with spring constants in the range of 20−30pN/nm, and a retraction velocity of 500nm/s. Single-molecule TAPIN experiments were performed using Cy3-labeled peptides excited by a 532nm laser at 260mA intensity (ThorLabs Inc., New Jersey, USA). Experiments were performed on an objective-through TIRF with 1.40NA objective and 100ms/frame capture rate.

3.2.2 Computational Modeling

Simulation of Hairpin Structure

To generate the initial structure of the hairpin that will be used for the hairpin-monomer and hairpin-hairpin complex simulations, we conducted cMD simulations using the AMBER99SB-ILDN force field (137) and the TIP3P water model (145). The initial hairpin structure was created by placing the amino acids in a linear and fully stretched conformation. To mimic the experimental design, a Cys residue was added to the N-terminus. The structure was then solvated in a cubic box with TIP3P water molecules. The minimum distance between the peptide and the edge of the water box was 1.5 nm, so that any interactions between periodic copies, due to periodic boundary condition, were avoided. The protonation states of Lys and His residues were set to mimic neutral pH conditions. Na^+ and Cl^- ions were added to neutralize the system charge and to keep a constant salt concentration of 150mM. This conformation was subsequently simulated for 1.2μs in an NPT (constant Number, Pressure, and Temperature) ensemble at 1bar and 300K. Other details of the simulation setup were adopted from our previous work (100). This simulation was performed using the special-purpose super computer Anton (162).

Characterization of Hairpin Interactions

The hairpin-monomer system was assembled using the structure obtained for the Aβ(14-23) hairpin in the previous step and the monomer structure identified in ref. (100). The hairpin-monomer system was solvated into a cubic box using TIP3P water molecules. In order to allow free tumbling before inter-molecular contact, the center-of-mass (CoM) distance of the two molecules was set to 2nm. All other parameters were the same as the hairpin simulation.

The hairpin-hairpin system was assembled in a similar fashion; however, instead of a hairpin and a monomer, the system consisted of two copies of the hairpin randomly placed at a CoM distance of 2nm. Both systems were then simulated for 2.4μs in an NPT ensemble at 300K and 1bar. These simulations were carried out on Crane at the Holland Computing Center (HCC) and Comet at the San Diego Supercomputer Center (SDSC) using the Amber14 (163) software package.

To further extend conformational sampling, the resulting structures from the cMD simulations were subjected to the aMD simulation method (152). The two systems were then simulated with a 500ns aMD simulation as an NVT ensemble at 300K. The simulations were carried out using Crane and Comet.

Dihedral Principal Component Analysis

Dihedral principal component (dPC) analysis (164) was used to acquire the representative structures after the MD simulation. The dihedral angles of the terminal residues were ignored. Equation 1 (below) was used to calculate the free energy:

$$\Delta G(V1, V2) = -k_B T \ln \left(\frac{P(V1, V2)}{P_{max}} \right) \qquad (1)$$

where $V1$ and $V2$ are the 1st and 2nd largest principal components; $P(V1, V2)$ represents the distribution obtained from the MD trajectories, P_{max} is the maximum value of the distribution; and k_B and T are the Boltzmann constant and the absolute temperature, respectively. The Fortran program written by Dr. Yuguang Mu was used to perform this analysis.

Validation of Simulated Structures

The Monte Carlo pulling (MCP) approach with the modified PROFASI package (http://cbbp.thep.lu.se/activities/profasi/) was used to investigate the molecular conformations of the H-M and H-H complexes. Briefly, the two Cα atoms of the N-terminal Cys residues of each molecule were defined as the pulling groups. A virtual spring was attached to each pulling group and used to pull them along a vector during the simulations. A detailed description can be found in ref. (108). We mimicked the experimental pulling rate of 500 nm/s, which translates to v = 0.083 for all MCP simulations. The experiments were carried out using Crane and Tusker at HCC.

3.3 Results

3.3.1 Single-molecule Characterization of Aggregates

Based on our hypothesis, that structure plays a critical role in self-assembly, we designed a hairpin construct using the Aβ(14-23) peptide, known to play a critical role in the aggregation of full-length Aβ amyloid proteins. In addition to this peptide, we also used Aβ(14-23) monomer.

Aggregation studies were carried out with the Aβ(14-23) monomer (100μM), hairpin (100μM), and their equimolar mixture (100μM). AFM images for the monomer, hairpin, and their 1:1 mixture are shown in **Figure 3.1**. Consistent with our previous observations (100), monomers form fibrils. The hairpin forms globular aggregates, while the equimolar mixture of monomer and hairpin assemble into aggregates with a globular shape; however, their morphology is different from those formed by the hairpin alone. Comparing the stability of hairpin-monomer and hairpin-hairpin complexes, investigated using TAPIN experiments and AFM based single-molecule force spectroscopy, showed

Chapter 3: Effect of Intramolecular Folding on the amyloid self-assembly

that the hairpin-monomer is approximately two times more stable compared to the hairpin-hairpin complex, **Figure 3.2**.

3.3.2 Structure and Dynamics of Hairpin

To characterize the underlying mechanism of aggregation and elucidate the effect of the hairpin on the stability of the aggregates we used all-atom MD simulations with the explicit TIP3P water model. The dynamics of the hairpin was investigated using the approach described in our recent publication (100). The initial structure of the hairpin was a fully stretched conformation, which was simulated for 1.2μs to obtain dynamics of the hairpin. Time-dependent secondary structure analysis using DSSP (165) revealed that the YNGK tetrapeptide very rapidly forms a stable hairpin, shown in **Figure 3.3A**. In line with DSSP results, the gyration radius of the hairpin decreases rapidly, indicating a collapse of the initial stretched hairpin, **Figure 3.3B**. Pairwise backbone Cα interaction map of the 1.2μs simulation showed a cross-diagonal pattern, further indicating the formation of a collapsed turn motif centered around the tetrapeptide, **Figure 3.4A**. Dihedral principle component analysis revealed the presence of an isolated and deep energy minimum; clustering of structures in this minimum showed the presence of a collapsed conformation with a short two-strand β-structure, **Figure 3.4B**.

3.3.3 Structure and Dynamics of Hairpin-monomer Interactions

The lowest energy structure of the hairpin, identified from dPC analysis, was then used to characterize the interaction of a monomer with the hairpin. Conventional MD simulation was run for 2.4μs, followed by 500ns of accelerated MD simulation in order to extend the conformational sampling efficiency by several orders of magnitude (152).
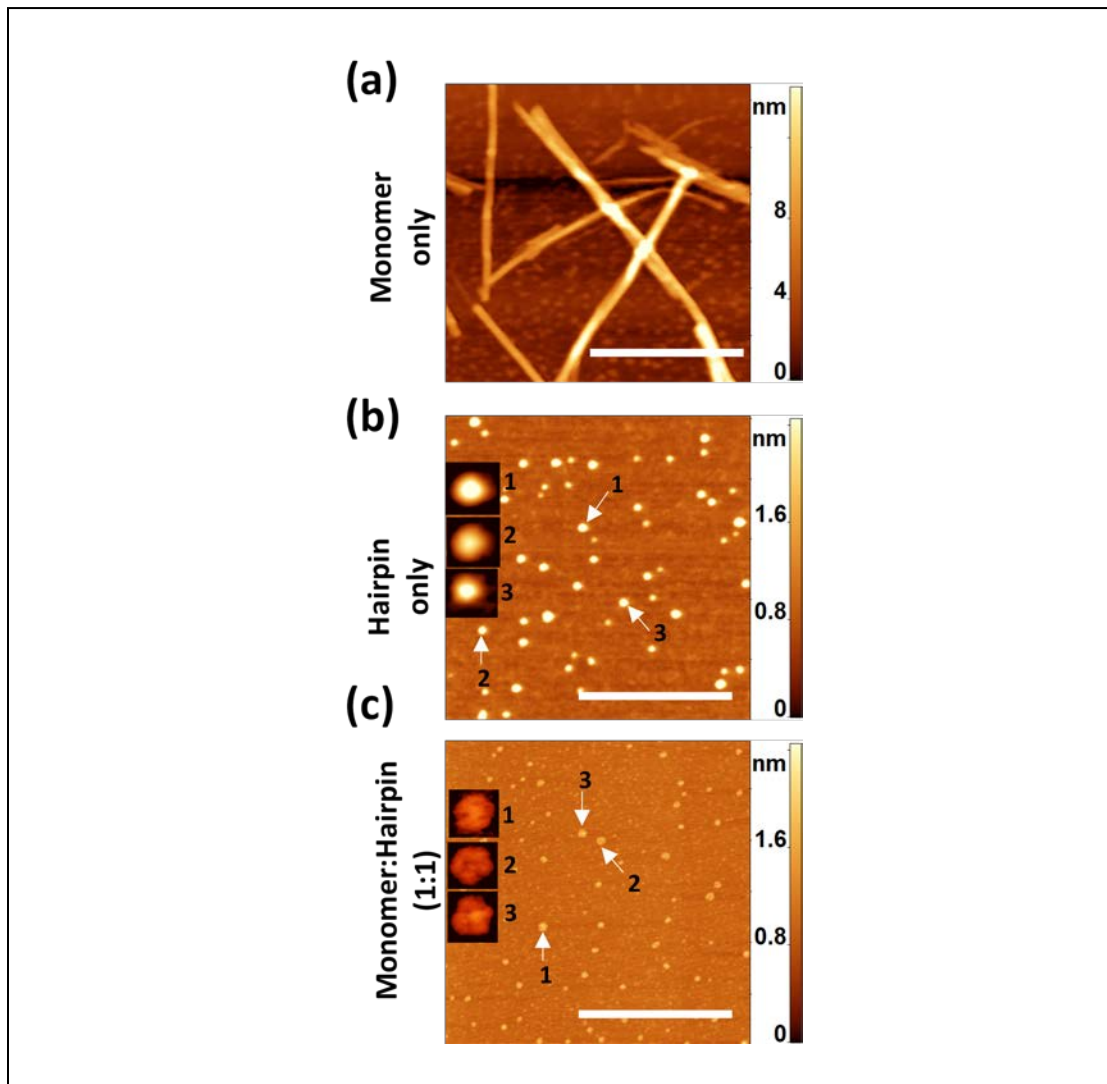
Figure 3.1. Aggregation study of Aβ(14-23) monomer and hairpin. **(a)** Shows fibrillar aggregates formed by monomers, **(b)** globular aggregates formed by hairpin, and **(c)** disk shaped aggregates formed by equimolar mixture of monomers and hairpins. All experiments were performed under same conditions and at 100μM concentration. The scale bars are 500nm.
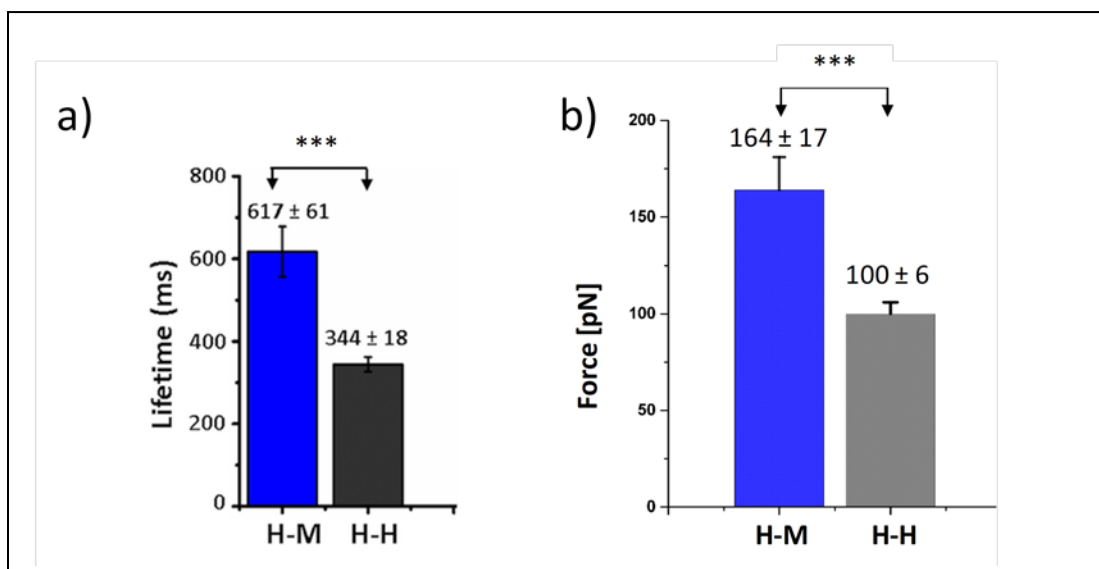
Figure 3.2. Single-molecule probing of hairpin-monomer and hairpin-hairpin interactions. **(a)** Lifetime measurements performed by TAPIN and **(b)** rupture force measurements obtained from AFM based force spectroscopy experiments analyzed using worm-like-chain model. Asterisks indicate statistical significance between the two groups using Kolmogorov-Smirnov test (***$p < 0.005$). Experiments performed at room temperature, 10mM sodium phosphate buffer (pH 7.0), and for force measurements a retraction rate of 500nm/s.
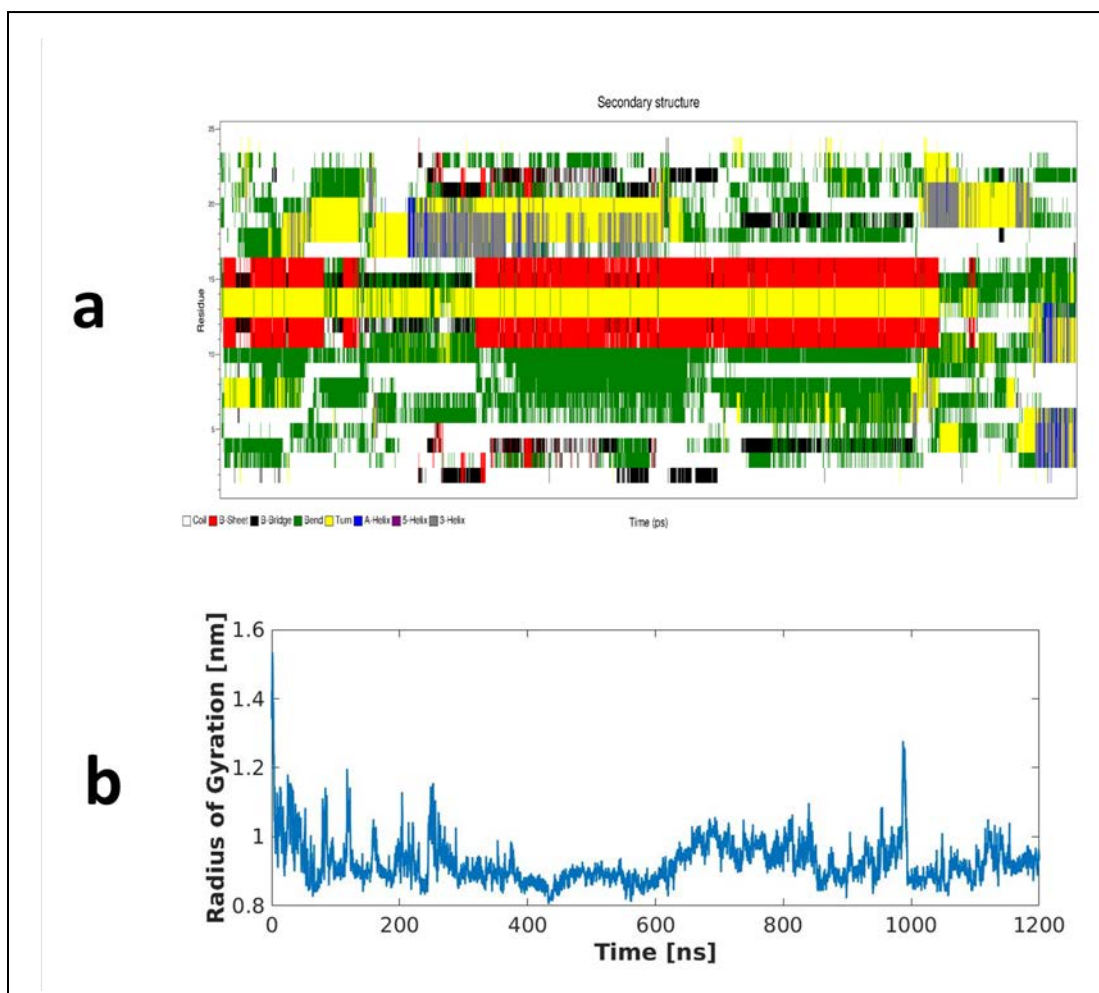
Figure 3.3. Dynamics of hairpin construct during 1.2μs cMD simulation. **(a)** The time-resolved secondary structure of the hairpin as determined by DSSP. The YNGK residues induce a stable β-turn at E10-D11-K12 and G14-K15-H16, seen as solid red and yellow segments. **(b)** The evolution of radius of gyration during the MD simulation.
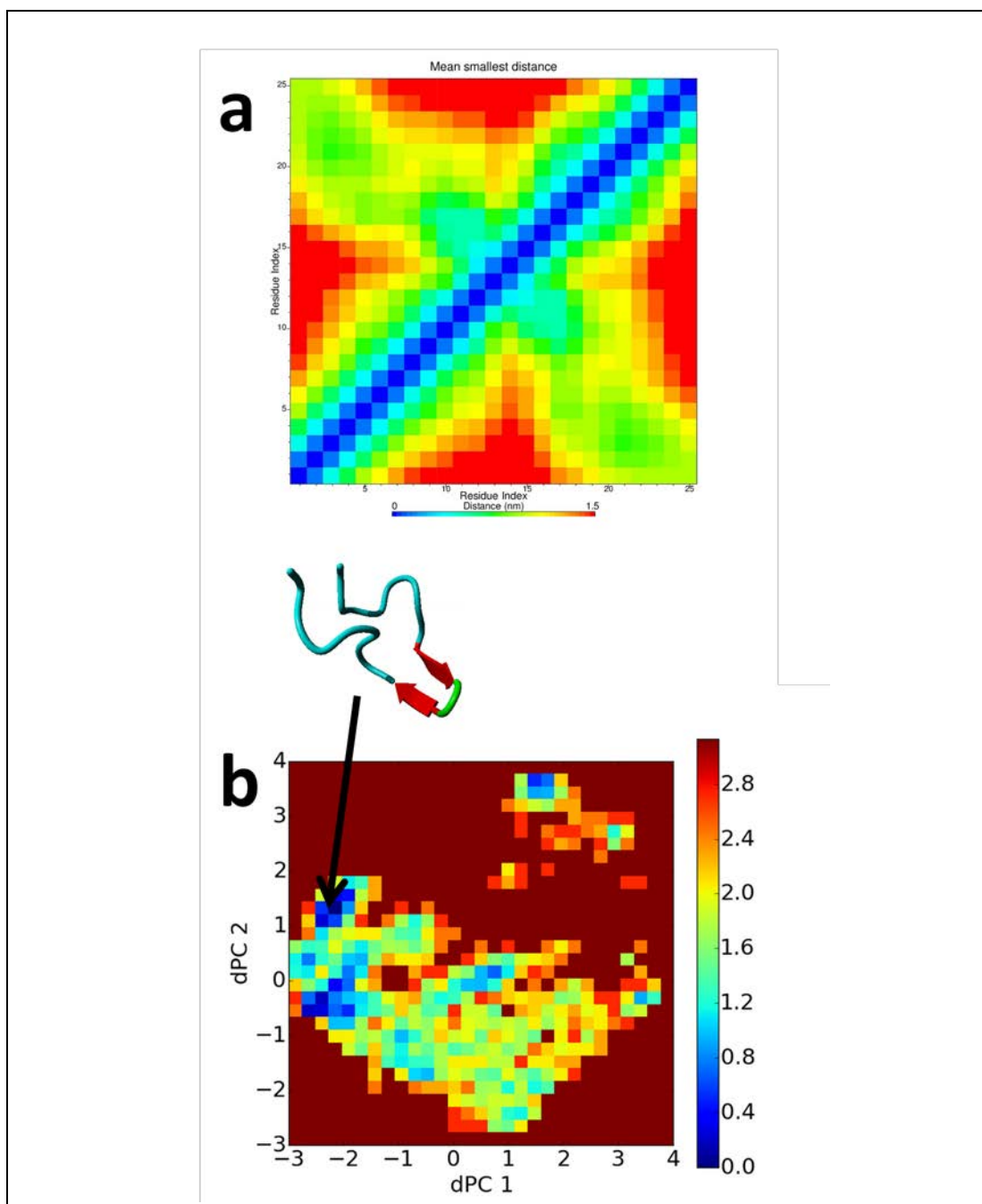
Figure 3.4. Characterization of hairpin conformations from cMD simulation. **(a)** Pair-wise residue interaction map showing the average distance between each residue in the hairpin. The cross-diagonal map is characteristic of a collapsed hairpin conformation. **(b)** Free energy landscape of hairpin simulation obtained using dihedral principal component analysis. The lowest energy structure is shown as cartoon. The colorbar is in units of k_BT.

During the aMD simulation, the hairpin-monomer complex assumes a conformation rich in β-structure; in particular the LVFFA regions of the hairpin contribute with two β-strands, **Figure 3.5**. The monomer is dynamic, undergoing continuous structural transitions, whereas the hairpin remains in a β-sheet conformation for the majority of the simulation. Analysis of the free energy landscape plot (FEP), based on the dPC analysis, revealed several minima, indicating the conformational heterogeneity of hairpin-monomer complexes, **Figure 3.6**. The structures of some of these minima are presented in **Figure 3.6**; the majority of complexes exhibit β-structure for the hairpin while the monomer assumes a plethora of conformations.

Further investigation of the conformations in each energy minima was performed using Monte Carlo pulling simulations. We used four structures, obtained from the dPC analysis of aMD results, corresponding to A-D on **Figure 3.6**. For each conformation, 500 MCP simulations were performed. The forces generated from each structure were assembled into histograms and compared with experimental data. The MCP results are shown in **Figure 3.7**. From the MCP simulations, it becomes clear that the Type D forms the most stable complex, with a mean rupture force of 141 ± 12pN. The distribution of forces and the mean are consistent with experimentally obtained rupture forces, 164 ± 17pN.

Type D structure is a novel conformation with the monomer intercalated inside the hairpin. This intercalated structure is formed from four short β-strands, resulting in an extended antiparallel arrangement, which is stabilized by three intra-molecular and five inter-molecular hydrogen bonds. Moreover, side chain interactions between Phe and His residues and a Lys-Asp salt bridge also contribute to the stability of the complex. These interactions all contribute to the elevated stability of the intercalated hairpin-monomer
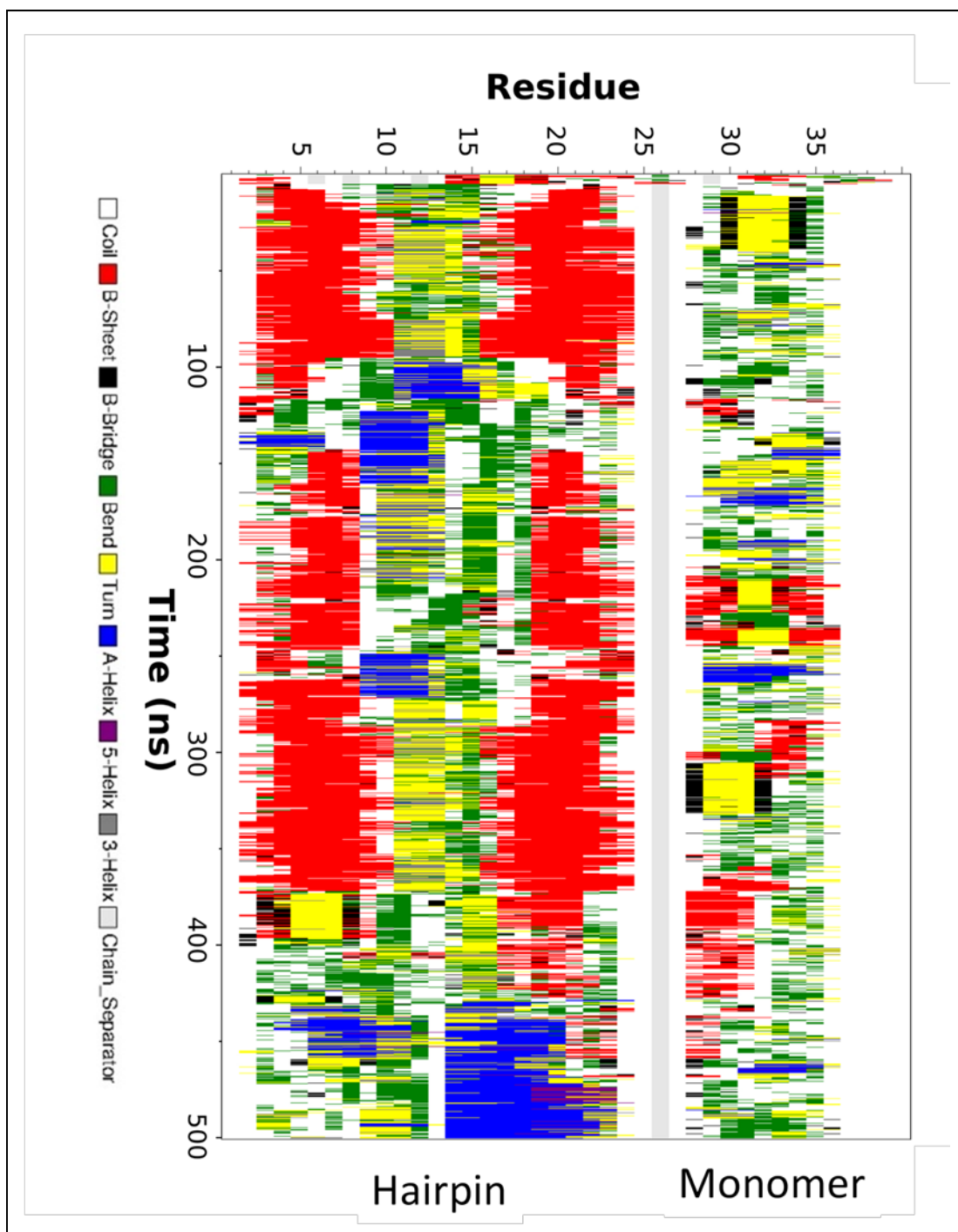
Figure 3.5. DSSP analysis of the change in secondary structure during aMD simulation of the interaction between hairpin and monomer.
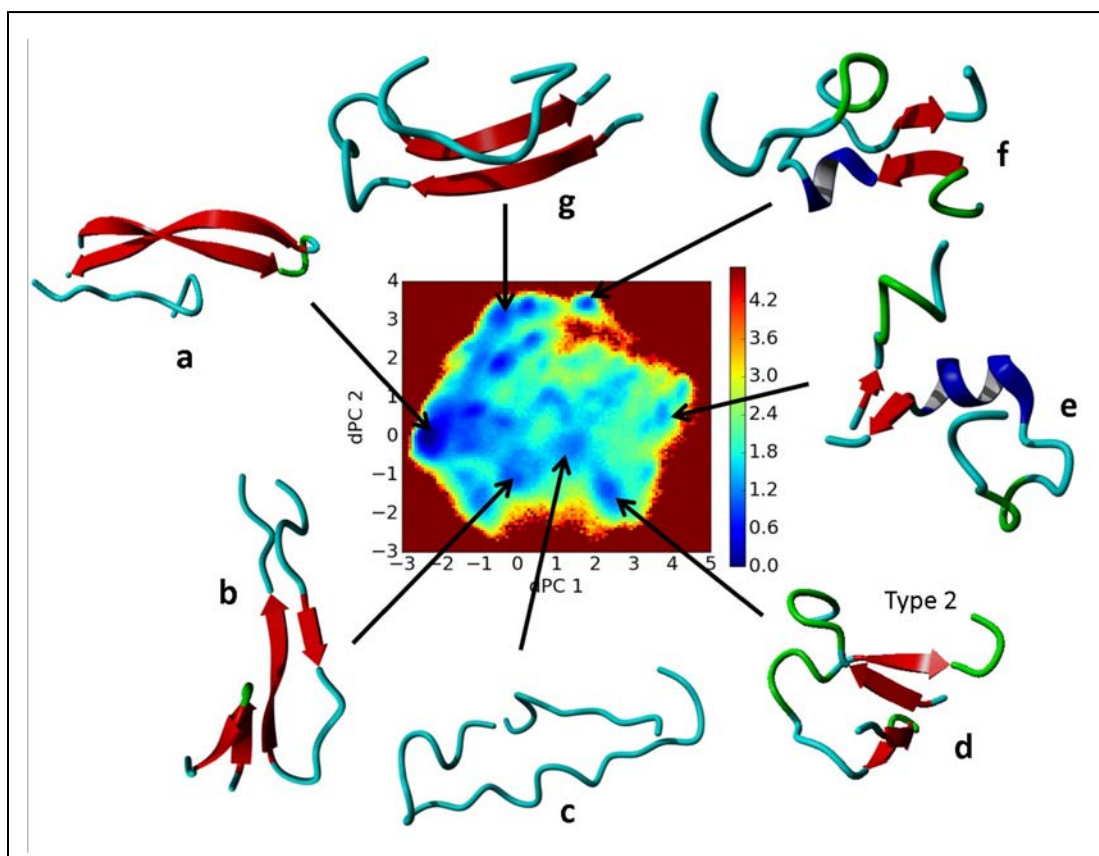
Figure 3.6. Free energy landscape according to dihedral principal component analysis for 500ns aMD simulation of hairpin-monomer system. Selected minima are highlighted with arrows and the most representative structures are shown for the respective minima (a-g). Colorbar is in units of k_BT.
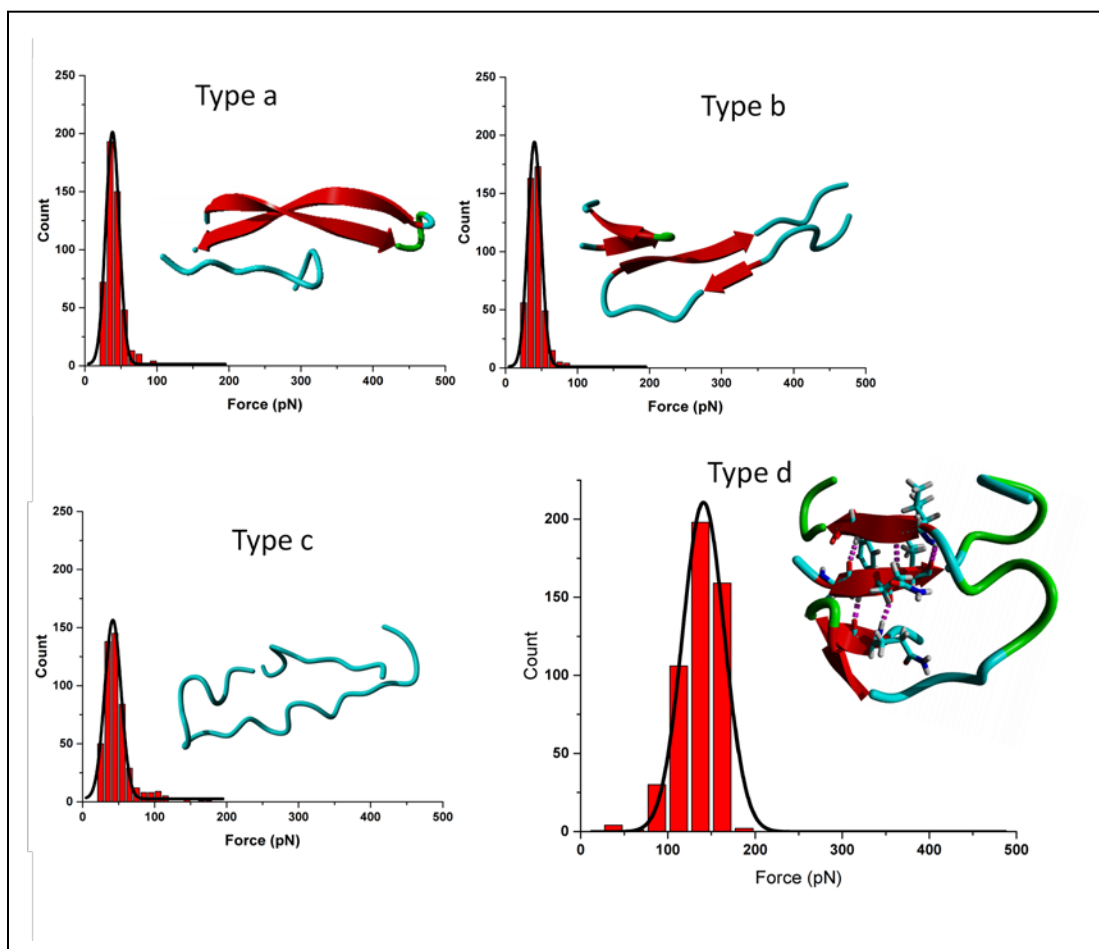
Figure 3.7. Monte Carlo pulling simulations for hairpin-monomer complexes obtained from energy minima in **Figure 3.6**. The histograms show forces obtained during MCP simulations, while black solid curves are Gaussian approximations. Structure of the conformation used in simulation is given in cartoon representation above the histograms.

complex. Hence, we posit that the interlaced structure is the main structural motif of the hairpin-monomer complex.

3.3.4 Dynamics of Hairpin-hairpin Interactions

Similar strategy, used for hairpin-monomer interactions, was employed to characterize the hairpin-hairpin complex. DSSP analysis revealed that, unlike the hairpin-monomer, the complex of two hairpins is structurally more dynamic, with one hairpin undergoing change in structure throughout the simulation, **Figure 3.8**. The energy landscape, based on dPC analysis, is rough with several minima clustered together locally and other minima spread further apart, **Figure 3.9**. All minima are separated by large energy barriers.

The hairpin-hairpin complex is stabilized by inter-molecular H-bonds and by side-chains from both hairpins interacting to form a hydrophobic pocket in the complex consisting of LVFFA residues from both peptides. MCP simulations revealed that the most stable hairpin-hairpin conformation dissociates at a mean force of 75 ± 10pN, **Figure 3.10**.

3.3.5 Dissociation of Hairpin Complexes

Taking a closer look at the dissociation of the hairpin-monomer and hairpin-hairpin complexes reveals important details regarding the structural arrangement of the peptides. During the force-induced dissociation, the hairpin-monomer complex transitions to a horseshoe shape, which allows the monomer to interact with a larger number of residues on the hairpin, **Figure 3.11A**. The re-arrangement of the complex leads to the formation of an extended β-sheet. This new sheet of anti-parallel strands remains stable for a period,
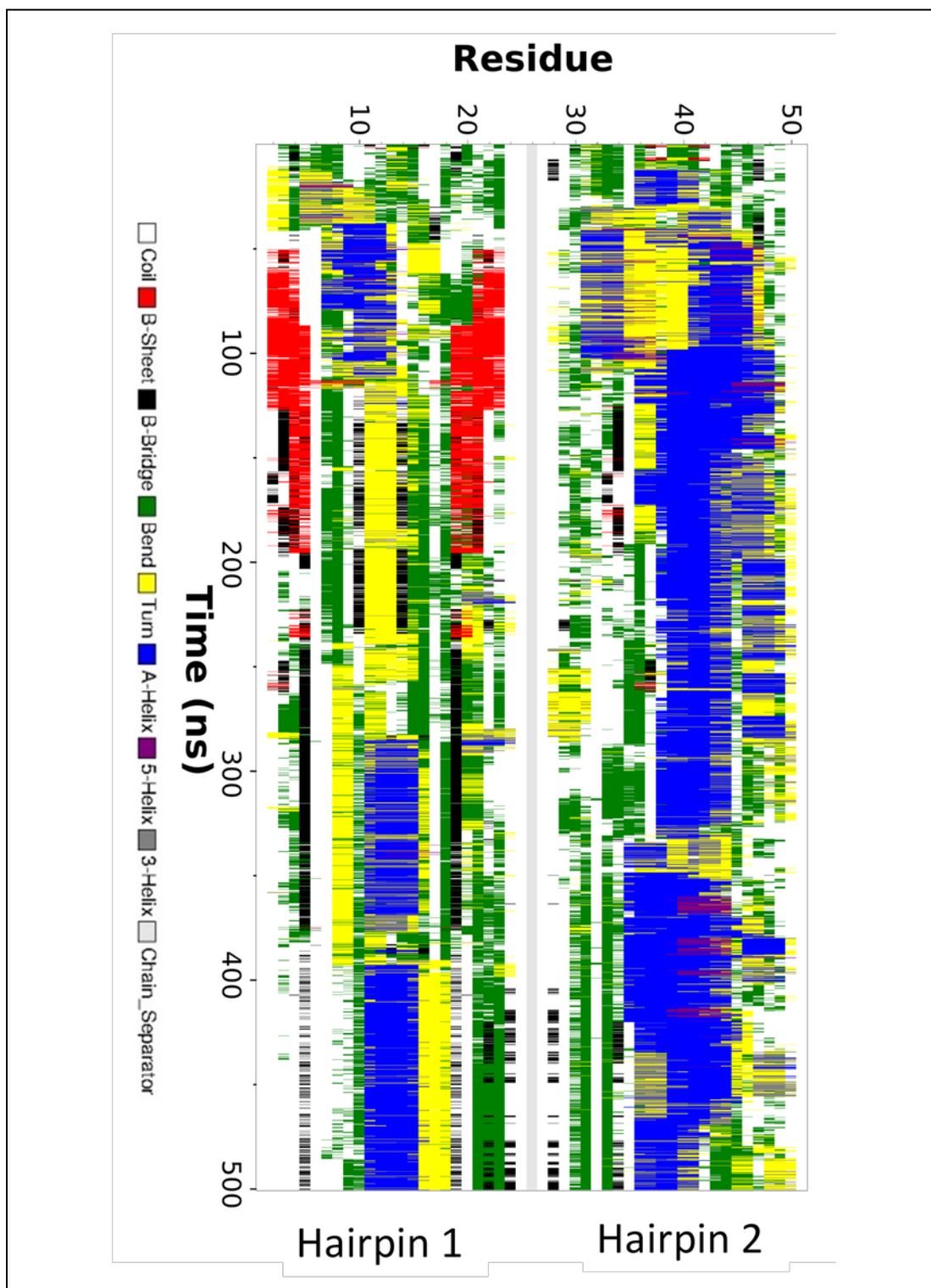
Figure 3.8. DSSP analysis showing the change in secondary structures of individual hairpins during aMD simulation of hairpin-hairpin interaction.

Chapter 3: Effect of Intramolecular Folding on the amyloid self-assembly
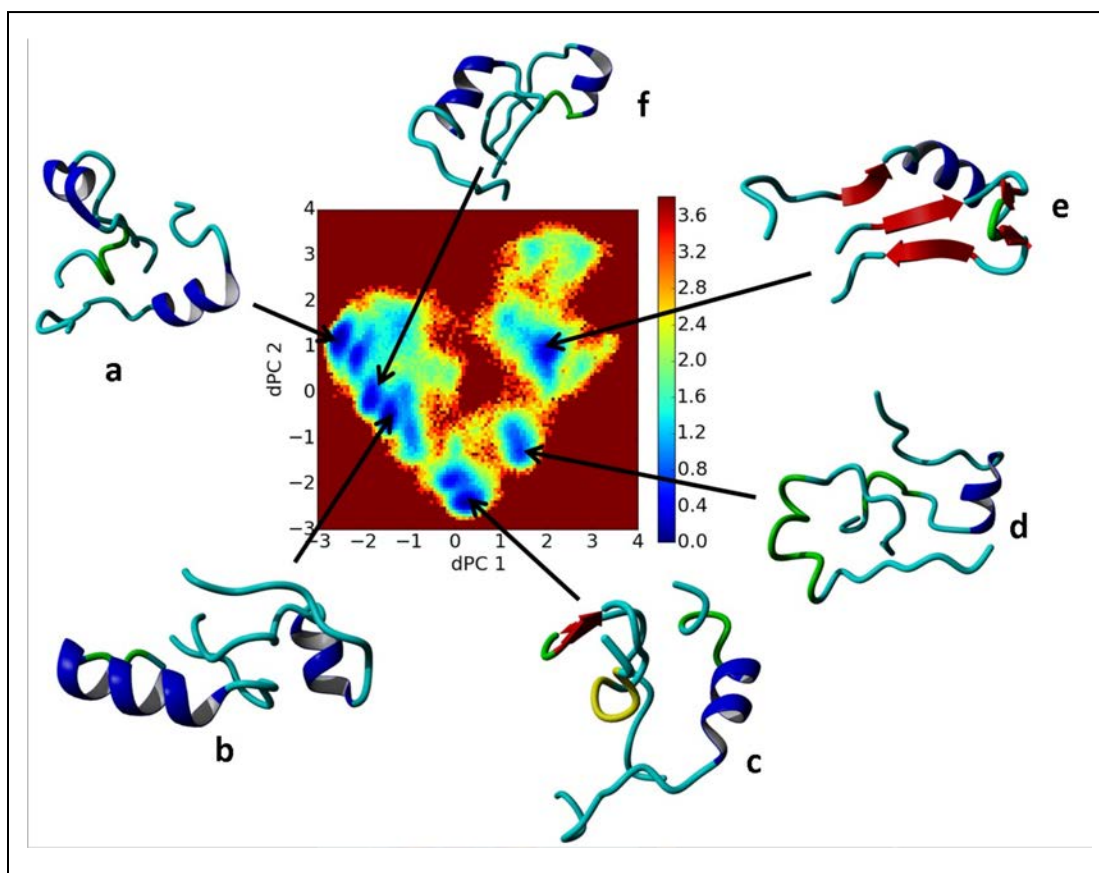
Figure 3.9. Free energy landscape, according to dPC analysis, after 500ns aMD simulation of the hairpin-hairpin complex. The most representative structures are shown for some of the minima (a-f). Colorbar is in units of k_BT.
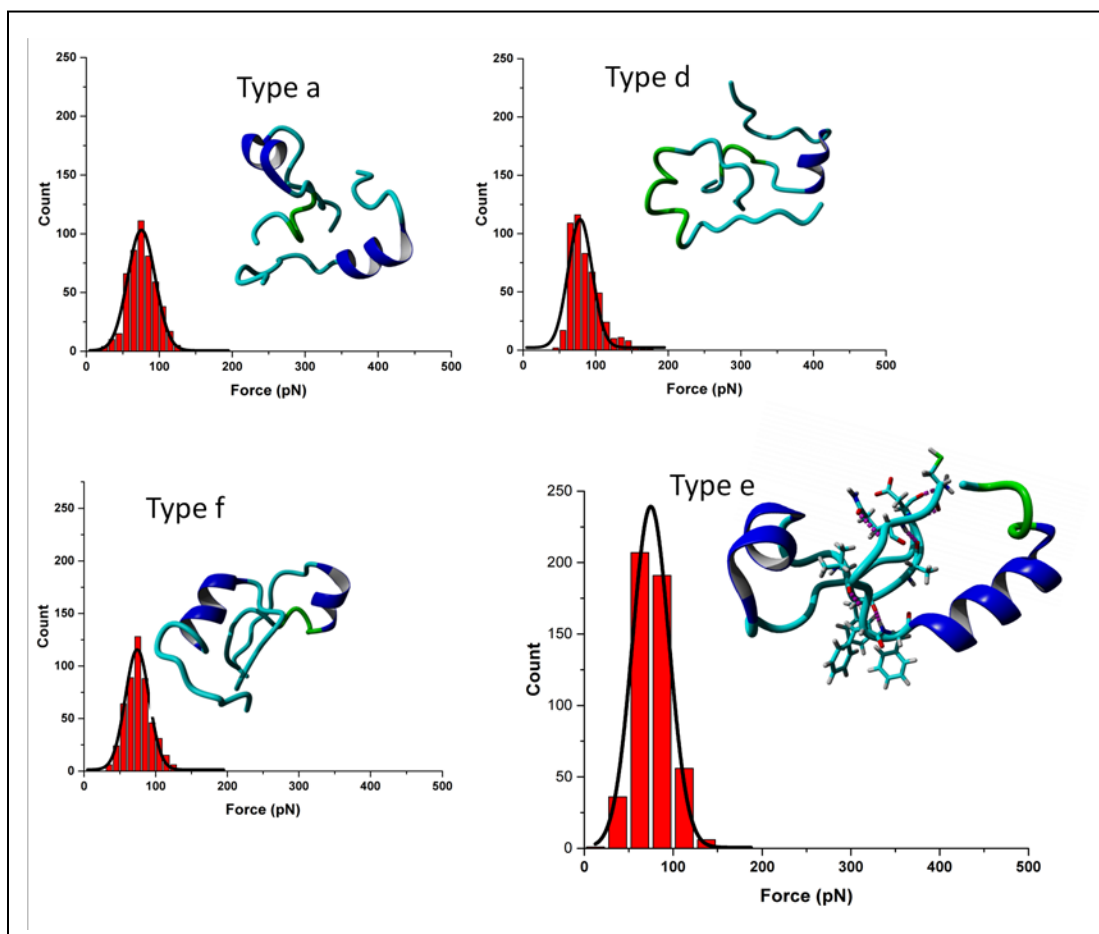
Figure 3.10. Monte Carlo pulling force histograms for hairpin-hairpin complexes; corresponding structures are shown in the insets. Structures are named according to energy minima in **Figure 3.9**. The black curves indicate Gaussian approximations.
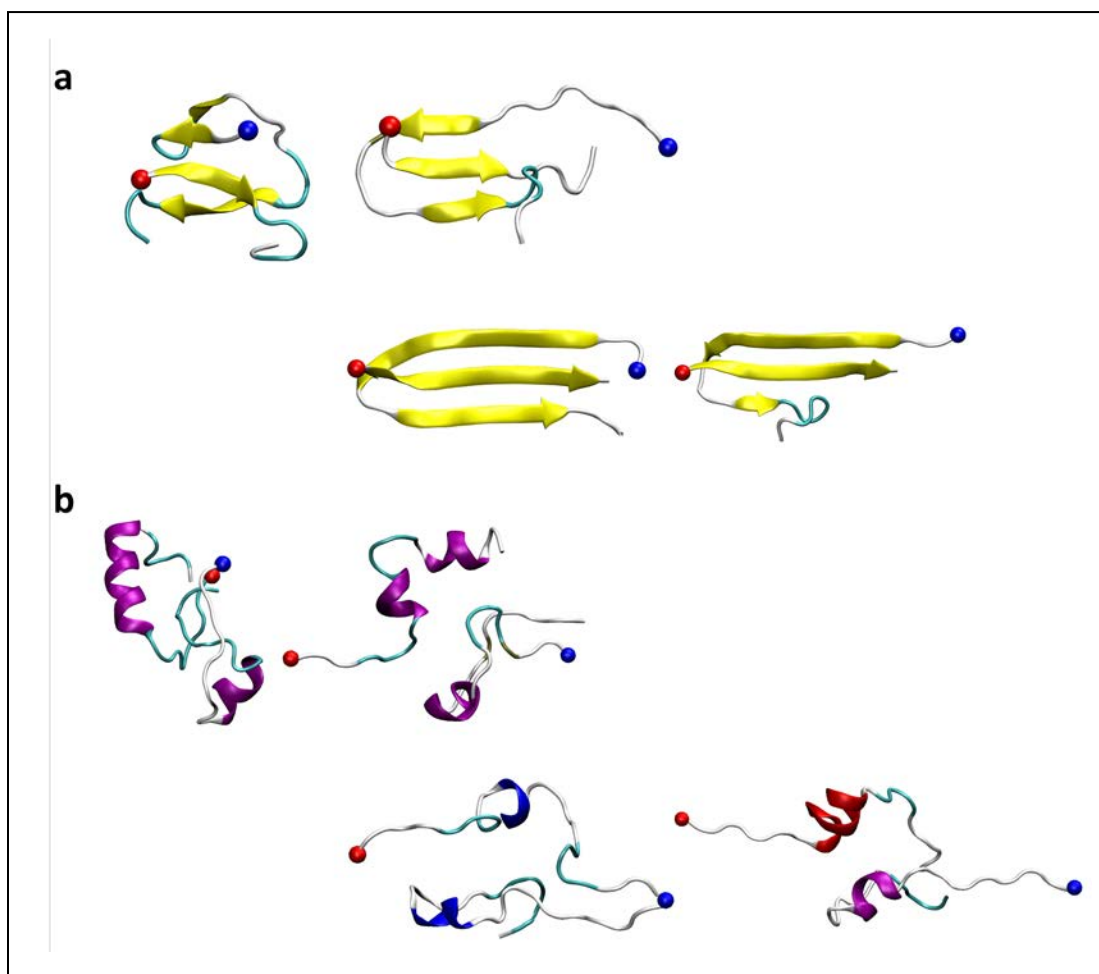
Figure 3.11. Rupture processes observed during MCP experiments. **(a)** The rupture process for hairpin-monomer complex producing 140pN force. The hairpin transitions to a horseshoe shape, allowing a larger number of residues to interact, leading to the formation of an extended β-sheet. Dissociation occurs when the sheet is destabilized. **(b)** Rupture of the hairpin-hairpin complex, requiring 90pN, occurs via conformational change in the complex leading to the loss of secondary structure and side-chain interactions. Blue and red spheres represent the pulling groups.

after which the sheet is destabilized due to re-arrangement of the strands, and the monomer is then able to dissociate.

For the hairpin-hairpin complex the dissociation is very different, initially the complex loses secondary structure as the peptides are pulled apart, **Figure 3.11B**. Gradually, this leads to the re-arrangement of the side-chains, which at the point of rupture have become disorganized and unable to maintain the stability of the complex.

3.4 Discussion

The data presented in this multifaceted study provides compelling evidence to support our hypothesis, that the folding pattern of amyloid protein defines the aggregation pathway. Aggregation experiments demonstrate that the morphology of amyloid assemblies is sensitive to the structure of the monomeric precursors: While Aβ(14-23) monomers assemble into fibrils, like those observed for full size Aβ proteins, the hairpin construct forms globular structures, like those for GNNQQNY peptide (166), with no evidence of the formation of fibrils or protofibrils. Importantly, the equimolar mixture of hairpin and monomer does not produce fibrils; rather they assemble in disk-shaped nanostructures. The finding that fibrillar aggregates do not form suggests that the hairpin fold dramatically changes the aggregation pattern, despite the presence of the fibril forming monomers. Similar results were also obtained from the Aβ42 hairpin, which was stabilized by a disulfide bond formed between mutations at A21C and A30C (167). To further elucidate the role of these hairpin structures on the assembly processes, extensive computational analyses were performed.

Extended MDs simulation revealed that the hairpin by itself exists in a collapsed turn conformation with minimal secondary structure (**Figure 3.4**). This is in line with NMR

data, which showed that the YNGK tetrapeptide induces a U-shaped geometry (168). Interactions of this collapsed hairpin conformation with Aβ(14-23) monomer revealed that the hairpin undergoes conformational change. Following the conformational change, the hairpin-monomer complex adopts a novel conformation with the monomer intercalated inside the hairpin (**Figure 3.7**). The complex has a high β-structure content, in particular the LVFFA regions of the hairpin contribute with two β-strands while the monomer is sandwiched between these two regions in an anti-parallel orientation. Interestingly, a similar three strand conformation, albeit without a hairpin, was recently proposed for the disc-shaped aggregates of the VDSWNVLVAG decapeptide (169).

The hairpin-hairpin complex assembles very differently compared to the hairpin-monomer complex. The hairpins interact in a side-by-side fashion and are stabilized by side-chain interactions. The hairpin-hairpin complex does not contain high β-structure content, instead the conformation best representing experimentally observed data contains segments of α-helical structure. This helps explain why the aggregates are globular instead of fibrils; the α-helical conformation significantly hampers the formation of fibrillar aggregates (170). Recent observations of α-helical Aβ oligomers further support our findings (135, 170, 171).

Monte Carlo pulling simulations revealed the stabilizing effect of the collapsed hairpin on interactions with monomers. Hairpin-monomer assembly is considerably more stable compared to the hairpin-hairpin complex. Comparison with AFM pulling experiments demonstrated that the intercalated hairpin-monomer assembly produces a high rupture force that is in good correlation with the experimental AFM probing of the hairpin-monomer interactions.

Chapter 3: Effect of Intramolecular Folding on the amyloid self-assembly

Altogether, computational analyses reveal that the secondary structure of the hairpin provides a novel type of interaction with the monomer. This novel assembly explains the results of the aggregation experiments, in which an equimolar mixture of monomer and hairpin produced non-fibrillar assemblies. In the mixture of monomers and hairpins all the combinations of hairpin-hairpin, hairpin-monomer, and monomer-monomer are possible, but computational modeling suggest that the hairpin-monomer arrangement produces the most stable conformation. As a result, the most stable hairpin-monomer configuration in the mixture acts to seed the aggregation process. This is in line with the findings of Ahmed *et al.*, which showed that Aβ42 is able to form oligomers containing turn motif that assemble into disc-shaped morphologies (57). Interestingly, the turn is located at residues H13-Q15 and G25-G29 and the overall oligomer is disordered, as measured by FTIR.

The observation that the morphology of aggregates is highly dependent on the secondary structure of Aβ(14-23) peptide suggests that the conformational transitions of the full-size Aβ peptides during the aggregation process plays a crucial role in the entire aggregation process of amyloids. Given the fact that Aβ(14-23) forms fibrils with morphologies similar to those for full size Aβ protein, we assume that this segment in the full size Aβ42 monomer should be structured to allow the molecules to assemble oligomers capable of fibril formation. Indeed, this seems to be the case, as mutation studies show that substitution in the 14-23 region with less hydrophobic amino acids or with proline lead to loss of fibril formation ability (78, 172, 173). Alternatively, intra-molecular folding of the 14-36 segment of Aβ42 protein in the hairpin-type structure can lead to the assembly of non-fibrillar aggregates (34, 46). These can be morphologically similar to those found in

Figure 3.1B and **C**, due to the structural heterogeneity of the monomers containing a mixture of folded and unfolded molecules, respectively. However, these are hypothetical models that need to be verified through future investigations.

Increasing evidence suggests that the self-assembly of Aβ protein underlies the early onset of AD. Given that small Aβ oligomers are the most neurotoxic species, a shift to an aggregation pattern dominated by assembly of non-fibrillar species would shift the aggregation process to the disease prone state. Based on our studies, we hypothesize that stabilization of the internal hairpin structure within (14-36) segment of the full size of Aβ42 protein can drive such a process. Furthermore, this assembly can be modulated by environmental conditions or interaction of Aβ42 protein with other molecules including cellular membranes. Our experimental approaches can be used for testing this hypothesis in future studies.

3.5 Conclusions

We demonstrated that the hairpin fold induces morphological and stability changes in the aggregates of Aβ(14-23) peptide. Using extended MD simulations, we characterized the mechanism of aggregation of the hairpin. Interactions of the hairpin with monomers results in a novel intercalated conformation with high β-structure content. The intercalated structure is stabilized by intra- and inter-peptide H-bonds and side-chain interactions. Monte Carlo simulations of the intercalated conformation further revealed that the intercalated structure produces a high rupture force that is in good agreement with the experimental AFM probing of the hairpin-monomer interactions. These finding suggest that the initial structure of amyloid proteins define the aggregation pathway.

Chapter 4.   SELF-ASSEMBLY OF FULL LENGTH AMYLOID β 40 INTO DIMERS

4.1 Introduction

Despite the small structural difference (two amino acids) between the two most studied Aβ alloforms (Aβ40 and Aβ42), they display distinct behavior, although the structural basis for this phenotype is unknown (16, 27-29, 35). Furthermore, recent compelling evidence show that amyloid oligomers rather than fibrils are the most neurotoxic species (38, 60-63). Hence, a detailed characterization of these oligomeric forms of Aβ is important for understanding neurotoxicity and pathology in AD.

Despite extensive effort, the oligomer formation process and the structure of toxic and non-toxic oligomers remain largely unknown due to the intrinsic transient nature of oligomers, which renders traditional structure determination techniques (e.g. X-ray crystallography and NMR spectroscopy) non-amenable under physiological conditions. Detailed structural information, presented in the previous chapter, about the effect of the hairpin fold on the aggregation behavior of a short Aβ fragment may shed light on the effects of different transient conformations during aggregation. However, the hairpin was an idealized model, using the most aggregation prone Aβ fragment with the sequence of the turn not from the Aβ peptides, making the translation of the observed behavior to the full-length peptides problematic; in particular, because self-assembly is a kinetic process and the additional amino acids can influence the peptide-peptide interactions and ultimately the aggregation pathway. Nonetheless the developed simulation procedures are applicable to investigate the interaction of the full-length peptides.

We recently characterized the conformational changes in monomers of Aβ(42) peptide upon dimer formation using long-time scale MD simulations (174). The simulations revealed that the dimer is very dynamic, which resulted in a multitude of different conformations being identified. By utilizing the recently developed Monte Carlo pulling approach (108), we were able to identify the most likely native conformation of the dimer, which generated statistically similar rupture forces and interaction profiles as was observed in AFM experiments.

Here, we applied the developed simulation approaches to analyze the dimer formation of full-length Aβ40 peptides. Different types of dimer conformations were identified, all with small segments of ordered structures and lacking the characteristic β-sheet structures found in amyloid fibrils. These dimers structures were then validated using MCP simulations and by comparing with stability and interaction data obtained from AFM-based force spectroscopy experiments. The validated dimer conformations were then used to compare Aβ40 and Aβ42 dimers and characterize the differences between the interaction of monomers and the resulting dimers.

4.2 Material and Methods

4.2.1 Monomer Simulation Procedure

To generate the initial structure of the monomers used for the dimer simulation, we conducted cMD simulation using GROMACS ver. 4.5.5 (175) employing AMBER99SB-ILDN force field (137) and the TIP3P water model (145). The initial monomer structures were adopted from NMR data (PDB ID: 1AML) (49), obtained in trifluoroethanol (TFE):water (40:60 vol. ratio). After which 500ns NPT cMD, at 1bar and 300K, were

carried out using resources at the HCC. Cluster analysis was then performed using *g_cluster* command in the GROMACS package, with the GROMOS method of clustering and the root-mean square deviation (RMSD) for the protein backbone with a 3Å cut-off value, as previously described (100). Due to large structural fluctuations of residues 1–9 and 36–42, only data for residues 10–35 were selected for cluster analysis.

We addressed secondary structure dynamics according to the method developed by Thirumalai's group (176). Briefly, if the dihedral angles from two consecutive residues satisfy the definition of an α-helix (-80° $\leq \phi \leq$ -48° and -59°$\leq \psi \leq$ -27°) and β-strand (-150° $\leq \phi \leq$ -90° and 90 $\leq \psi \leq$ 150°), the structures are considered to be α and β conformations, respectively. The changes of secondary structure over time are monitored by, $\alpha(t) = \frac{1}{\Delta} \int_t^{t+\Delta} \alpha_s(s)ds$ and $\beta(t) = \frac{1}{\Delta} \int_t^{t+\Delta} \beta_s(s)ds$, where $\alpha(s) = \frac{1}{41} \sum_{i=1}^{41} \delta_{i,\alpha}$ and $\beta(s) = \frac{1}{41} \sum_{i=1}^{41} \delta_{i,\beta}$ at t =s and Δ=1ns. When the residues adopt α or β conformations, the $\delta_{i,\alpha} = 1$ or $\delta_{i,\beta} = 1$.

4.2.2 Dimer Simulation on the Specialized Supercomputer Anton

For simulations on the special purpose supercomputer Anton, we used the Maestro-Desmond software package Version 4.0 (Schrödinger, New York, NY, 2014) to build the initial starting configuration using two copies of the most representative structure for the monomer. The simulation used the same force field and water model as for the monomer cMD simulation. The dimers were created from copies of monomers with different orientations from cluster 1 in **Figure 4.1**, with the angle between the long axes of each monomer at 90° or 180°. The dimer systems were then run for 4µs cMD simulations on Anton.

Chapter 4: Self-assembly of full length amyloid $\boldsymbol{\beta}$ 40 into dimers

The calculation of the time-dependent secondary structure changes follows the same methods as described in the monomer simulation section. Here, $\alpha(s) = \frac{1}{82}\sum_{i=1}^{82}\delta_{i,\alpha}$ and $\beta(s) = \frac{1}{82}\sum_{i=1}^{82}\delta_{i,\beta}$ at t = s and Δ=1.2ns.

4.2.3 Accelerated Molecular Dynamics Simulations

To extend conformational sampling, the resulting structures from the cMD simulations on Anton were subjected to the aMD simulation method using Comet at SDSC. The simulation procedures were adapted from ref. (152).and the website (URL: http://ambermd.org/tutorials/advanced/tutorial22/). The dimer systems were then submitted to a 500ns NVT aMD simulation.

The principal component analysis of backbone dihedrals (164), in which the artifacts from combining internal and overall motion are minimized, was used to acquire the representative structures after the aMD simulation. In total, 1,500,000 unique structures were used for the dPC analysis. The dihedral angles of the terminal residues were ignored. The following equation for the free energy calculations was used:

$$\Delta G(V1, V2) = -k_B T \ln\left(\frac{P(V1, V2)}{P_{max}}\right) \quad (1)$$

where $V1$ and $V2$ are the 1st and 2nd largest principal components; $P(V1, V2)$ represents the distribution obtained from the MD trajectories, P_{max} is the maximum value of the distribution; and k_B and T are the Boltzmann constant and the absolute temperature, respectively. The Fortran program written by Dr. Yuguang Mu was used to perform this analysis.

4.2.4 Monte Carlo Pulling Simulations

The Monte Carlo pulling simulations, via the modified PROFASI package, was performed

using our previously described procedure (108), with FF08 force field and implicit water.

Dimer structures obtained from dPC analysis of pooled aMD data were used for MCP.

Briefly, the two Cα of the N-terminal Cys residues of each monomer were defined as the

pulling groups. A virtual spring was attached onto each pulling group and used to pull them

along a vector during the pulling simulation. The energy of the springs was calculated by

the A2A spring function and the total energy in the course of pulling was described by the

following equation,

$$E_{tot} = E(x) + \frac{k}{2}[L_0 + vt - L(x)]^2 \quad (2)$$

where E(x) indicates the energy without an external force, k and t are the spring constant

of the virtual spring. L_0 is the initial distance between two Cα atoms of the N-terminal Cys

residues of each monomer. L(x) represents the real-time distance between the Cα atoms of

Cys residues during pulling, and x denotes a protein conformation. Here, v = 0.083,

equivalent to 500 nm/s, and was used for all MCP simulations.

Similar to the dimers obtained during the aMD simulations, we investigated

dimers assembled from fibril structures. Two fibril conformations were chosen to perform

MCP simulations, PDB IDs: 2LMN and 2MVX. Chains A and B, excluding hydrogen

atoms, from the first frame of the PDB files were extracted using VMD (177) and used for

MCP analysis. For 2LMN, the missing residues, 1-8, were added using YASARA

molecular modeling and simulation program (178).

4.2.5 Analysis Software

The cluster network for monomer simulations was prepared by Visone (179) using *g_cluster* data obtained from the simulations.

The dihedral angle calculations and movies were made with VMD, and the protein snapshots were generated by YASARA.

The contact map and free energy landscape plots were generated via Python2.7 (Python Software Foundation. Python Language Reference, version 2.7. Available at http://www.python.org) (180, 181).

Matlab (MathWorks Inc., Natick, MA, USA) was used to analyze the force curves, as well as generate plot and perform statistical analysis.

4.3 Results

4.3.1 Aβ40 Monomer Structure.

As a preliminary step for the simulation of Aβ40 dimerization process, we performed cMD simulations of Aβ40 monomers to identify the most representative monomer structure. We adopted the approach from our recent simulations of the dimer structures for Aβ42 peptide (174). Briefly, the NMR resolved Aβ40 monomer structure (PDB ID: 1AML) was used as initial conformation for a 500ns all-atom MD simulation using the explicit TIP3P water model. The most representative structure was then identified using cluster analysis by calculating the RSMD of backbone atoms between all pairs of structures with a cut-off at 3Å (182). Only data for residues 10–35 were selected for cluster analysis, due to large structural fluctuations in residues 1–9 and 36–40. The results of the cluster analysis are shown in **Figure 4.1**. Twelve clusters were identified, with the 1st cluster comprising 47.5%
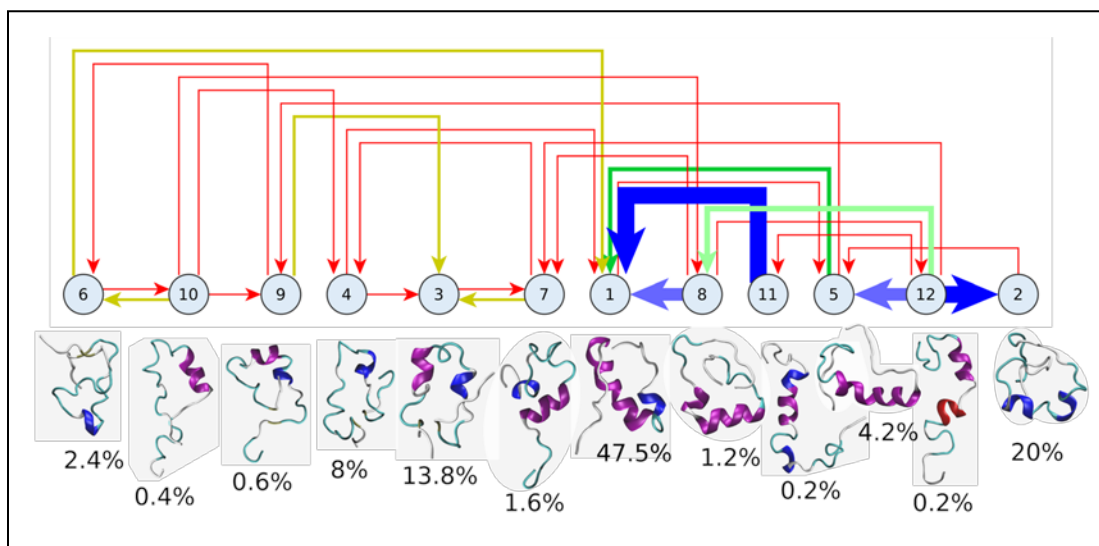
Figure 4.1. Cluster analysis of 500ns MD simulation of Aβ40 monomer from PDB ID: 1AML. Representative structure for each cluster is shown below the cluster node together with the relative population percentage. Thickness of connecting links indicate the relative transition frequency. Proteins are shown in cartoon representation using the VMD secondary structure color scheme.

of the entire population. The representative structure of this cluster contains a large α-helical segment in the central region of the peptide and is otherwise unstructured. Two copies of this representative structure were used to characterize the dimer conformation.

4.3.2 Characterization of Aβ40 Dimer Formation

Two dimer systems were generated by randomly placing the obtained monomer structure in orthogonal (90°) or parallel orientations, with respect to the long peptide axis, at 4nm CoM distance, **Figure 4.2 right**. Both dimer conformations were then simulated for 4μs, using the same force field and water model as the monomer simulation, on the special purpose Anton supercomputer.

To determine if the dimer simulations had reach equilibrium, we monitored the time-dependent change in the secondary structure of the peptides, **Figure 4.2 left column**. The α-helix and β-structure content for both configurations were obtained using the method from ref. (176). The graphs show that for the orthogonal configuration the α-helical content fluctuates with a decreasing tendency up to the 1μs mark, after which the helical portion increases over the next μs, **Figure 4.2A**. Meanwhile, the β-content remains stable at approximately 5%, with minor fluctuations, until approximately 3.5μs. After 3.5μs a conversion from α-helical to β-structure is observed, with β-content reaching a maximum of ~12% at the end of the simulation. The parallel configuration on the other hand does not display similar behavior, both α-helical to β-structure content fluctuate throughout the simulation, with averages of approximately 15% and 5%, respectively, **Figure 4.2B**. This suggests that, for both configurations, a local equilibrium state has not been reached.
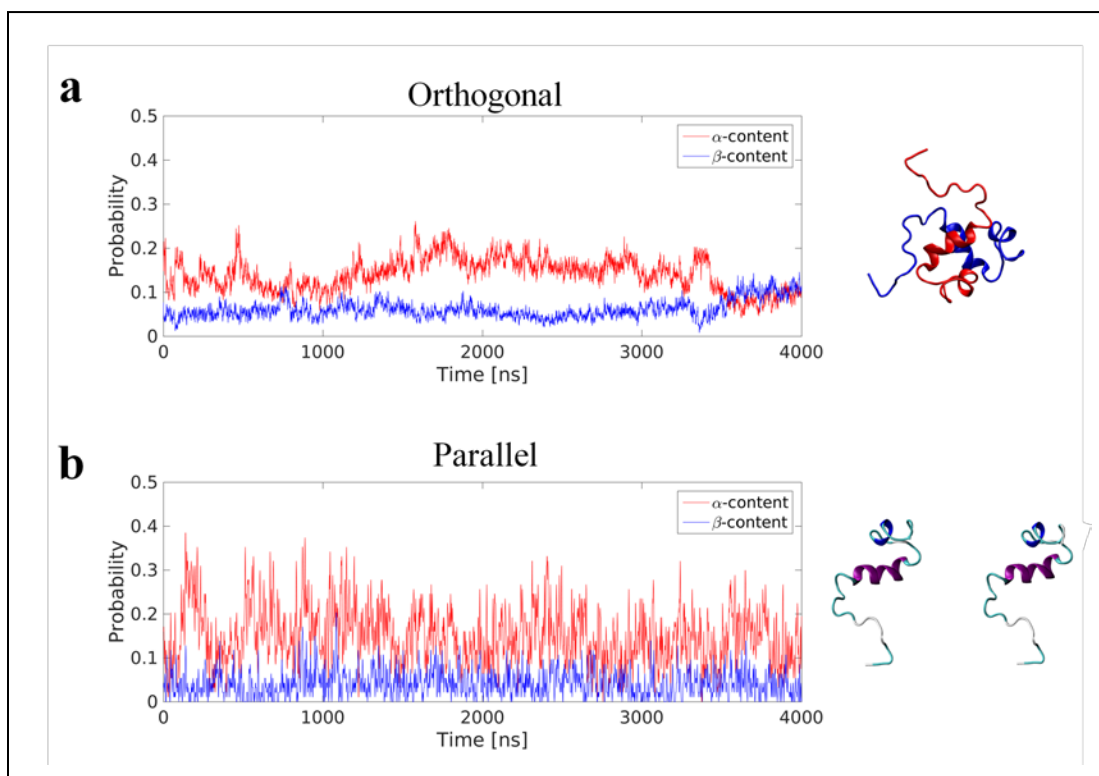
Figure 4.2. Time-resolved change in secondary structure during 4μs cMD simulations of Aβ40 dimers on Anton. Data for Aβ40 dimer in the orthogonal **(a)** and parallel **(b)** starting configuration.

We then used dihedral principal component analysis, in which the artifacts from combining internal and overall motion are minimized, to analyze the energy landscape of the dimer. For both dimer configurations, several distinct energy minima were found, **Figure 4.3**. Furthermore, for both configurations we see that only a small portion of the energy landscape has been sampled. This, in combination with the time-resolved change in secondary structure, suggests the possibility that the dimers are trapped in local energy minima, leading to insufficient sampling of the conformational space. To overcome this issue, we extended the dimer simulation using accelerated MD simulations (see specifics in Methods) to enhance the sampling of the conformational space. It has been shown that the sampling enhancement is several orders of magnitude, furthermore, we and others have successfully employed aMD to characterize amyloid proteins.

Accelerated Molecular Dynamics Simulations of Dimers

The result of the aMD simulations for the dimer is presented in **Figure 4.4**. Several well-defined and separated energy minima were identified for the orthogonal system, **Figure 4.4A**, while the parallel system only has few energy minima that are clustered in the same region of the energy landscape, **Figure 4.4B** . The aMD results were then pooled and the concatenated data set underwent dPC analysis again, **Figure 4.5A**. The snapshots in the figure depict representative structures from the two lowest energy minima. It is evident, that the dimer does not adopt long β-structures but has a mixture of short helices and β-structures.

To analyze the conformational diversity of the dimers we performed cluster analysis using the pooled aMD data. Similar to the analysis performed for monomers, clustering was performed using RMSD of backbone atoms between all pairs of structures
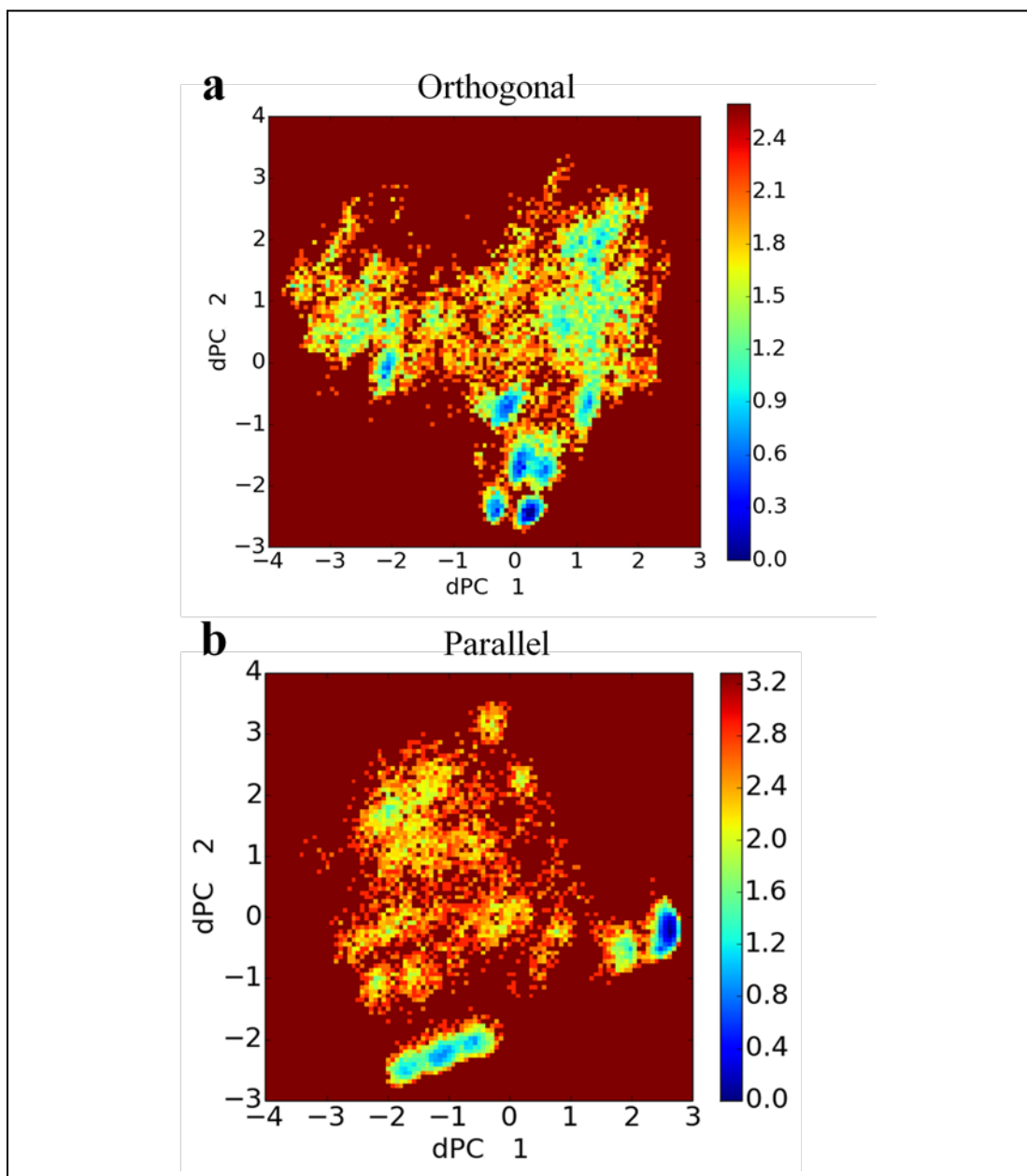
Figure 4.3. Free energy landscape of 4μs MD simulations of Aβ40 on Anton. Energy landscapes of Aβ40 in orthogonal (**a**) and parallel (**b**) configurations. Units of colorbars are in k$_B$T.
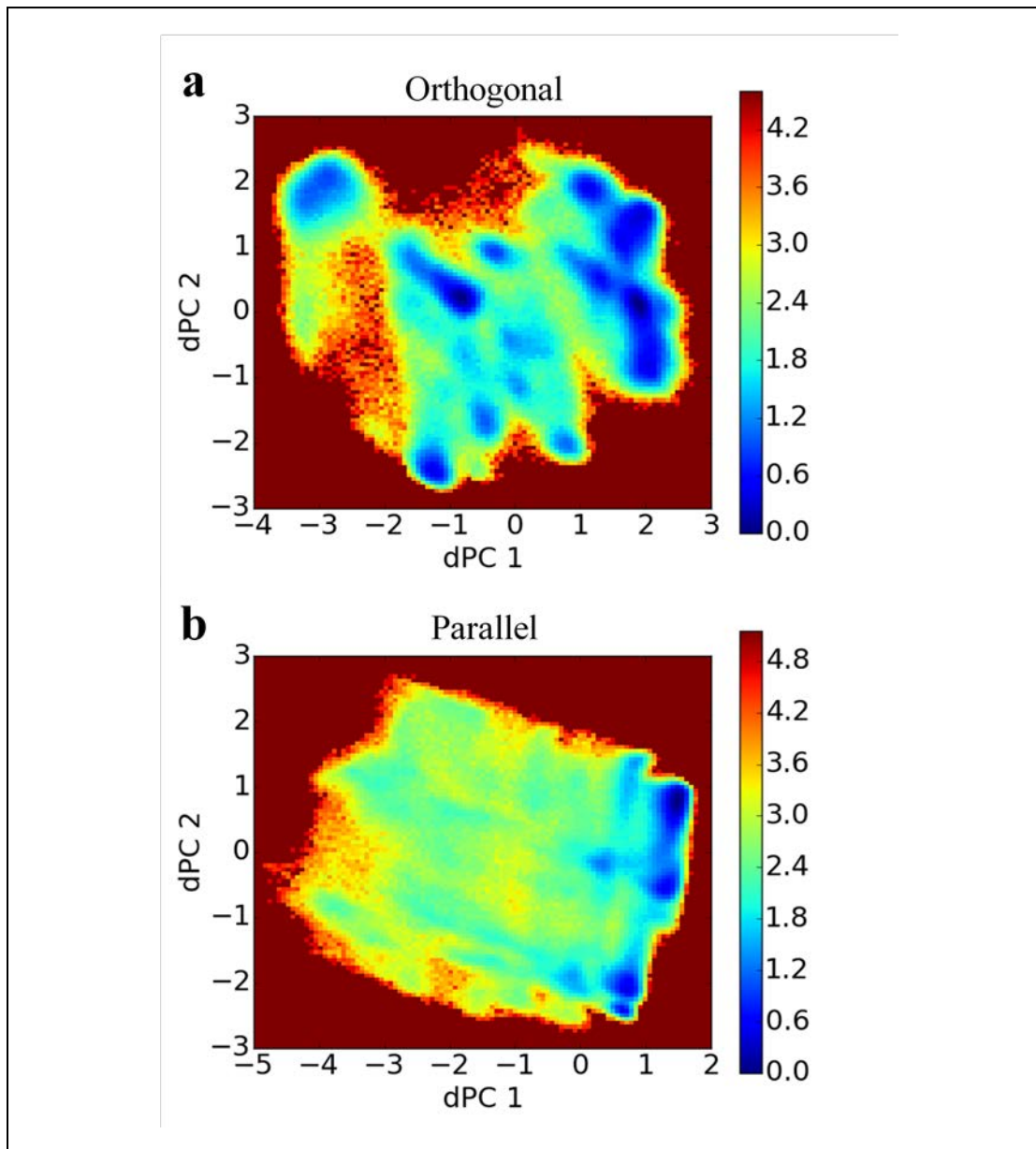
Figure 4.4. Free energy landscape of Aβ40 dimers. Energy landscapes are from 1.5μs aggregate aMD simulations of Aβ40 in orthogonal **(a)** and parallel **(b)** configurations. Colorbar units are in k$_B$T.
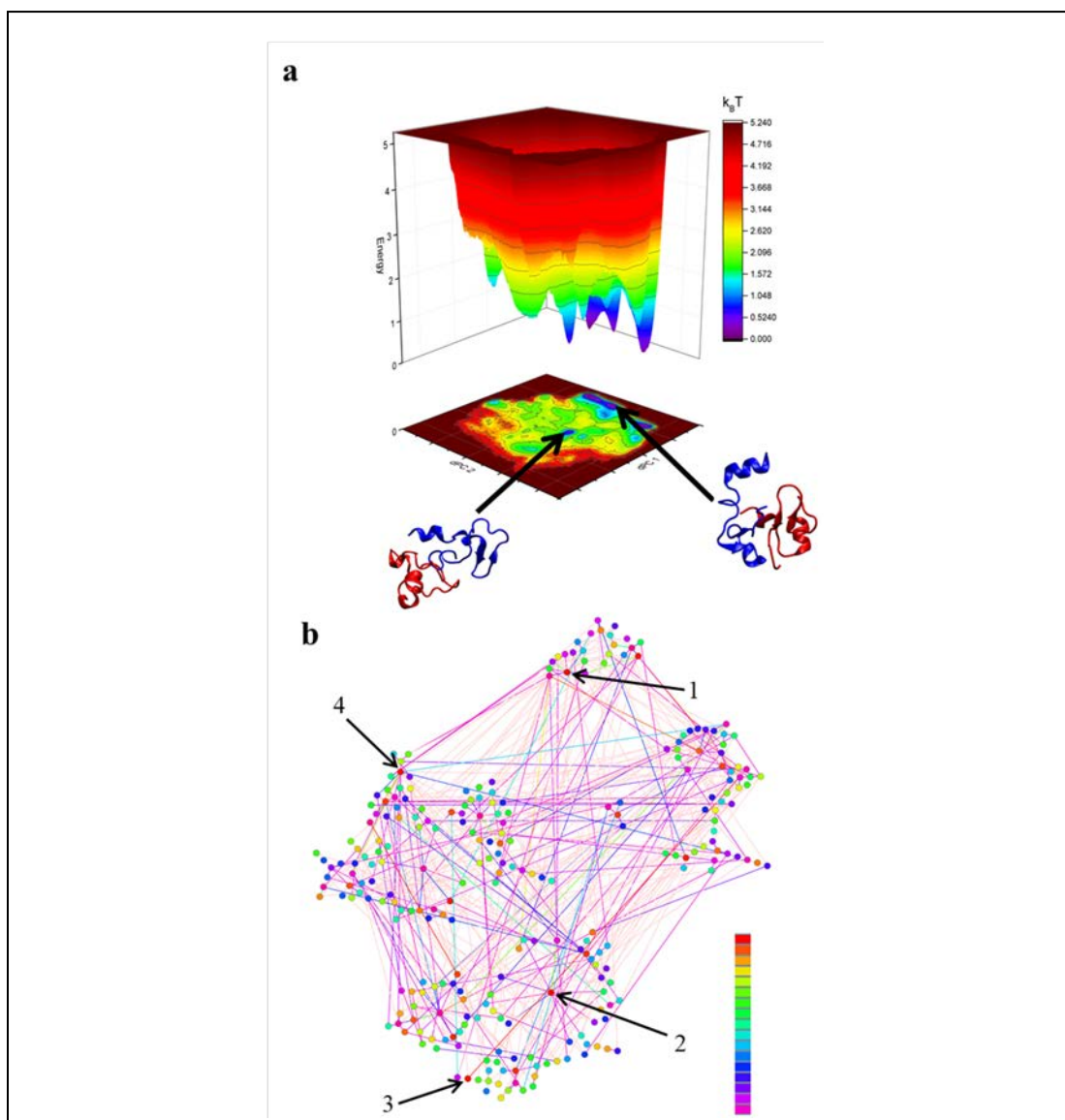
Figure 4.5. Analysis of Aβ40 dimers obtained from 3μs aggregate accelerated MD simulations. **(a)** Free energy landscape based on dihedral principle component analysis of Aβ40 dimers; the two lowest energy structures are shown as cartoons. **(b)** Transition network obtained from cluster analysis of Aβ40 dimers. The four most populated clusters have been highlighted; representative structures are shown in **Figure 4.6**. Node colors indicate the cluster occurrence frequency (red to magenta, highest to lowest), while link color indicates the number of transitions using the same color scheme. Single transitions have been colored pastel orange to decrease color overlap.

Chapter 4: Self-assembly of full length amyloid *β* 40 into dimers

with a cut-off at 3Å and using only data for residues 10–35. In total 1,500,000 unique

structures were used in the analysis, the results of which is shown in **Figure 4.5B** as a

transition map. From the transition map, in addition to identifying groupings of the clusters,

we were also able to identify several key clusters, clusters 2, 4, 9, and 19, that are important

for the structural transition of the dimer. Representative structure for the first 20 clusters

are depicted in cartoon representation and relative populations on **Figure 4.6**. These

clusters combined make up approximately 54% of the total structure population.

Structurally the clusters, with few exceptions, exhibit similar trends of low α-helical and

β-structural content and high degree of unstructured regions. The main difference within

the clusters arise from the different configurations of monomers.

The secondary structure of the dimers was quantified using DSSP. Each monomer

was investigated separately with the results being displayed as residue specific

probabilities, **Figure 4.7A**. Monomer 1 shows greater than 40% propensity for helix

formation in residues 3-7, 11-13, and 25-29. β-structures are overall less likely compared

to helices, however regions 10-30 and 35-38 have on average greater than 20% chance of

β-structures. Monomer 2 on the other hand is more diverse, the helix probability is

localized around residues 11-20, while collectively β-structures are more probable in the

N- and C-terminal segments in residues 3-10 and 21-38, respectively.

Geometrical analysis was then performed on the dimer to determine the solvent

accessible surface (SASA) and the radii of gyration of the monomers within the dimer and

the dimer itself, **Figure 4.7B** and **C**. SASA revealed that residues from the two monomers

are equally exposed and that the C-terminal segments, from residue 30 and up, are the least

exposed segments of the peptides. Furthermore, the radii of gyration for both monomers
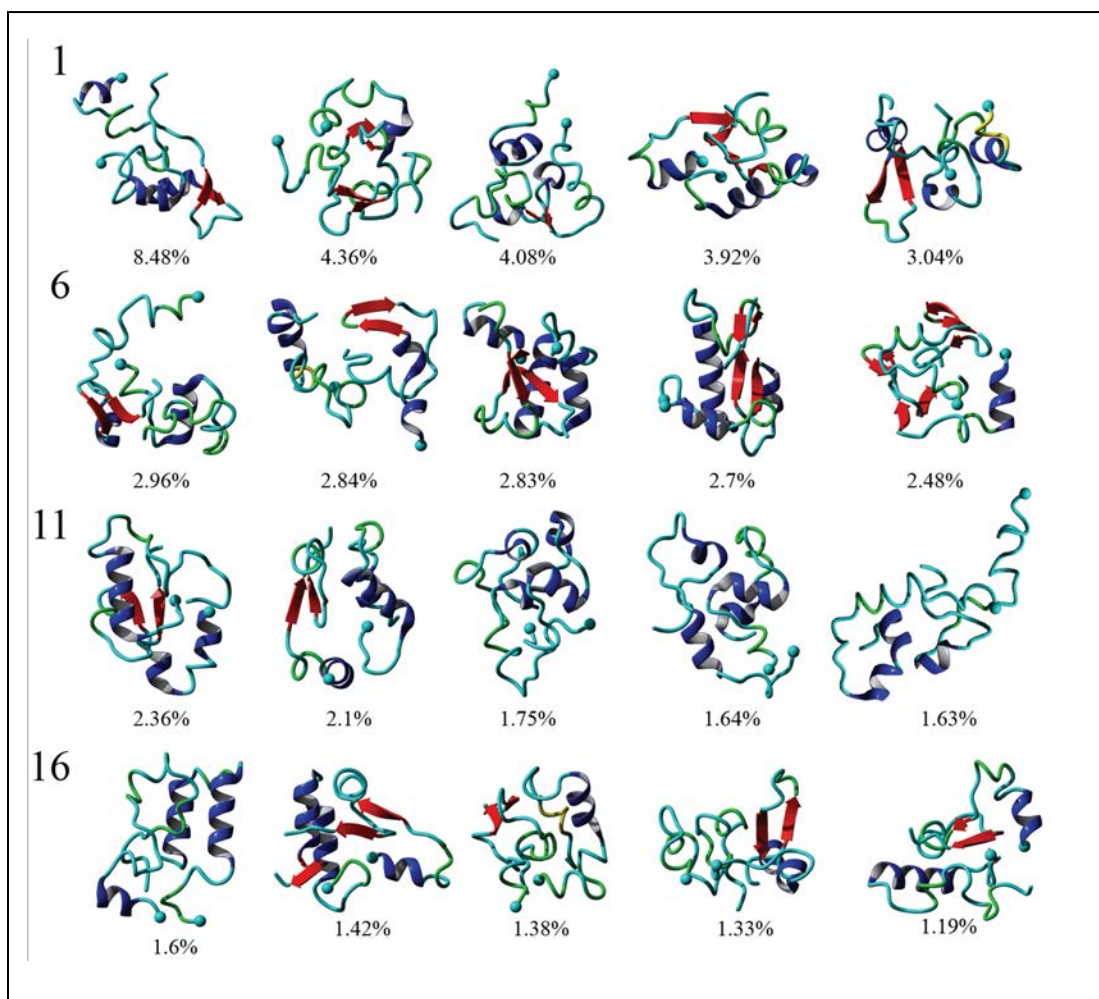
Figure 4.6. Cluster analysis of Aβ40 dimers obtained from 3μs aggregate accelerated MD simulations. Representative structures of the top 20 clusters formed by Aβ40 dimers are presented with relative populations, as percent, for each cluster displayed below each structure. α-helices are colored blue while β-strands are in red. A solid sphere depicts the Cα of Cys residues.
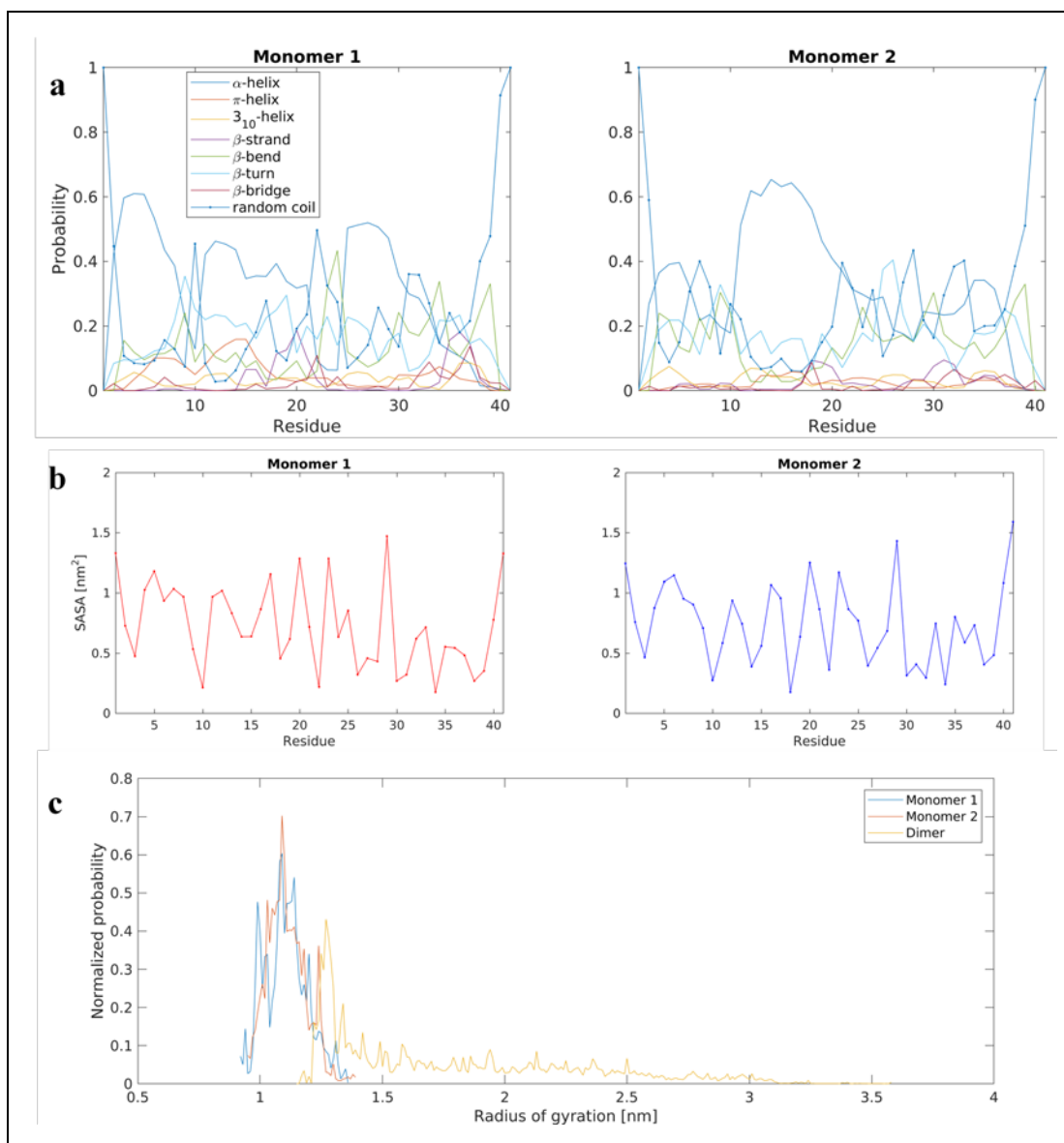
Figure 4.7. Conformational analysis of Aβ40 dimers from 3μs aggregate aMD simulation. **(a)** Population of each secondary structure type, determined by DSSP, for each monomer within the Aβ40 dimer, on a per residue basis. **(b)** The surface accessible surface area per residue for Aβ40 monomers, within the dimer. **(c)** The normalized probability of radius of gyration for each monomer and the dimer of Aβ40.

within the dimer are very similar, **Figure 4.7C**. The dimer is very compact, Rg ~1.3nm, and has the main distribution peak very close to the radii of the monomers.

To identify segments important for the interaction of Aβ40 monomers, we performed analysis of the pair-wise residue interactions. Intra-peptide contact probability maps were generated based on Cα atom contacts within the monomers, **Figure 4.8**. For Monomer 1, interactions in three segments stand out, residues 5-12, residues 16-23, and residues 30-40, **Figure 4.8 top**. The interactions within these three segments reveal that the monomer during the simulations, with high probability, is found in a compact turn-like conformation with C-terminal interacting with the central segment of the peptide. Monomer 2 on the other hand is more dynamic with few residues interacting in the N-terminal and the 16-23 region, **Figure 4.8 bottom**. The interaction patterns of the two monomers reveal that, apart from neighbor residue interactions, the main difference is found in the way the two monomers interact with the 16-23 region; for Monomer 1 the interaction happens with residues 33-38, while for Monomer 2 it is residue 28-32, **Figure 4.9A**.

The inter-peptide interactions of the dimer were obtained using the pair-wise interactions of Cα atom between the monomers, **Figure 4.9B**. The contact map reveals that the interactions between the two monomers occur in the central region of the peptide as well as between the N- and C-terminals and the two C-termini. Comparison of the contact data and the dimer structures, revealed by cluster analysis, shows that the 20 most populated clusters are a mixture of different conformations that all contain N-C terminal interactions, with a few configurations also containing C-C terminal interactions. Further investigation of the inter-peptide interactions using heavy atom contacts, within 6Å, reveals

Figure 4.8. Analysis of intra-peptide interactions of Aβ40 monomers within the dimers from 3μs aggregate aMD. Contact probability maps for Cα atoms of monomer 1, **top**, and monomer 2, **bottom**.
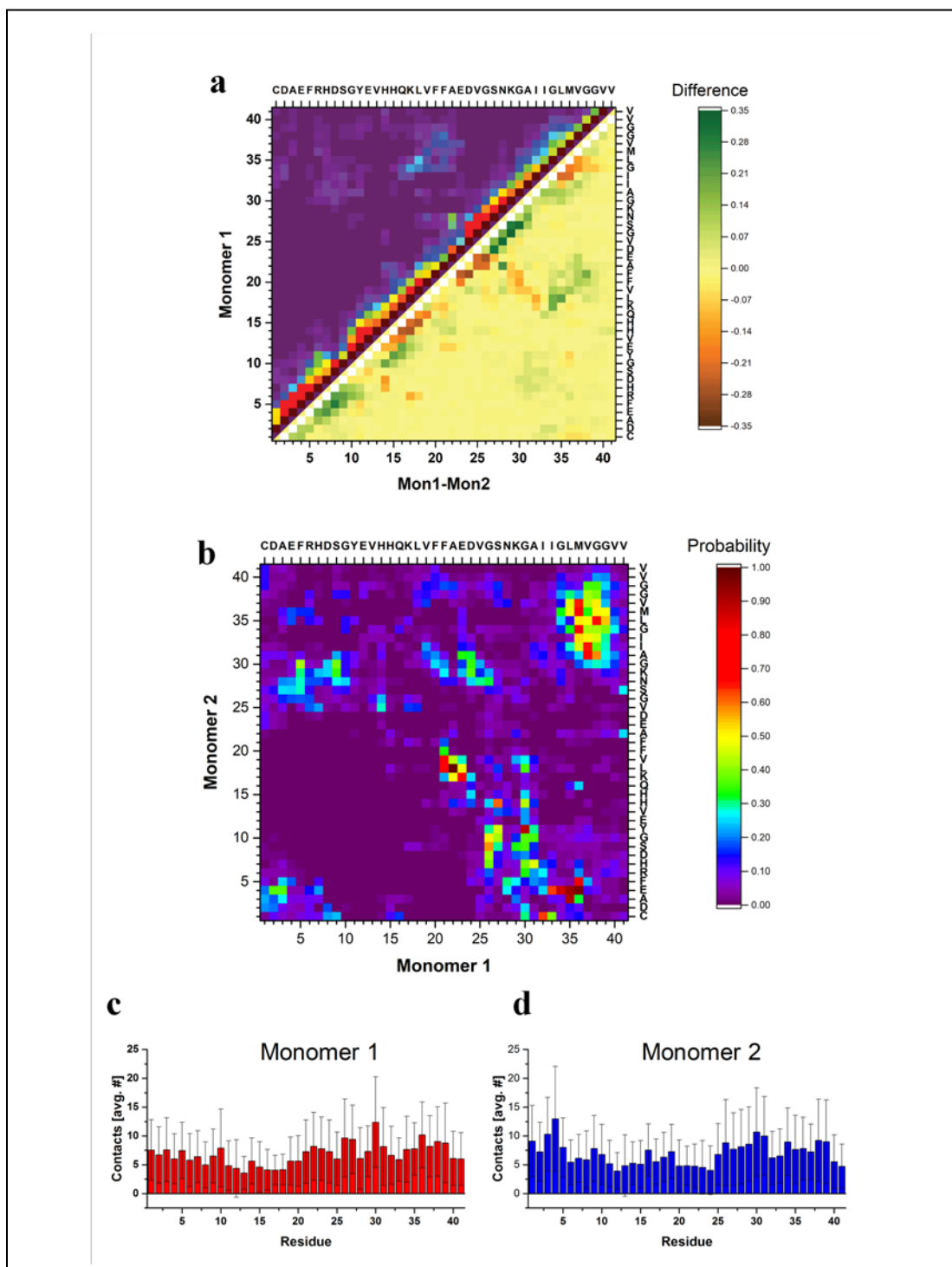
Figure 4.9. Analysis of inter-peptide interactions of Aβ40 dimers from 3μs aggregate aMD. **(a)** The difference in the contact probability between the two monomers and **(b)** the inter-peptide contact probability map for Cα atoms of dimers. **(c)** and **(d)** Show residue specific average number of heavy atom contacts (within 6 Å) between monomer 1 and monomer 2 within the dimer of Aβ40, respectively. Error bars represent standard deviation.

Chapter 4: Self-assembly of full length amyloid *β* 40 into dimers

that the trends found in the Cα contacts are corroborated, **Figure 4.9C** and **D**. Monomer 1 primarily interacts through its central and C-terminal segments, while Monomer 2 interacts through the N- and C-terminal regions.

4.3.3 Validation of Dimer Conformations

To validate the simulation results as well as identify the experimentally relevant conformations we performed Monte Carlo pulling simulations on identified dimer structures. The rupture force and interaction patterns for the top candidates are presented in **Figure 4.10**. The interaction patterns of the simulated dissociation processes were normalized with respect to the experimentally obtained contour lengths. Experimentally observed values for the dissociation force was 56.58 ± 20.47pN (STD), approximated using a Gaussian distribution, with a two-peak distribution of the interaction pattern favoring interaction in the N-terminal and central regions.

The dimer obtained following analysis of the cMD simulations, named "No aMD" on **Figure 4.10**, shows a distinct three-peak interaction pattern, with majority of interactions located in the N-terminal and central regions of the proteins, while the dissociation force is 36.54 ± 18.44pN. Dimer conformations from the two most populated clusters following the aMD simulations produce rupture forces of 61.74 ± 27.5pN and 35.57 ± 17.72pN, respectively. Similar to the cMD dimer, the two aMD conformations produce the distinct three-peak interaction pattern. However, Clu 01 shows a very large C-terminal peak. The dissociation of dimer Clu 01 is statistically similar to the experimentally observed results, using a non-parametric two-sample Kolmogorov-Smirnov with 0.05 significance.
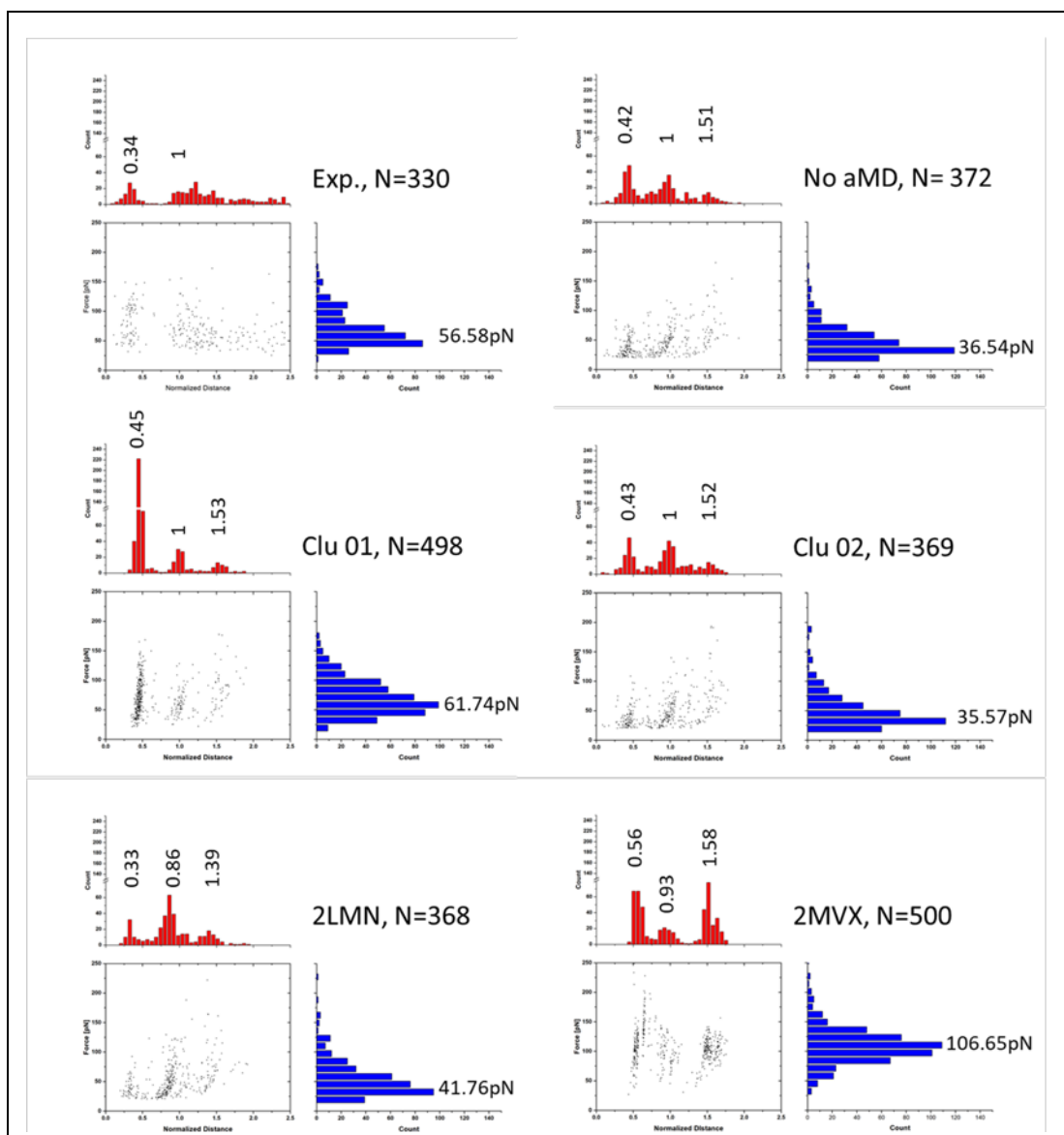
Figure 4.10. Experimental and MCP simulation results of force-induced dissociation of Aβ40 dimers. Each dataset shows a scatter plot of Normalized Distance vs Force, a histogram of Force (blue), and a histogram of Normalized Distance (red); normalization was performed based on the experimentally observed contour lengths. Peak values, obtained using Gaussian distribution function, are presented above each peak of the histogram. Clu 01 and 02 are conformations from **Figure 4.6**; "No aMD" the most populated cluster before aMD simulations; and the bottom row are dimers from fibrils from the PDB. Statistical analysis was performed using two-sample Kolmogorov-Smirnov test with 0.05 significance level; only Clu 01 was statistically similar to the experimental data set, with p>0.066.

To characterize the interaction pattern and the dissociation force of a dimer with high β-structure content, we created two dimer conformations from NMR structures of Aβ40 fibrils (PDB IDs: 2LMN and 2MVX). The two are significantly different compared to experimental results and the results obtained for the cMD and aMD dimers. Although, the fibril dimers contain the three-peak interaction pattern, the patterns are significantly different; for the 2LMN dimer the majority of interactions happen within the central part of the dimers, while for 2MVX dimer the interactions are dominated by the N- and C-terminals.

4.3.4 Comparison with Aβ42 Dimers

To investigate the effect of the two extra C-terminal amino acids of Aβ42, we performed analysis of the Aβ42 dimer using the methodology for Aβ40 dimers. The orthogonal Aβ42 dimer data was from our recent publication (174) while the parallel dimer was from unpublished data.

We generated intra-peptide contact probability maps based on Cα atom contacts within the monomers of the Aβ42 dimers, **Figure 4.11**. Monomer 1 of the orthogonal dimer primarily forms intra-peptide contacts through interactions between residues 1-5 and 24-29 and residues 6-11 and 35-41, **Figure 4.11A**. Monomer 1 also forms a turn structure utilizing residues 25-34, while Monomer 2 has strong propensity for N-terminal nearest-neighbor interactions as well as interaction between residues 30-35 and 14-23. Monomer 1 of the parallel dimer is compact and interacts through segments 1-5 and 10-15 and 10-16 and 35-42, **Figure 4.11B**. Monomer 2 primarily has a U-turn like conformation and forms

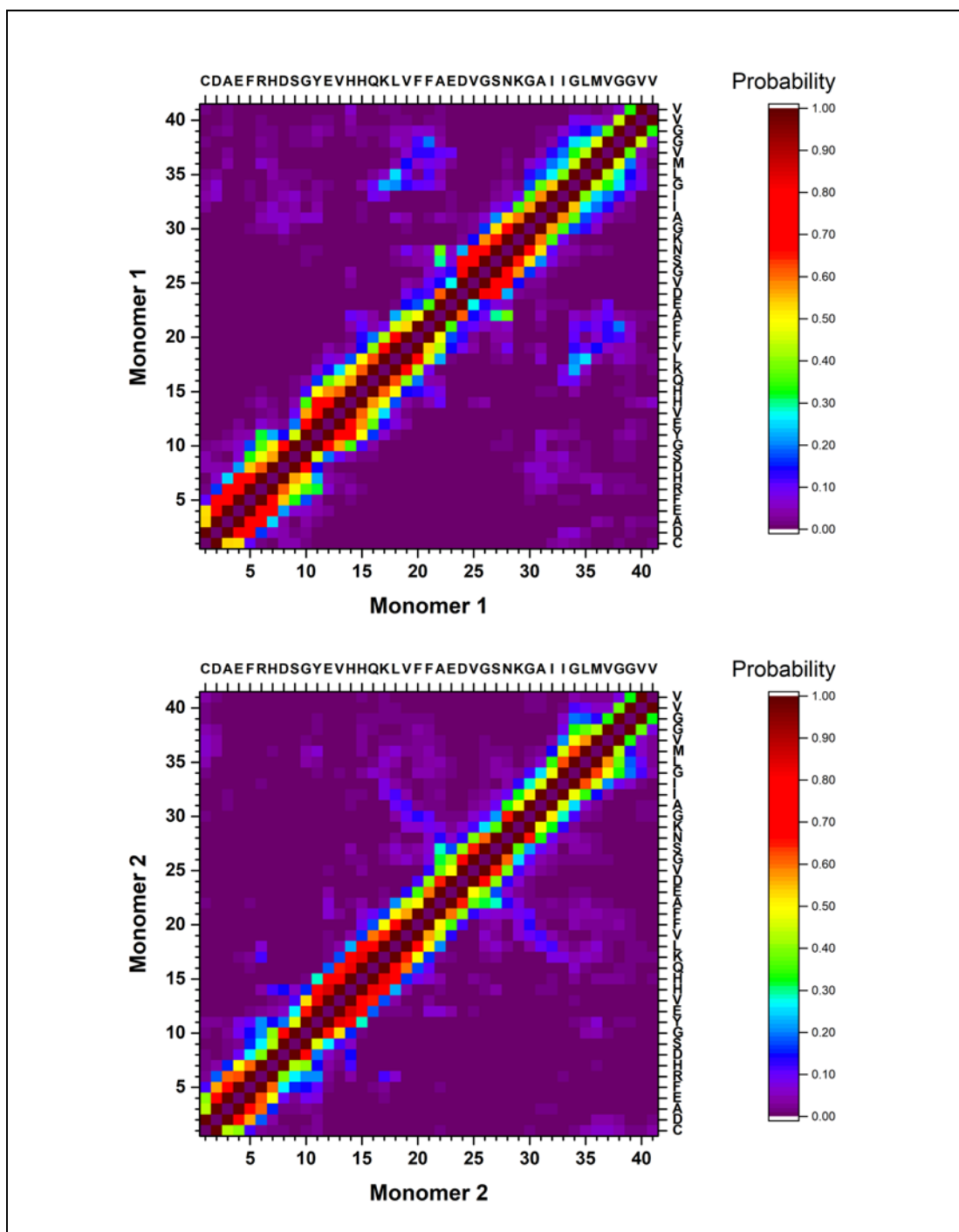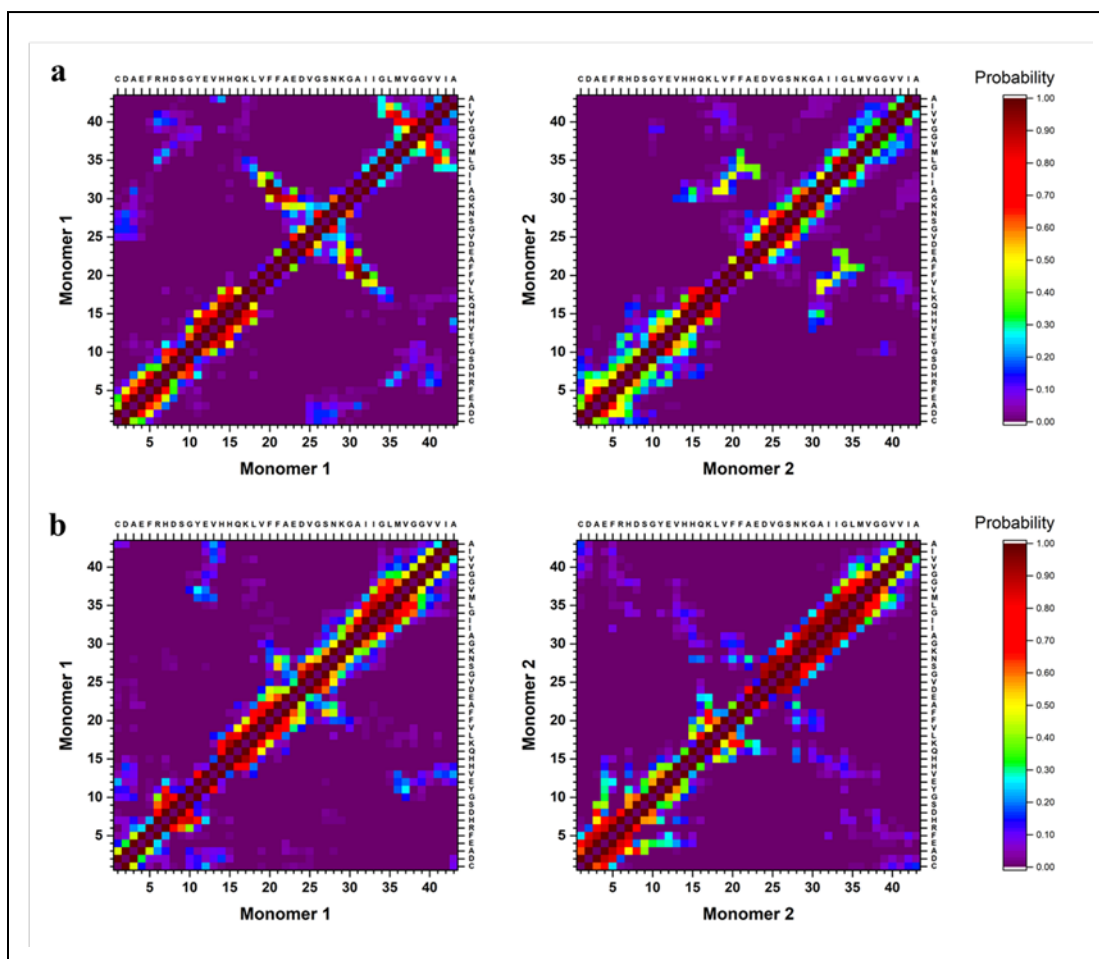**Figure 4.11.** Analysis of intra-peptide interactions of Aβ42 monomers within the dimers from 500ns aMD simulations. Contact probability maps for Cα atoms of orthogonal **(a)** and parallel dimer **(b)**.
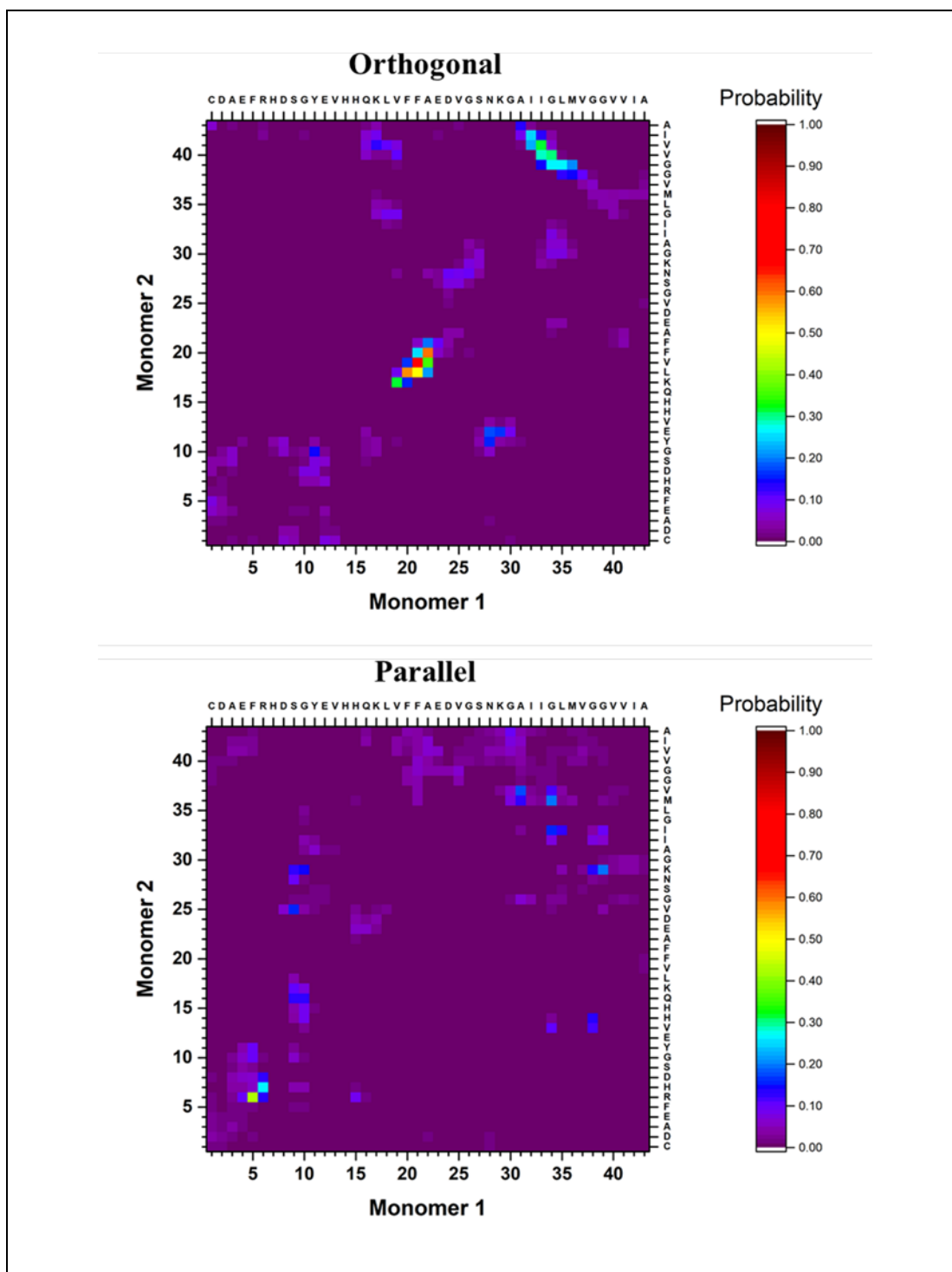
Figure 4.12. Analysis of inter-peptide interactions of Aβ42 dimers from 500ns aMD simulations. Contact probability maps for Cα atoms of orthogonal, **top**, and parallel, **bottom**, dimers.

contacts through residues 1-20 and 25-40, many high probability contacts with neighbor residues in the N-terminus are also observed.

The inter-peptide contact map for the two Aβ42 dimers were then generated, **Figure 4.12**. The orthogonal dimer is stabilized by interactions in the central region, residues 16-23, between the two monomers as well as C-C terminal interactions by residues 30-36 and 36-42. Other interactions of 10-20% probability also occur between the N-termini of the two monomers. The monomers in the parallel dimer on the other hand primarily interact through N-terminal and C-terminal residues, segments 5-11 and 30-40.

4.4 Discussion

Although the behavior of Aβ peptides have been subject to numerous studies, our present study adds a substantial amount of data to the discussion. Our computational analysis of the aggregation of Aβ40 into dimers reveal a broad range of peptide structures and very dynamic dimers. The data show a low propensity for stable secondary structure elements in the monomers of the dimers. In particular, we did not identify significant β-conformation in the monomers within the dimer, **Figure 4.6**.

The equilibrated monomer structure, used as the initial conformation to characterize the dimerization process, is in line with recent data obtained using NMR and simulations of the Aβ proteins, which showed that the monomer has unstructured segments and can assume helical secondary structure (51, 183). Another interesting feature of the monomer structure is the presence of a turn on each side of the central helix, the turn conformation is believed to be the first folding event in the structural transition of Aβ proteins and important for the aggregation process (31, 89, 90).

Interaction of two monomers lead to conformational transitions within the monomers, accompanied by change in local structure of the peptides, leading to the formation of a stable dimer. Investigation of the dimer structures showed that the Aβ40 dimers exhibit a heterogeneous ensemble of conformations that contain a diverse number of structures. Dimers are primarily stabilized by interactions in the N-terminal region (residues 5-12), in the central hydrophobic region (res. 16-23), and in the C-terminal region (res. 30-40); with inter-peptide interactions focused around the N- and C- terminals. The 20 most populated clusters are a mixture of different conformations that all contain N-C terminal interactions, with a few configurations also containing C-C terminal interactions. Interestingly, similar observations regarding the interaction pattern of Aβ40 dimers have been presented recently (184). Tarus *et al.* showed that regions, identified in our simulations, were also interacting and important for the stability of the dimer. However, unlike the dimer conformations identified here, their dimers contained significant β-structure content. More recent findings, (185), from the same group show that the dimers structures are more diverse and do not contain a large extent of β-structure, and that the dimer is stabilized by nonspecific interactions. This is in agreement with our findings, and also may explain the role of structural plasticity in the interactions of Aβ oligomers with binding partners and ultimately their toxicity. The structural flexibility of the dimer may also play a role in the aggregation progression, where the free energy cost of transitioning from less ordered states is much less compared to dimeric states with high level of ordered β-structures.

We validated the dimer conformations using MCP approach to simulate the force-induced dissociation of the dimers and compared the obtained force and interaction patterns

with experimental results. The simulations were performed at conditions identical to the experimental ones and allowed us to identify the dimer conformation of Clu 01 as the most probable dimer probed during experiments. Probing of dimer conformations with high degree of β-structure content, adopted from fibril structures, showed that such dimers produce dissociation forces significantly different compared to experiment as well as our simulated dimers. Furthermore, the interaction pattern of high β-content dimers was strongly shifted compared to experiments.

Our results indicate that the presence of the two additional C-terminal residues of Aβ42 does not provide significant stability to the dimer conformation. However, the spatial orientation within the dimer as well as the inter-peptide interaction pattern of the monomers are significantly different. These finding are in line with recent finding about the monomeric Aβ peptides (183), which show that while the two peptides show similar structural elements their conformation are different, and that in turn has a large effect on the inter-molecular interactions of the peptides.

4.5 Conclusions

We showed, through the use of computer simulations, the initial stages of Aβ40 oligomerization by examining the transition of monomers to dimers and characterizing their dynamics properties. Furthermore, we explored the differences between dimers of Aβ40 and Aβ42.

All-atom MD simulations allowed us to structurally characterize Aβ40 dimers. Structures were organized in clusters, with ~54% represented in the 20 most populated clusters. These clusters were further narrowed down to four by the comparison with AFM

force spectroscopy results. Dimers are stabilized by interactions in the central hydrophobic region (residues 17-21) as well as N-C terminal (res. 1-10 and 30-40) interactions, through hydrophobic interactions and H-bonds. Aβ40 dimer did not show parallel in-register β-sheet structures, as one may expect based on the known structures of Aβ fibrils. Comparison of Aβ40 to Aβ42 dimers revealed differences in their conformations. Aβ40 dimers are stabilized primarily by interactions within the central hydrophobic regions and the N-terminal regions, whereas Aβ42 dimers are stabilized by interactions in the central and C-terminal regions. Aβ40 dimers are more dynamic compared to Aβ42 dimers. Comparison, based on MCP simulations, between Aβ40 and Aβ42 showed that overall, the dimers of both alloforms exhibit similar interaction strengths. However, the interaction maps, and more importantly the patterns, clearly show differences.

Chapter 5.   INTERACTION WITH SURFACES PROMOTES AGGREGATION OF AMYLOID PROTEINS

5.1 Introduction

The amyloid cascade hypothesis remains the major underlying hypothesis of *in vitro* and *in vivo* studies related to the molecular mechanisms of amyloid aggregation causing neurodegenerative diseases, despite the fact that it cannot explain all phenomena related to the development of these diseases (186). A strong support for the amyloid cascade hypothesis comes from recent studies, that demonstrated that antibody-based immunotherapy against Aβ improved cognition in a dose-dependent manner (187). Evidence of similarities of structural features of aggregates extracted from amyloid plaques with those of Aβ aggregates assembled *in vitro* provide additional support for the use of *in vitro* Aβ aggregation studies for understanding Aβ structural dynamics *in vivo* (32). However, there is a serious complication with translating current knowledge about amyloid aggregation *in vitro* to understanding the aggregation process *in vivo* - namely, the concentration of amyloidogenic polypeptide are dramatically different *in vivo* versus *in vitro*. For example, whereas the critical concentration for the spontaneous aggregation of Aβ peptide *in vitro* is in the micromolar range, physiological concentrations of Aβ are in the low nanomolar range (188, 189); at such low concentrations of Aβ *in vitro* aggregation cannot occur.

Recently, we found that dimers of α-synuclein (α-syn) could be assembled at nanomolar concentrations if the target monomer is tethered to a surface (101). These data led us to hypothesize that binding to a surface can be a factor dramatically facilitating the aggregation process. This hypothesis is supported by recent studies, in which the assembly

of large α-syn aggregates on a glass surface was observed with the protein concentration in the nanomolar range (190).

In the present study, we developed a systematic approach enabling us to directly test our hypothesis. We used full-length Aβ protein (Aβ42), its aggregation-prone segment Aβ(14-23) peptide, and the full-length α-syn. The experiments demonstrate that, at nanomolar concentrations, all peptides assemble into aggregates on mica surfaces, while essentially no aggregation occur in the bulk solution. Computational modeling allowed us to characterize the mechanism of the accelerated on-surface aggregation process; revealing that the interaction of monomers with the surface causes a conformational change in the monomer that allow it to rapidly form dimers. The interaction with surface is a dynamic process, and once formed, the dimers are able to dissociate and re-associate with the surface; this is believed to allow dissociated aggregates to act as seeds for the aggregation in bulk solution. Given that the on-surface aggregates are oligomeric in nature, which are known to be the most neurotoxic species, we hypothesize that prevention of the on-surface aggregation could block the progression of the disease-prone process and can be considered a means for the development of future preventions and treatments for Alzheimer's and similar neurodegenerative protein aggregation diseases.

5.2 Methods

5.2.1 Aggregation Studies

Detailed description of the experimental procedures are found in ref. (191). Briefly, Aβ(14-23) (HQKLVFFAED), Aβ42, and α-syn (A140C mutant) in 10mM sodium phosphate buffer (pH 7.4) were incubated in presence or absence of 1-(3-aminopropyl) silatrane

(APS) functionalized mica surfaces to determine the effect of surface on aggregation. AFM imaging under ambient condition and *in situ* time-lapse AFM imaging was used to characterize the aggregates.

5.2.2 Molecular Dynamics Simulations

Interaction with Mica Surfaces

Molecular dynamics simulations were conducted using NAMD v 2.10 and employing CHARMM27 force field (192), extended with INTERFACE FF v1.5 (INTFF) parameters for mica (193), and the TIP3P water model (145). A single layer of mica, spanning 52x54Å, was constructed using the INTFF provided structures. Two monomers of Aβ(14-23) were then placed at CoM distance of 2nm above the mica surface. The initial monomer structure was adopted from ref. (100). To mimic the experimental design, a Cys residue was added to the N-terminus of the peptide. The index of this Cys residue was set to 0 to keep the context of the other residues as the actual Aβ42 protein. Because the behavior of the cations on the mica surface is not well understood, we performed simulations of two different mica surfaces: one, which allowed the K cations to freely move during the simulation, called Mica1, and another system where the K cations were restrained to their crystal positions as obtained from (194), called Mica2. Both systems were then solvated with TIP3P water. Na^+ and Cl^- ions were then added to neutralize the charges and maintain an ionic concentration of 150mM. Other details of the simulations setup were adopted from our previous work (100). 20ns NVT simulation was then performed. After which 520ns NPT production simulation, at 1bar and 300K, were carried out for each system using Crane at HCC and Comet at SDSC.

Interaction with Lipid Bilayer

An equilibrated bilayer containing 128 1,2- didodecanoyl-*sn*-glycero-3-phosphoethanolamine (DLPE) molecules was obtained from http://www.fos.su.se/~sasha/SLipids and used together with Slipids force field parameters (195) to simulate the interaction of Aβ(14-23) with the bilayer. Three systems were simulated, a single monomer, two monomers, and two monomers on each side of the lipid bilayer. The Aβ(14-23) molecules were placed 2nm CoM above the lipid head groups. The rest of the simulation parameters, steps, and duration were the same as the mica simulations.

Analysis of MD Simulations

Analysis of interactions with mica was performed on a data set which had discarded the first 20ns of the NPT simulation. The interaction between peptides was examined using the COM distances between each of the peptides. Likewise, the minimum distance between the peptide and the mica layer was also calculated using the CoM of each peptide and the Si atoms of the mica surface, this was done using *g_distance*.

Similarly, for the DLPE system, the distances were calculated with respect to the PO4 groups. Additionally, the backbone interactions of each of the monomers were also monitored using *g_mindist*. To follow the frequency of interaction of each of the peptides as they interact with the surface, the number of contacts between peptide backbone and the surface were monitored; contact being defined as distances less than 1nm. Furthermore, the area per lipid (APL) for each of the simulated bilayer systems was calculated using Dirichlet tessellation to obtain Voronoi diagrams. The GridMAT-MD approach was used to perform the tessellation every ns, using the PO4 groups of each bilayer as the reference,

and with a resolution (grid spacing) of 1Å (196). In addition, membrane thickness was also calculated based on the same reference group.

5.3 Results

5.3.1 Experimental Characterization of On-surface Aggregation

To directly test the hypothesis that surface interactions facilitate the self-assembly of amyloidogenic polypeptides, we performed systematic AFM studies of the on-surface aggregation of Aβ(14-23) peptide, full-length Aβ42, and α-syn protein at the nanomolar range, **Figure 5.1**. Quantitative characterization of the aggregates was performed based on total number and volume of aggregates at all incubation time points, and show that the presence of surface significantly enhances the aggregation of all peptides while at similar concentrations practically no aggregates are formed in bulk experiments.

We then performed *in situ* time-lapse AFM imaging experiments; in which images were taken continuously over the same area after injecting the amyloidogenic polypeptide solution onto the functionalized mica surface. Analysis of these aggregates show that the number of aggregates increases in an almost linear fashion, **Figure 5.2**. Interestingly, comparison of images, adjacent in time, demonstrate the dynamic nature of the aggregation process; aggregates are formed, can grow, and are able to dissociate from and re-associate with the surface. Aggregates of Aβ42, dissociated from the surface, were quantified and compared to the aggregates found on the surface and in bulk, **Figure 5.3**. Aggregates formed on and dissociated from the surface where, at all time points, greater than those found in bulk experiments. Moreover, the volumes of the dissociated aggregates were significantly larger compared to the bulk aggregation experiments.
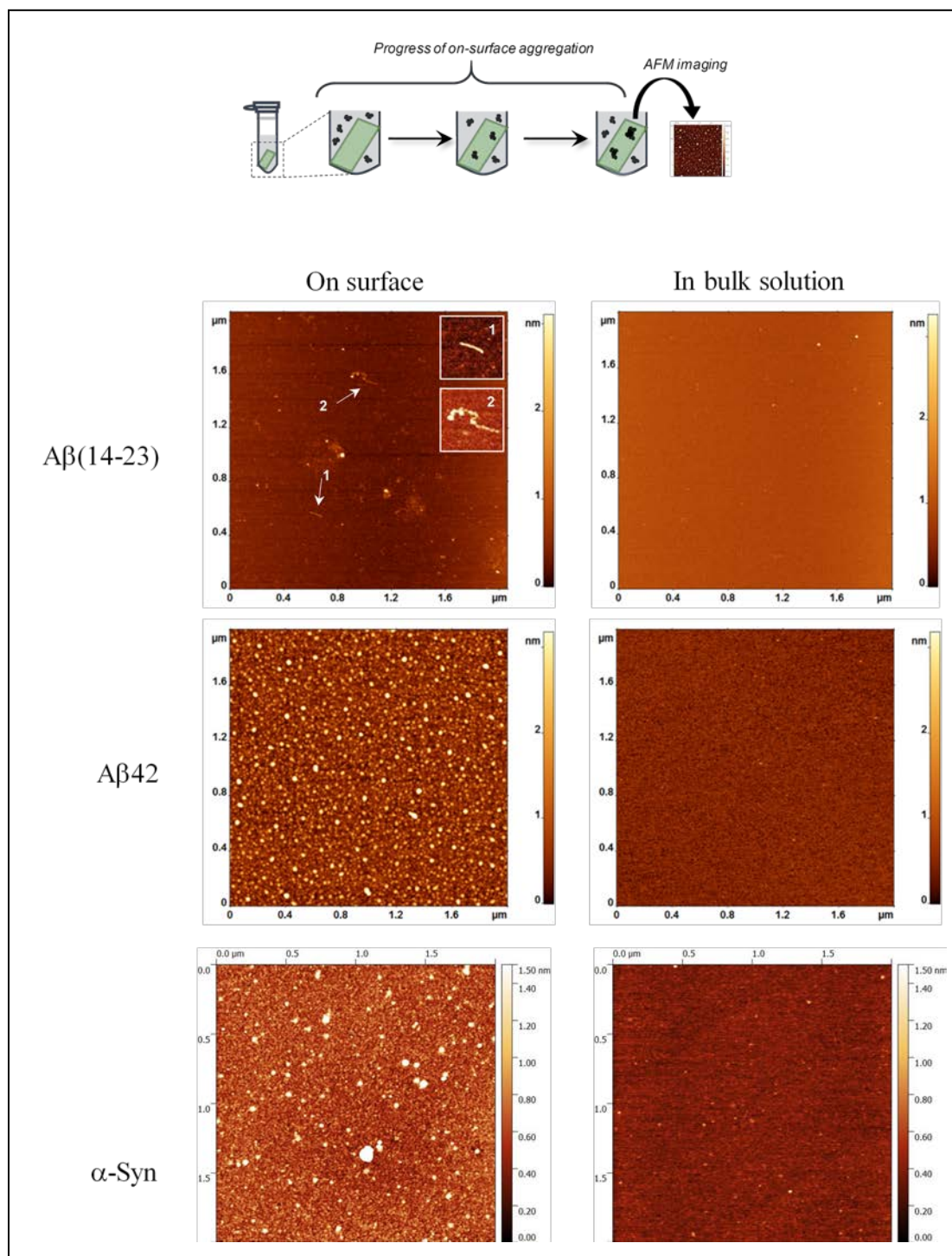
Figure 5.1. Effect of surface on the aggregation of amyloidogenic polypeptides. Schematic of the experimental setup used to investigate surface effect is shown on **top**. APS-functionalized mica surfaces were incubated in protein solutions. At designated time points, mica was removed from the solution, rinsed, dried, and then imaged using AFM. Representative AFM images of aggregates of Aβ(14-23) peptide, full size Aβ-42, and α-syn protein are shown below the scheme in listed order. **Left** column shows representative images from on-surface aggregation experiments, while **right** shows images of the aggregates obtained from bulk incubation. All images are of the 48hr samples. Aβ polypeptide concentrations were 100nM, while α-syn was 10nM for the respective experiments.
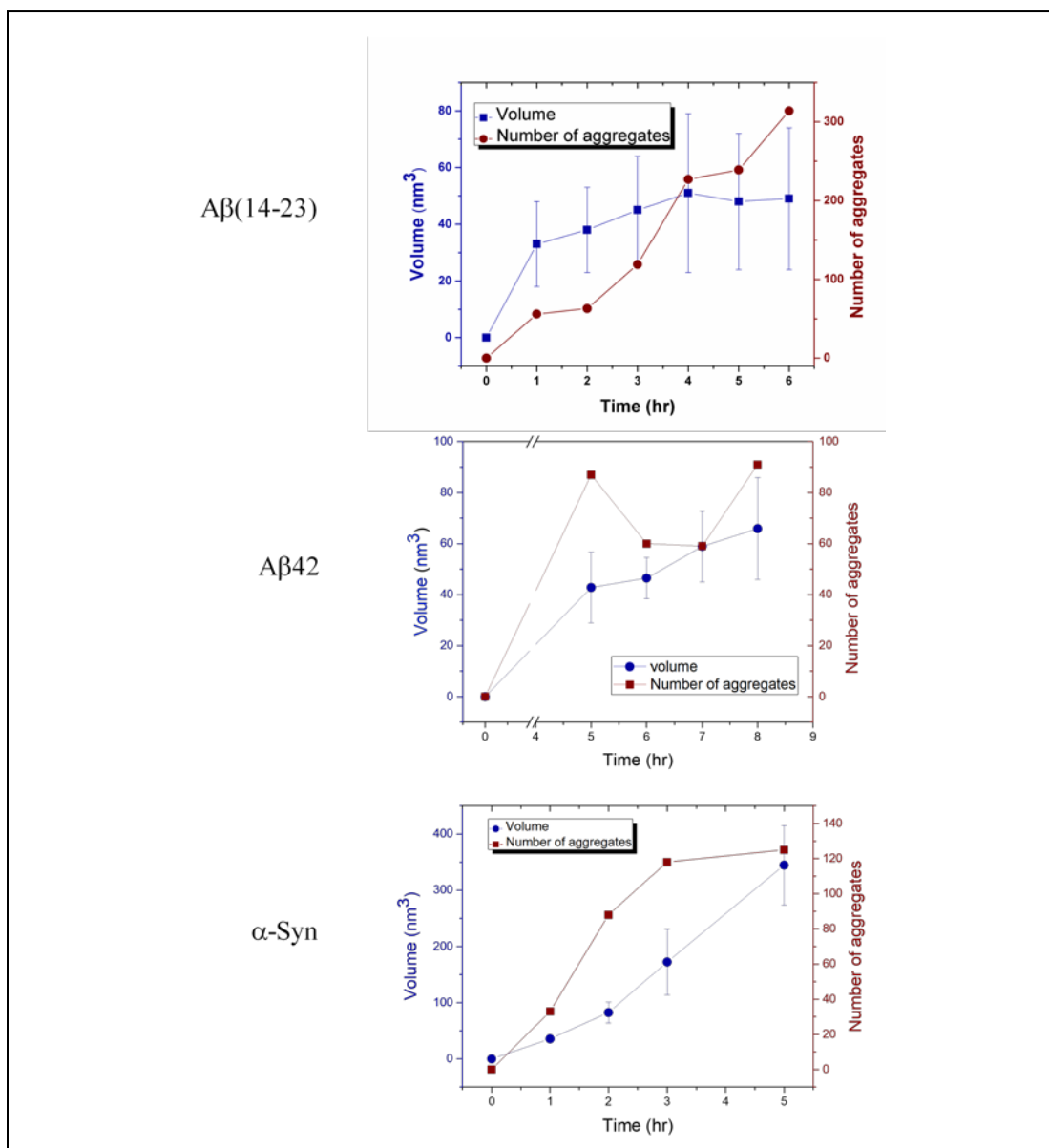
Figure 5.2. *In situ* time-lapse imaging of on-surface aggregation. Volume and number of particles observed as they appear on topographic AFM images after the addition Aβ(14-23), **top**, Aβ42, **center**, or α-syn, **bottom**, protein solution to the functionalized mica surface.
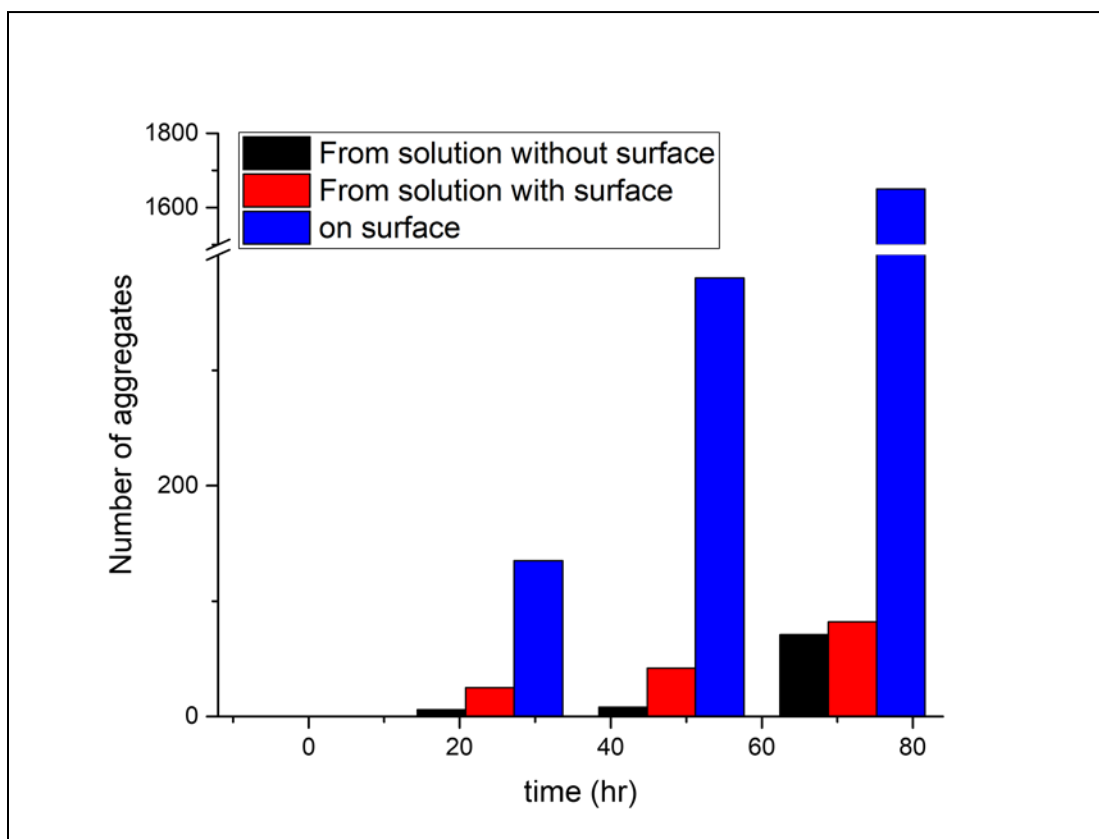
Figure 5.3. The effect of surface on the accumulation of Aβ42 aggregates in solution. Two sets of test tubes were used in parallel using the same Aβ42 solution. One set contained functionalized mica surfaces. At times 0, 24hrs, 48hrs, and 72hrs, 10μl protein solution was removed from each tube and deposited on functionalized mica to be analyzed using AFM. The diagram shows number of aggregates obtained for bulk incubation (black bars), for the tube containing mica surface (red), and on-surface aggregates (blue).

5.3.2 Computer Modeling of the On-surface Dimer Formation of Aβ(14-23)

In order to understand the effect of the surface on aggregation and reveal the mechanism of aggregation, we performed all-atom molecular dynamics simulations of interactions of Aβ(14-23) monomers with mica surfaces, **Figure 5.4**. Two systems were simulated, Mica1 and Mica2, with initial monomer structure being adopted from ref. (100); for detailed description of the simulation parameters please see the Methods section.

The interaction of two peptide monomers with each mica surface was simulated. In the Mica1 system, an Aβ (14-23) monomer, A, rapidly interacts with the mica surface; within the first 50ns of the simulation the monomer approaches the surface. The CoM distance to the mica surface and time-dependent secondary structure of the monomers, as characterized using the DSSP method (197), were obtained, **Figure 5.4B** and **C**. Binding of the monomer is accompanied by its structural transformation, going from having a small helical segment to assuming a bend structure, as seen with the change in secondary structure in **Figure 5.4B**. Recruitment of the free monomer, monomer B, happens within the first 100ns of the simulation; the dimerization causes a structural change in the previously free monomer, **Figure 5.4C**. However, the newly formed dimer is only transiently bound to the surface and for the next ~200ns binds and dissociates multiple times, as is demonstrated by the fluctuation of the dimer-surface distance plot in **Figure 5.4B**.

The interaction between the monomers was characterized by the distance between them as a function of time, as shown in **Figure 5.5**. A few snapshots illustrating the peptide structures are indicated along the time trajectories. The surface induces a conformation that
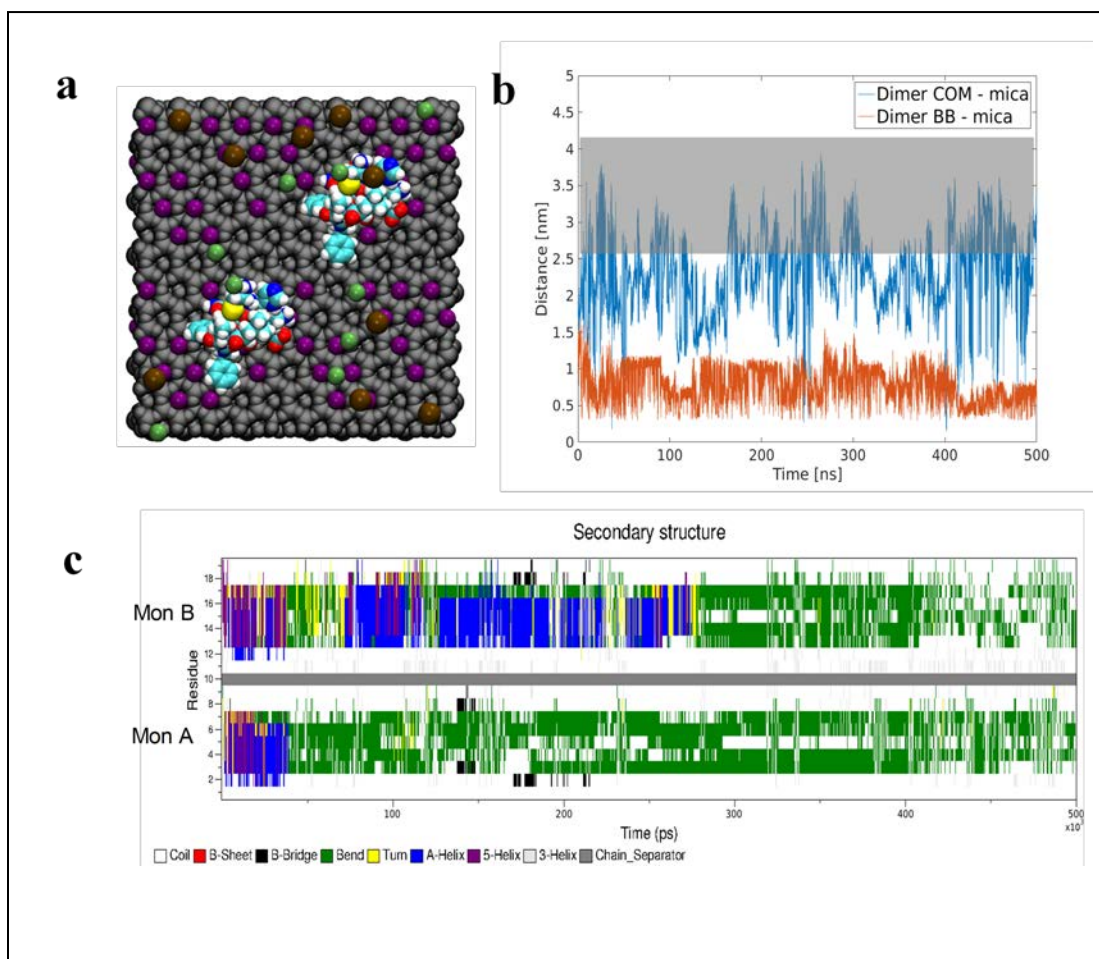
Figure 5.4. Molecular dynamics simulations of on-surface aggregation of Aβ (14-23) dimers. **(a)** Schematic of the simulation system showing van der Waal representation of the atoms. Grey color is the mica structure excluding K cations, K$^+$ atoms are purple, Cl$^-$ are green, Na$^+$ are brown, while peptides are colored using atomic names in VMD. (b) CoM distance between the dimer and mica surface, **blue**, and the minimum distance of the peptide backbone and the mica surface, **red**, for Mica1 system as determined by *g_mindist*. Highlight indicates the distance at which dimer is dissociated from the surface. **(c)** Time-dependent change of the secondary structure of the peptides determined using DSSP. Solid gray bar separates the two monomers.

Chapter 5: Interaction with surfaces promotes aggregation of amyloid proteins
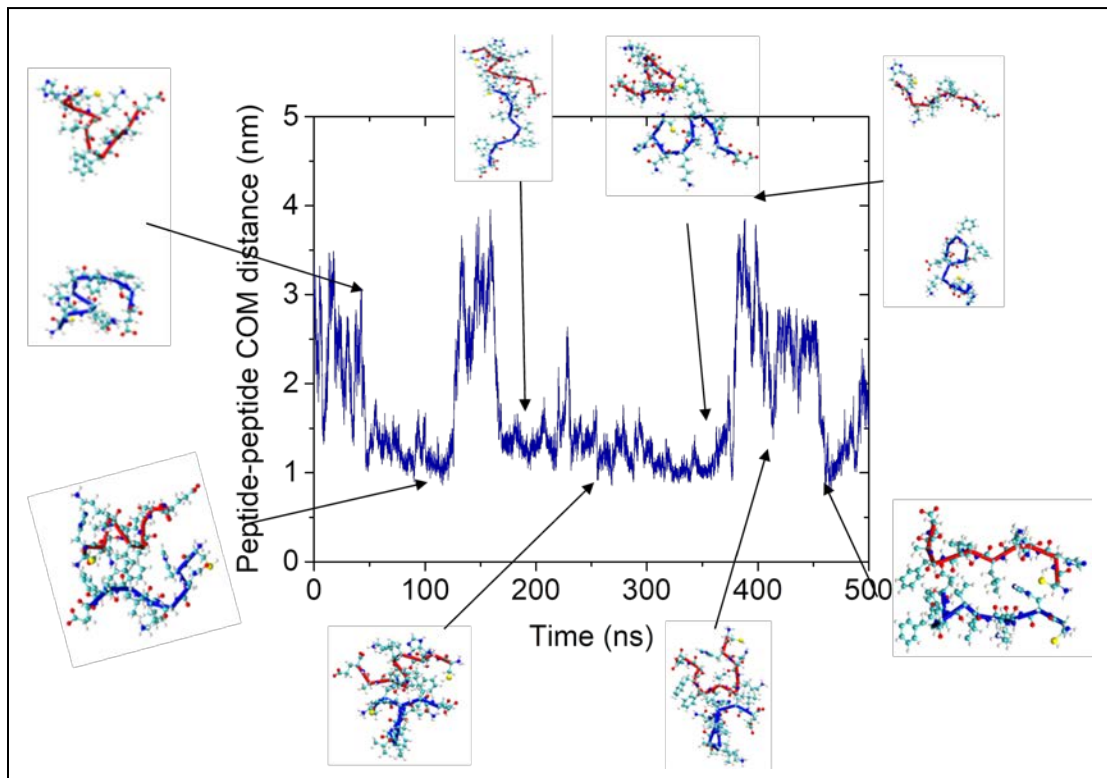
Figure 5.5. Molecular dynamics simulations of on-surface aggregation of Aβ (14-23) dimers. The plot shows CoM distance between the two Aβ(14-23) peptides in the Mica1 system. Key events of the simulation are highlighted with a cartoon representation of the dimer, **blue** represents monomer A and **red** monomer B.

is favorable for dimer formation, as is evident from the rapid recruitment of the free monomer and the formation of a dimer bound to the surface, **Figure 5.5**. The dimers interact with the surface, primarily staying in contact with the surface, through interactions involving a few residues and rarely lie fully on the surface. The behavior of the Aβ(14-23) monomers in the Mica2 system is very similar to the Mica1 system, with the exception that the interaction of peptides with the surface is not as strong, and the conformation of the dimer is less compact, **Figure 5.6**.

5.3.3 Modeling of Aβ(14-23) Interactions with DLPE Lipid Bilayer

We performed MD simulations to characterize the interaction of Aβ(14-23) with a biological model surface, namely DLPE lipid bilayer, which mimics cellular membrane surfaces (198, 199). Three systems were simulated, containing a single monomer, two monomers on the same side of the bilayer, and four monomers, two on each side of the bilayer.

Aβ(14-23) Monomer interacting with DLPE bilayer

Interaction of Aβ(14-23) monomer with the DLPE bilayer was initiated through the C-terminal residues within the first 10ns of simulation, **Figure 5.7**. However, the monomer does not stay attached to the upper leaflet; during the ensuing ~40ns the monomer dissociates from the bilayer surface, traverses the periodic boundary, and interacts with the inner leaflet. Upon interaction with the inner leaflet, the monomer undergoes conformational change, **Figure 5.7B**. Initially, it is attracted through electrostatic interactions with the bilayer, **Figure 5.7B** 47.1ns, followed by a transition to a turn conformation with the peptide backbone interacting with the lipid headgroups, 51.5ns **Figure 5.7B**. Change in the secondary structure, mainly between a bend and a turn
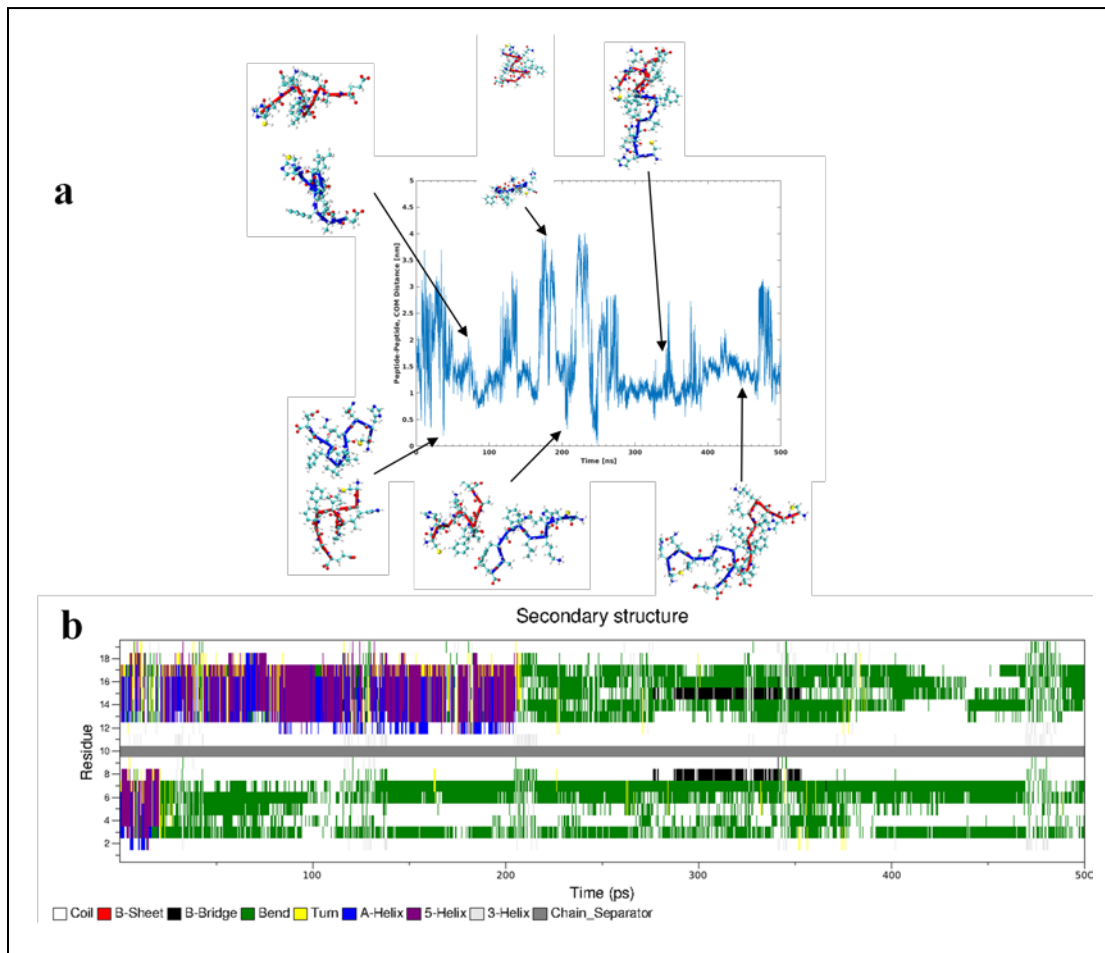
Figure 5.6. Molecular dynamics simulation of interactions of Aβ(14-23) and Mica2, with K+ atoms fixed to their initial positions. **(a)** CoM distance between the two Aβ(14-23) peptides; key events of the simulation are highlighted with a cartoon representation of the dimer, **blue** represents monomer A and **red** monomer B. **(b)** Time-dependent change of the secondary structure of the peptides. Solid gray bar separates the two monomers, with monomer A being below the separator.
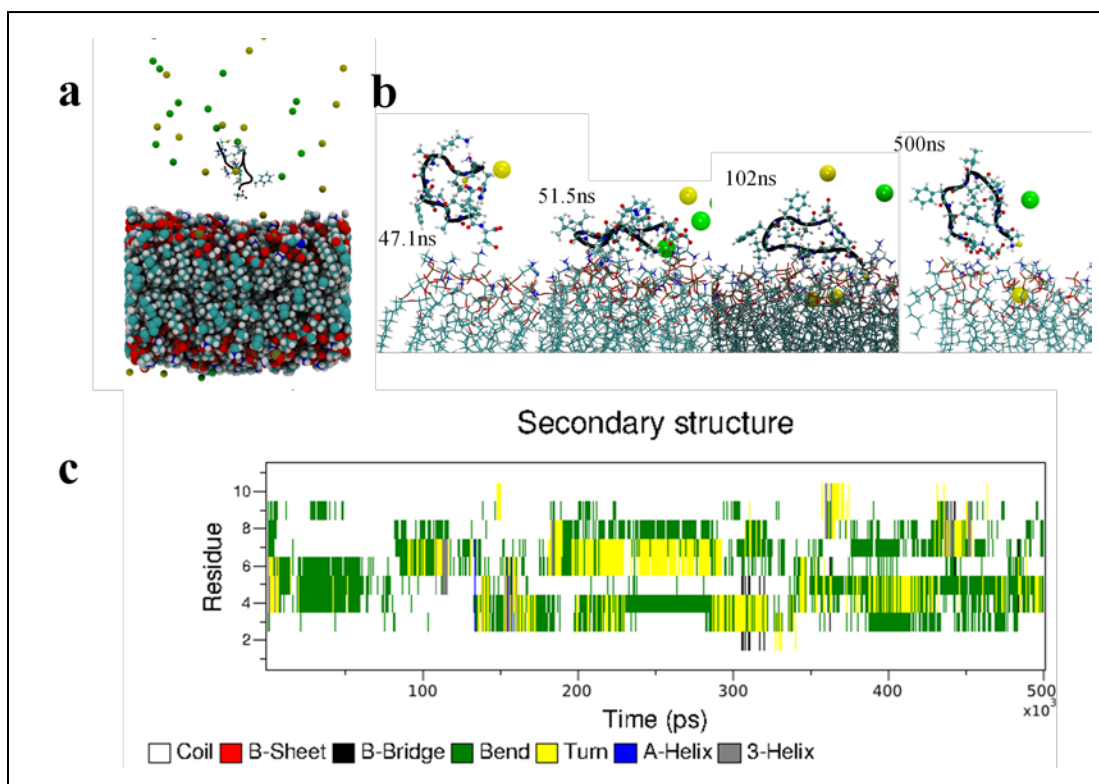
Figure 5.7. Interaction between Aβ(14-23) monomer and DLPE bilayer. **(a)** The initial placement of the monomer with respect to the bilayer. Aβ (14-23) monomer backbone is colored black while the side-chains, bilayer, and ions are colored according to the atom names in VMD. **(b)** Images depicting the initial interaction of the monomer with the bilayer and the following re-orientation of the monomer. Ions within 10Å of the protein are shown. **(c)** Change in secondary structure of the monomer over time. DSSP was used to calculate the secondary structure; the legend shows what each color in the plot represents.
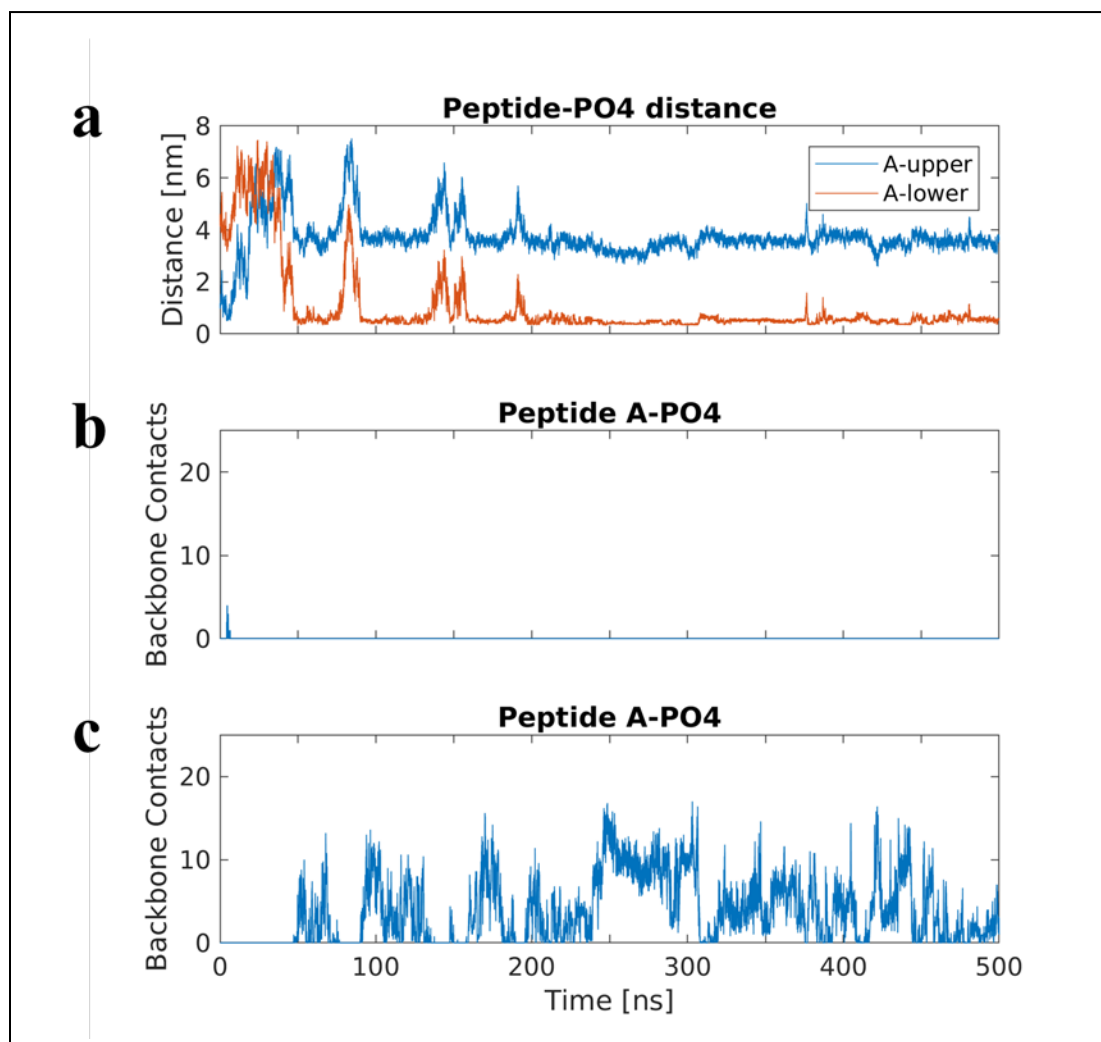
Figure 5.8. Interaction of Aβ(14-23) monomer with DLPE bilayer. **(a)** The distance between Aβ(14-23) monomer and each leaflet of the bilayer, called upper and lower, are plotted versus time. The number of protein backbone contacts with the PO4 head groups of the upper **(b)** and lower **(c)** leaflet are plotted versus time.

structure, was also observed during the interaction with the bilayer, **Figure 5.7C**. Even when bound to the bilayer, the monomer remains highly dynamic, undergoing several conformational changes, as seen in the time-dependent secondary structure, **Figure 5.7C**. Furthermore, the time-dependent peptide-bilayer distance also reveals that the monomer did not remain statically adsorbed to the bilayer, **Figure 5.8A**; further evidenced by the change in number of backbone contacts between the monomer and the bilayer, **Figure 5.8B** and **C**.

Formation of Dimer on DLPE bilayer

Next, we investigated the possibility of dimer formation in the presence of DLPE bilayer. The two monomers were placed on the outer leaflet side of the bilayer, **Figure 5.9A**, inset. The distance between the CoM of the two Aβ(14-23) monomers versus time was monitored, **Figure 5.9A**, and shows that the dimer formation did not happen until ~300ns of the simulation had elapsed. The reason for the "lag" period in the dimer formation is clear from the peptide-bilayer headgroup distance, **Figure 5.9B**, which shows that monomer B traverses the periodic boundary within the first 10ns of the simulation. During this time monomer A binds to the outer leaflet, after ~2ns, in the same manner as the single monomer bound the bilayer, **Figure 5.7**. Likewise, monomer B, once it traversed the periodic boundary, interacts with the inner leaflet and binds the bilayer in a similar fashion. Similar to the interaction of a single monomer with the bilayer, each of the two monomers experience conformational changes during interactions with the bilayer, **Figure 5.9C**. The secondary structure of the monomers primarily transitions between bend and turn structures.
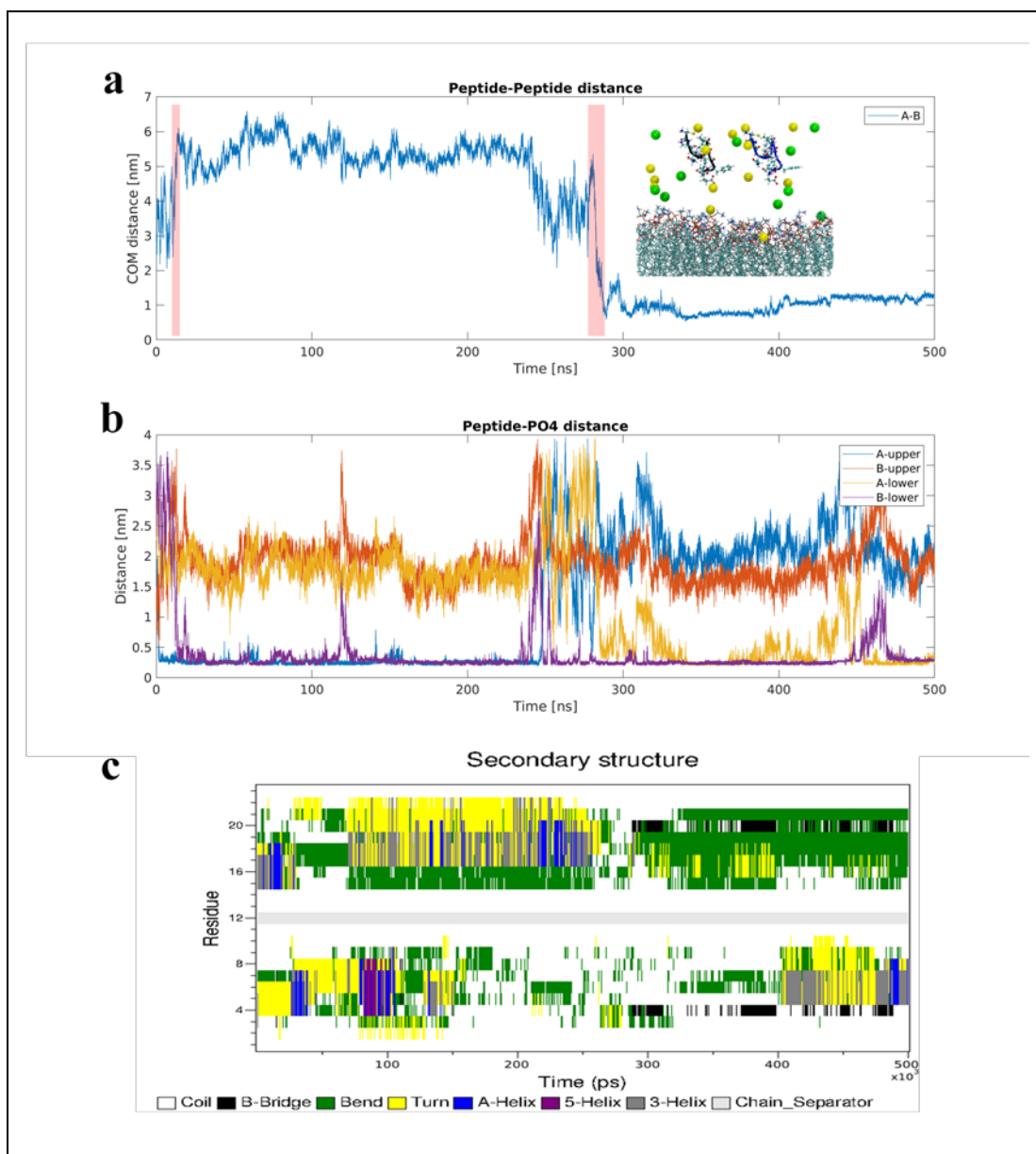
Figure 5.9. Interaction of two Aβ(14-23) monomers with DLPE bilayer. **(a)** Time-dependent CoM distance between the two monomers. The highlights indicate crossing of the periodic boundary; first a monomer moves away from the upper leaflet, next the other monomer leaves the upper leaflet side and is recruited by the membrane bound Aβ(14-23) monomer. Inset show the initial configuration of the system, with monomer A in black and monomer B in blue. Atoms are colored according to VMD. **(b)** Distance of monomers to the two leaflets of the bilayer versus time. **(c)** Change in secondary structure of the monomers over time, monomer A is below the grey separator. DSSP was used to calculate the secondary structure; the legend shows what each color in the plot represents.

Dimer formation occurs when monomer A dissociates from the outer leaflet, traverses the periodic boundary, and starts interacting with monomer B, **Figure 5.10**. The dimers forms through the interaction of N- and C-terminal residues of the two monomers in an anti-parallel conformation, **Figure 5.10A.** Over time, the conformation transitions to a more compact dimer, 300ns, with both monomers interacting with the bilayer, primarily backbone of monomer B and side-chains of monomer A, **Figure 5.10A**. The dimer is very dynamic and undergoes further conformational re-arrangement by extending away from the bilayer surface, 450.6ns, followed by re-organization so that the dimer is anchored to the bilayer through monomer A, 461.4ns on **Figure 5.10B**. Finally, the dimer lies in a flat conformation on the bilayer in an extended conformation with N-terminal residues of monomer A and C-terminal residues of monomer B interacting.

Interaction of Four Aβ(14-23) Monomers with Lipid Bilayer

To investigate the effect of the initial Aβ(14-23) monomer orientation, as well as symmetrical concentration through the bilayer, we performed characterization of the interaction of four monomers with DLPE bilayer. Two monomers were placed on each side of the bilayer, with initial orientation of the monomers on the outside and inside facing leaflets being opposite of each other, **Figure 5.11**. Similar to the results for two monomers interacting with the bilayer, the monomers on each side of the bilayer assemble into dimers, but the process occurs more rapidly. As shown in **Figure 5.11**, on both sides of the bilayer, the monomers interact with the surface within the first 20ns of simulation followed by a rapid dimer formation process. Also similar to before, structural changes occur in monomers upon interaction with the surface, **Figure 5.12**, the primary structural features being bend and turn conformations. Monomer B, initially assumes a helical conformation
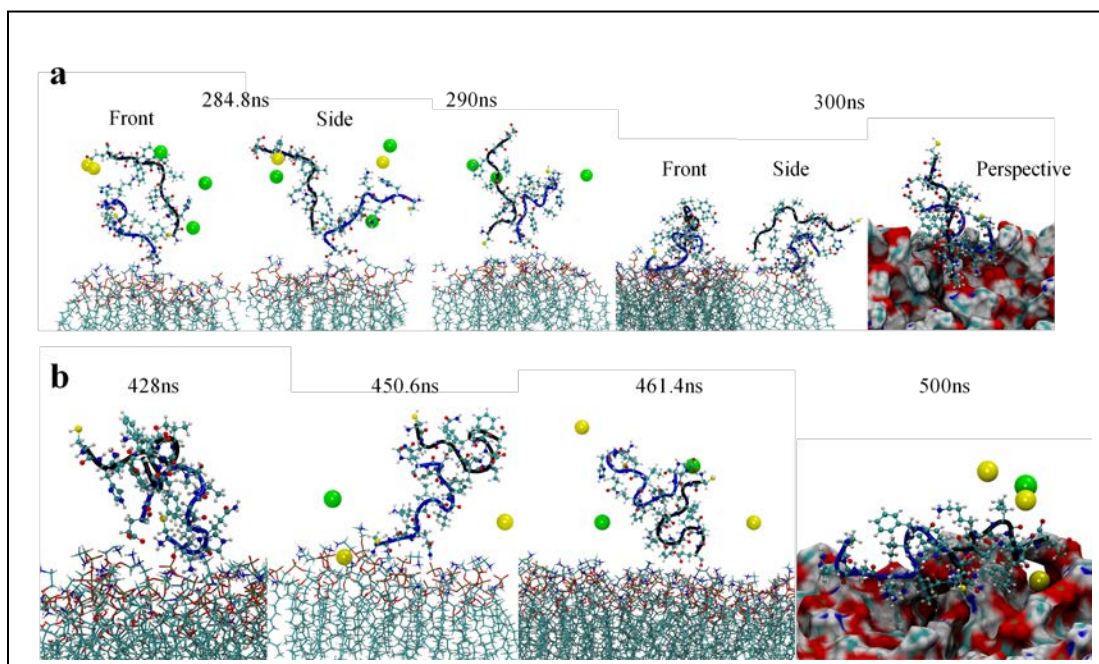
Figure 5.10. Formation of Aβ(14-23) dimer on DLPE bilayer. **(a)** Depiction of the initial interaction between the two monomers, 284.8ns, followed by re-arrangement of the monomers from an extended dimer, 290ns, to a compact and flat dimer, 300ns. Monomer A in black and monomer B in blue. Atoms are colored according to VMD. **(b)** Monomer A dissociates from the bilayer surface, 428ns, is extended and undergoes re-arrangement, 450.6ns, followed by re-attachment to the surface, 461.4ns; and finally forms an extended conformation on the surface, 500ns; throughout this process the dimer remains stable.
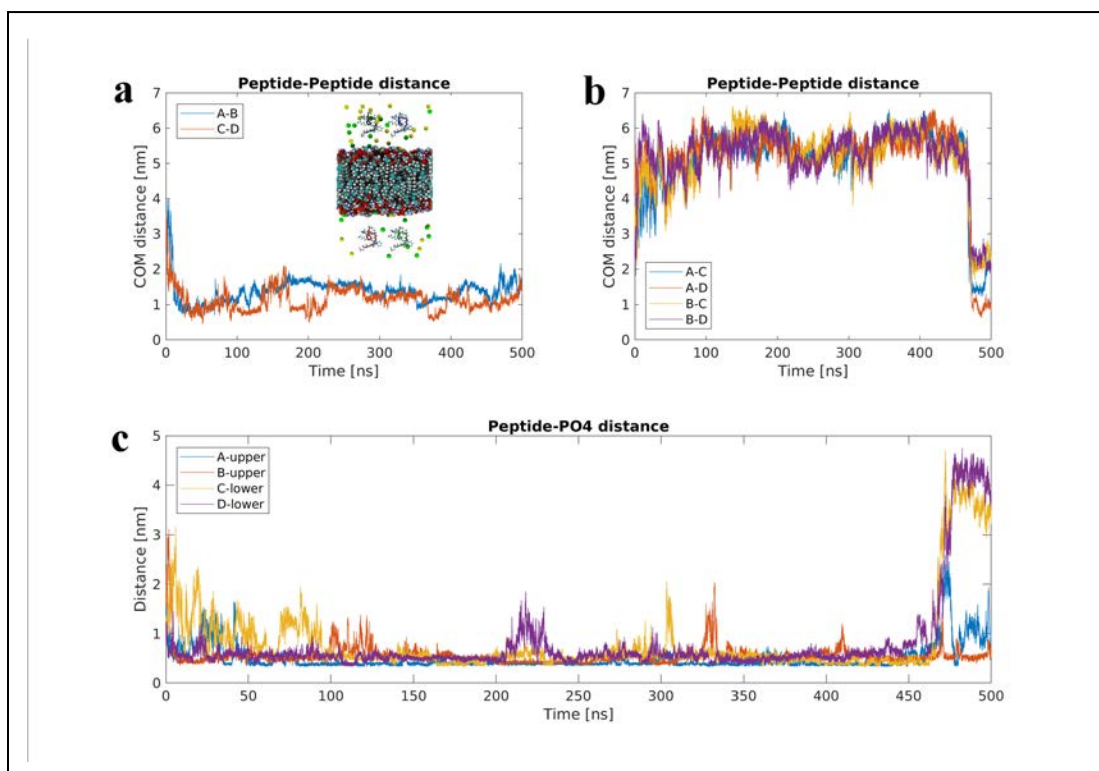
Figure 5.11. Interaction of four Aβ(14-23) monomers with a DLPE bilayer. **(a)** The CoM distance between two pairs of monomer over time. The inset shows the initial placement of the monomers with respect to the bilayer. Monomer A is in black and monomer B in blue, monomer C in red, monomer D in green, and the side-chains and bilayer are colored according to the atom names in VMD. Monomers A and B are on the upper leaflet side of the bilayer. **(b)** CoM distance of each monomer to the other three monomers. **(c)** Shows the minimum distance of the peptide backbone and the PO4 of the lipid headgroups, as determined by *g_mindist*.
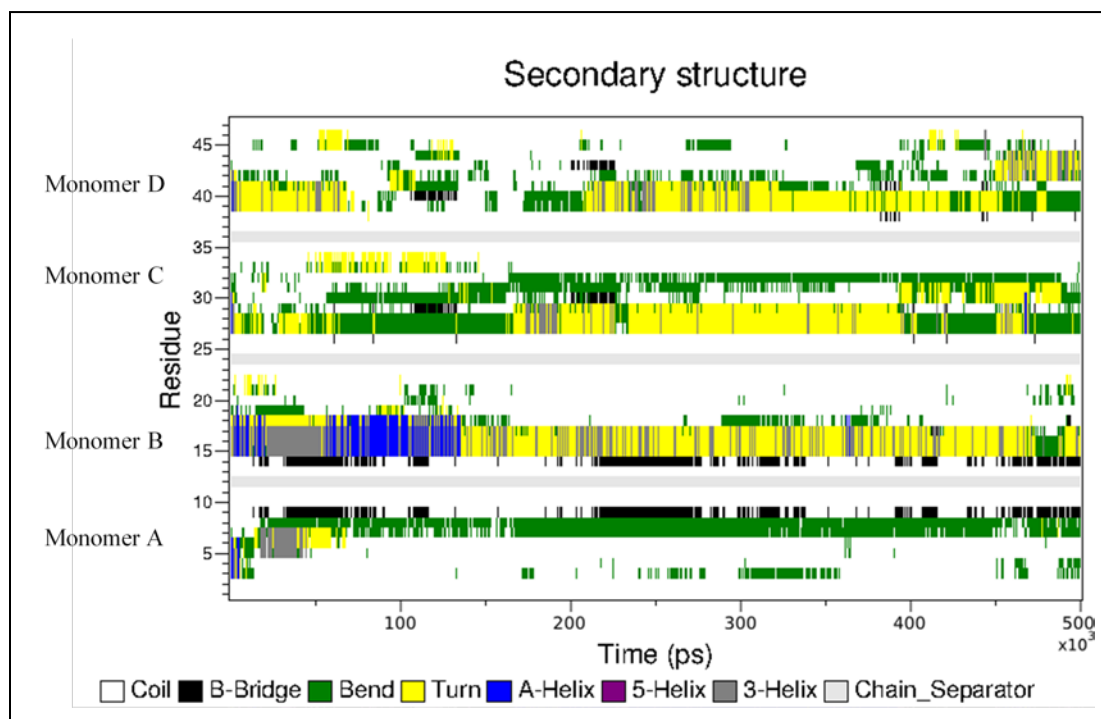
Figure 5.12. Interaction of four Aβ(14-23) monomers with a DLPE bilayer. Secondary structure of each monomers during the simulation is shown as a function of time, as determined by DSSP.

but is rapidly converted into a largely unstructured conformation with some turn and bend structure.

The individual monomers within the dimer interact with and re-organize on the surface throughout the simulation. The re-organization allows the monomers to dissociate from and re-associate with the surface – but remain as dimers, **Figure 5.11C**. This dynamic behavior is seen clearly in the fluctuations of the number and duration of contacts during the simulation, **Figure 5.13**. Furthermore, it becomes clear that, for both dimers, a single monomer is responsible for the majority of contacts and acts as an anchor for the dimer.

Interestingly, toward the end of the 500ns simulation the dimer formed on the inner leaflet of the bilayer traverses through the periodic boundary and interacts with the dimer present on the outer leaflet. Initially an extended tetramer is formed with one monomer from each dimer interacting, **Figure 5.14**. The tetramer then undergoes structural transition that extends the contact interface so that all monomers interact with each other, while only the original dimer is interacting with the membrane surface, 477.8ns on **Figure 5.14**. Further re-structuring of the tetramer happens and causes an extended tetramer with a trimeric core to form as the final configuration during the simulation. The trimer core is extended from the membrane surface, with only one monomer interacting with the surface, and participates in side-chain interactions with the remaining membrane-bound monomer, 500ns on **Figure 5.14**.

Effect of Aβ(14-23) of DLPE Bilayer
An important effect associated with amyloid peptides and proteins are their tendency to disrupt normal bilayer function. To investigate the effect of the Aβ(14-23) monomers on the DLPE bilayers we performed analysis of the bilayer thickness as well as area per lipid.

Chapter 5: Interaction with surfaces promotes aggregation of amyloid proteins
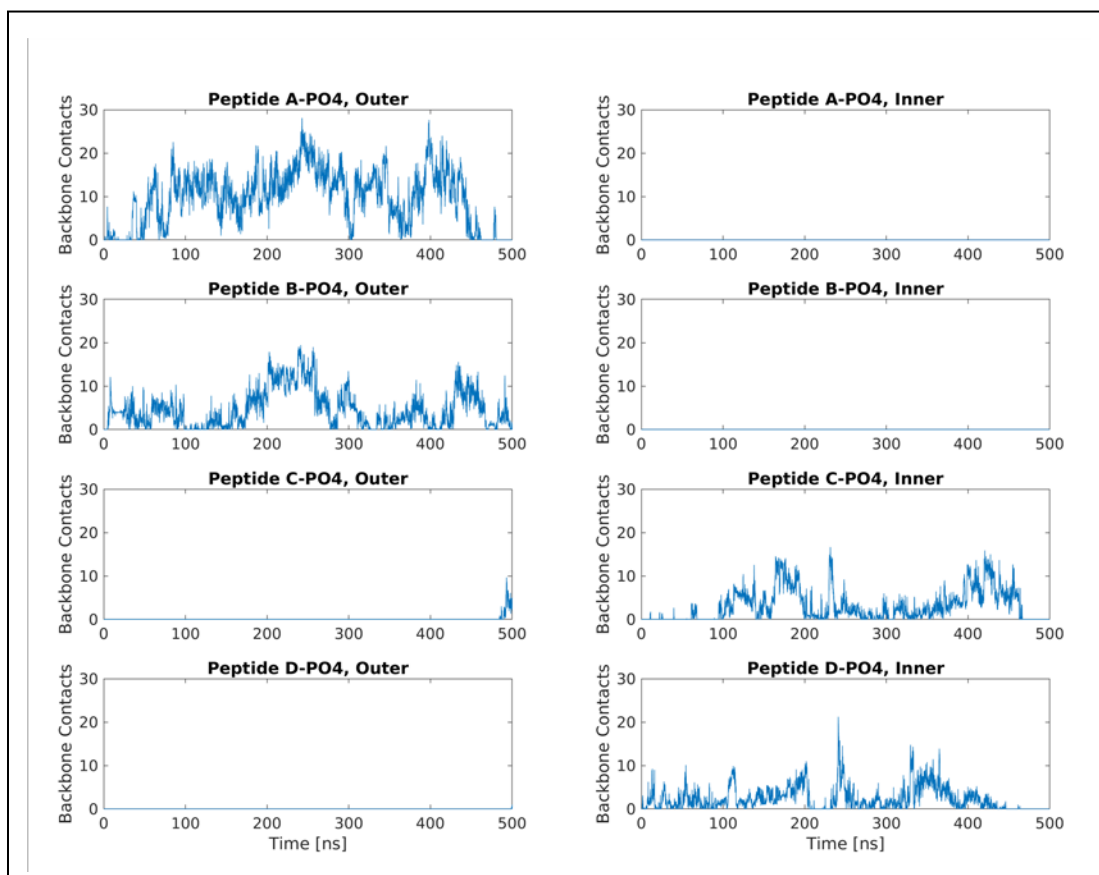
Figure 5.13. The frequency of interaction of four Aβ(14-23) monomers with DLPE bilayer. The number of backbone contacts between each monomer and the bilayer PO4 headgroups are plotted for each leaflet of the bilayer.
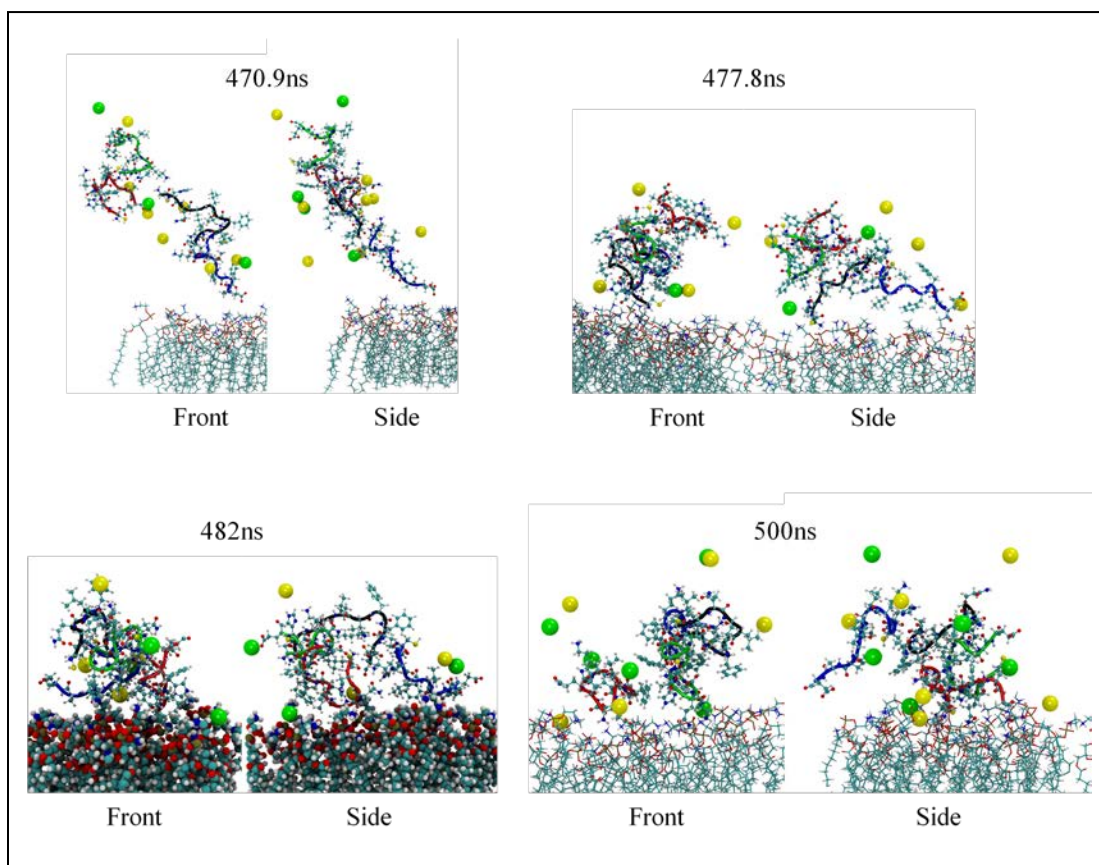
Figure 5.14. Formation of tetramer on DLPE bilayer surface. Dimer, formed by monomers C and D, traverses the periodic boundary and interacts with surface-bound dimer formed by monomers A and B, 470.9ns. Monomer A is in black and monomer B in blue, monomer C in red, monomer D in green, and the side-chains and bilayer are colored according to the atom names in VMD. Following the interaction, the surface-bound dimer undergoes conformational change that brings the tetramer closer to the surface, 477.8ns. Over the next ~20ns the tetramer experiences conformational changes that increase the interaction with the surface, but ultimately leads to the formation of a compact trimer, monomers A-C, and a surface bound monomer that interacts with the trimer, 500ns.

For the single and two monomer systems, the majority of the simulation time was spent with a single monomer interacting with one leaflet of the bilayer. Area per lipid calculations show that the leaflet which was interacting with the Aβ(14-23) monomer experienced compression of the lipids, **Figure 5.15A** and **B**. For both systems the interaction with peptide causes change to the APL in the order of a few $Å^2$, moreover, the presence of two monomers does not cause higher compression of the lipids. However, once a dimer has formed on the bilayer the lipids become more compressed, with APL changes up to $10Å^2$, ~325ns on **Figure 5.15B**. Four Aβ(14-23) monomers interacting with the membrane cause effects that follow the trends of the previous two systems, larger change in APL when larger number of Aβ(14-23) monomers interact with the membrane, **Figure 5.15C**.

Other changes in membranes were characterized by measuring the mean membrane thickness, **Figure 5.16**. It is clear from the bilayer thickness plots that increase in Aβ(14-23) monomer concentration causes an increased inhomogeneity in the membrane thickness, with four monomers causing the largest change. Interestingly, the interactions do not cause membrane thinning, rather the monomer causes the membrane to become slightly expanded, **Figure 5.16A**, this effect sees a significant increase when two monomers interact with the membrane, **Figure 5.16B**, and is at maximum when four monomers interact with the membrane, **Figure 5.16C**.

5.4 Discussion

Time-lapse AFM imaging of the aggregation of amyloid proteins allowed us to directly visualize the effect of a surface during the aggregation process. Surface greatly enhanced
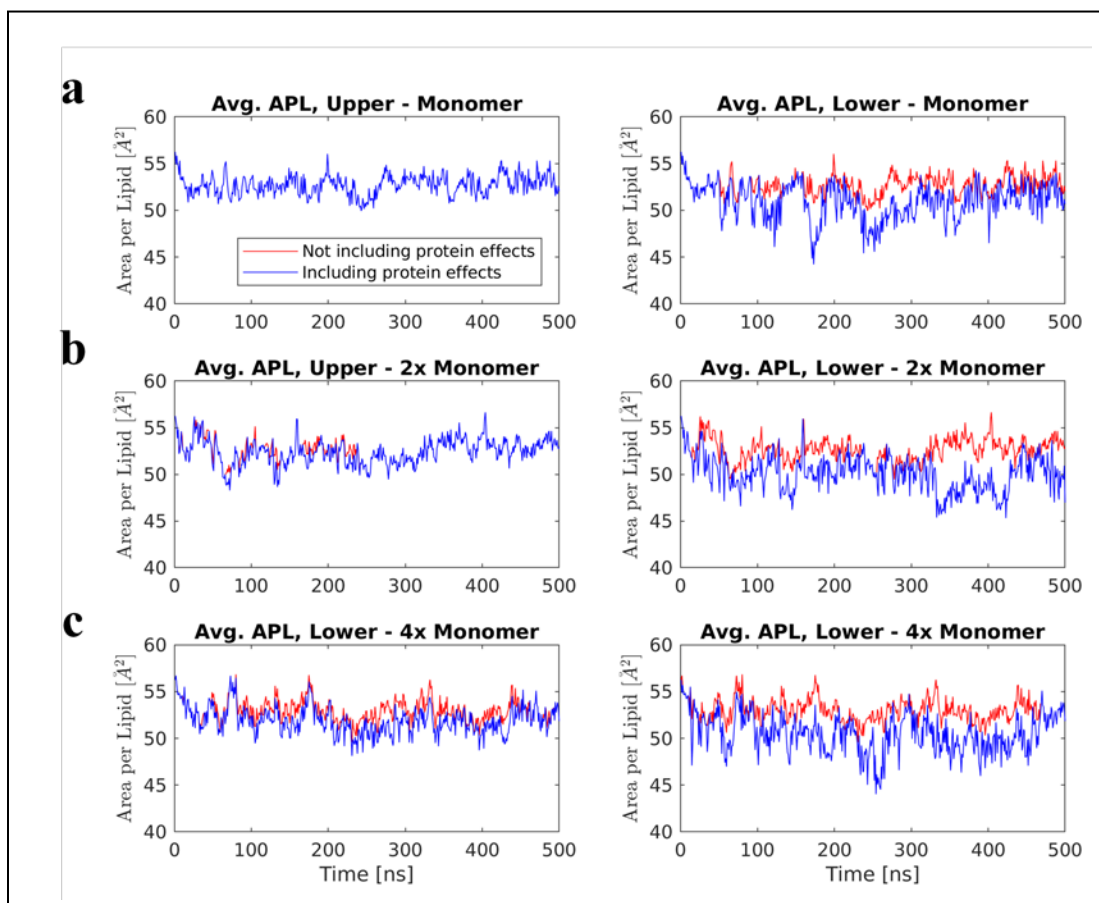
Figure 5.15. The effect of interaction of Aβ(14-23) monomer on DLPE bilayer. Are per lipid for DLPE interacting with a monomer, **(a)**, two monomers, **(b)**, and four monomers, **(c)**, are plotted versus time. GridMAT-MD was used to determine the APL, taking into account interactions of the Aβ(14-23) monomers with the bilayer, **blue** curves, or disregarding protein-lipid interactions, **red** curves.
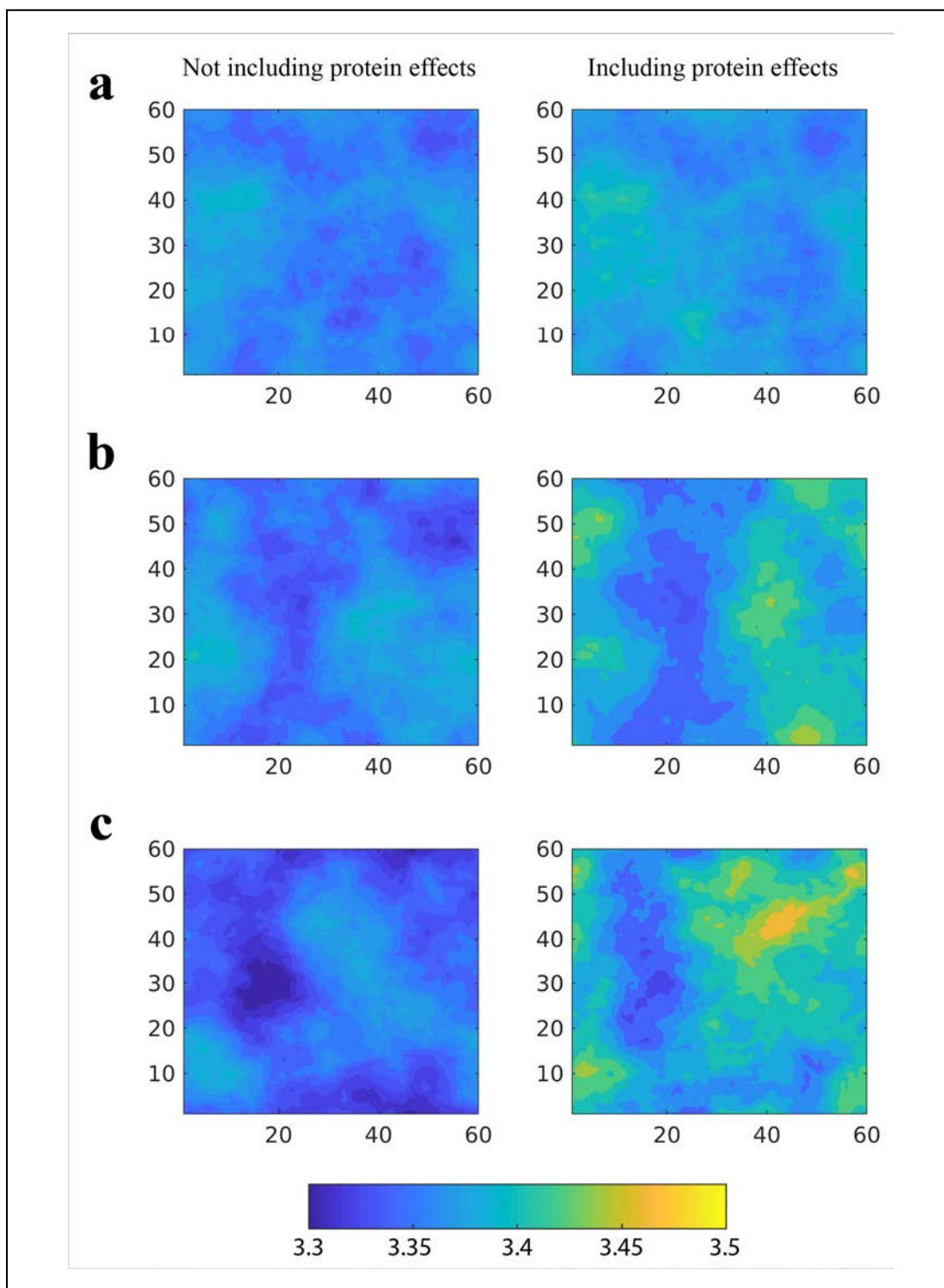
Figure 5.16. The effect of interaction of Aβ(14-23) monomer on DLPE bilayer thickness. Average thickness of the DLPE bilayer interacting with a monomer, **(a)**, two monomers, **(b)**, and four monomers, **(c)**, were obtained from the 500ns simulation. GridMAT-MD was used to determine the thickness, taking into account, **right**, or disregarding, **left**, interactions of the Aβ(14-23) monomers with the bilayer. Colorbar is in units of nm.

Chapter 5: Interaction with surfaces promotes aggregation of amyloid proteins

the aggregation of Aβ(14-23) peptide, full-length Aβ42, and α-syn protein, compared to bulk experiments that showed very few aggregates at the same concentrations.

The mechanism of the unique on-surface pathway of aggregation was characterized using MD simulations. Interactions of Aβ(14-23) with mica and DLPE bilayer surfaces, revealed that interactions of a monomer with the surface is accompanied by the structural transition of the monomer that promote interactions with another monomer. A free monomer is able to bind to the adsorbed monomer and rapidly form a dimer. The newly formed dimer is very dynamic and the monomers within the dimer undergo structural transitions. Compared to our previous simulations for dimer formation by free Aβ(14-23) monomers, in which no major structural changes were observed during the first ~200ns (100), we have an almost five-fold faster structural transition when the peptides interact on the surface.

With regard to implications of this work to AD development, we propose, in the framework of the amyloid cascade hypothesis, that the interaction of amyloidogenic polypeptides with cellular membranes plays an important role for the disease-related aggregation process. Under normal conditions, the interaction of intracellular or extracellular amyloid proteins with intracellular or extracellular membranes is weak, so small aggregates assemble. These are unstable and dissociate into monomers either on the surface or after dissociation from the membrane. A change in membrane properties, leading to an increase in affinity of amyloid proteins to the membrane surface, will shift the process to the formation of more stable oligomers that remain intact after dissociation from the surface, and this assembly triggers the disease-related aggregation process. This mechanism does not require elevation of the amyloid peptide concentration, and indeed the

Chapter 5: Interaction with surfaces promotes aggregation of amyloid proteins

concentration of amyloid beta peptide in blood fluctuates weakly regardless of the disease state and does not differ from the controls (200). Also, the Aβ clearance in late-onset AD patients drops by about one quarter (201), and only a fraction of the Aβ produced is trapped in amyloid plaques (202).

Our model is in line with recent findings that demonstrate that the aggregation rate of amyloidogenic proteins measured in the presence of membranes of various types depends on the membrane composition and mechanical properties (203-206). Indirect support for the concept of membrane-induced aggregation comes from findings on the elevated yield of Aβ dimers in membrane-containing fractions of blood from AD patients compared with controls (207). Note as well our direct observation of α-syn on-surface assembly at nanomolar concentrations when the initial monomer was covalently bound to the surface (101). Recent NMR studies on the intracellular structure of α-syn showed that it primarily exists in cells as monomers in an essentially unstructured, compact conformation, but transient interaction of the protein with the membrane was considered (187).

5.5 Conclusions

We demonstrated that the interaction of amyloid proteins with surfaces allow the proteins to assemble into aggregates at concentrations that are non-permissive for aggregation in solution. Moreover, we characterized the mechanism of the on-surface aggregation using MD simulations. The interaction with surfaces cause amyloid proteins to rapidly undergo conformational transitions to unstructured monomers that favor interactions with free monomers. Furthermore, we found that aggregates formed on the surface are dynamic and can dissociate from and re-associate with the surface. As a result, these dissociated

aggregates can play roles as seeds for aggregation in the bulk solution, or start a neurotoxic effect such as phosphorylation of the tau protein to initiate its misfolding and aggregation followed by neurodegeneration (186). Therefore, we posit that on-surface aggregation is the mechanism by which neurotoxic amyloid aggregates are produced under physiological conditions. Our proposed model does not require an elevation in amyloid synthesis, as, based on simulation results, stable oligomers can rapidly form at low concentrations in presence of surfaces.

Chapter 6.   INTERACTION OF α-SYNUCLEIN WITH LIPID BILAYERS

6.1 Introduction

In the previous chapter on-surface aggregation presented a unique pathway to allow the amyloid proteins to assemble into aggregates at physiological concentrations. The relevance of this pathway is immediately clear in the case of PD, where the monomeric α-syn interacts with membranes as part of its normal function through binding to phospholipid molecules (208, 209), a property that is neglected in current models involving the assembly of toxic aggregates in bulk solution. Past reports suggest that the normal membrane-binding function of α-syn is related to regulation of synaptic vesicle trafficking (208-210). Moreover, the protein has been shown to undergo accelerated aggregation when incubated in the presence of phospholipid vesicles at high protein:lipid ratios (211-213). These findings suggest that self-assembly at the surface of cellular membranes is the mechanism by which potentially neurotoxic oligomers are assembled at physiological concentration of the protein (191).

In the current study, this hypothesis is tested by direct visualization of α-syn aggregation on the surface of supported lipid bilayers (SLBs) using time-lapse AFM. We demonstrate that SLBs promote the aggregation of α-syn at concentrations as low as 10 nM, which corresponds to the concentration range in the CSF (214). Moreover, aggregates are not strongly bound to the surface and are capable of spontaneous dissociation into solution. MD simulations revealed that the interaction mechanism with SLBs is different depending on membrane composition. α-Syn monomers change conformation upon interaction with the bilayers in a composition dependent manner. Furthermore, aggregation

propensity also depends on SLB composition, being considerably higher for 1-palmitoyl-2-oleoyl-sn-glycero-3-phospho-L-serine (POPS) bilayer when compared to 1-palmitoyl-2-oleoyl-sn-glycero-3-phosphocholine (POPC) due to the conformations of α-syn after binding to the membrane; a property in line with experimental data. Importantly, simulations revealed that the interaction and self-assembly of α-syn does not damage the membranes. We propose a model for the membrane mediated amyloid aggregate assembly and the role of this process in beginning of the disease state.

6.2 Materials & Methods

6.2.1 Aggregation of Supported Lipid Bilayers

SLBs, on freshly cleaved mica, were prepared from POPC and POPS following the protocol in ref. (215). *In situ* AFM imaging was then performed to characterize the SLB surface, following which α-syn (A140C mutant) solution was added to the membrane surface and images were then acquired at different time points. Between images, the AFM tip was placed on idle (electronically retracted, approximately 4μm above the scan area) to ensure that it exerted minimum influence on the sample.

6.2.2 Molecular Dynamics Simulations

Lipid bilayers of POPC and POPS were prepared using the *insane.py* script (available at http://md.chem.rug.nl) using the MARTINI2.2refP (216) force field together with the polarizable water (217) model. The initial bilayer was constructed using, in total, 512 lipids placed randomly in a bilayer structure with 40 water molecules per lipid and 150mM NaCl. After energy minimization using the steepest decent algorithm, the bilayers were simulated as an NPT ensemble for 500ns using a 20fs integration time step. The simulation employed

periodic boundary conditions with a semi-isotropic pressure coupling using the Parrinello-Rahman barostat at 1bar with a 12ps coupling constant. The temperature was kept at 300K using the velocity rescaling algorithm. Electrostatic interactions were calculated using the particle mesh Ewald algorithm, with a real space cut-off of 1.1nm. All simulations were performed using the 2016 version of the GROMACS suite of programs (218). Only the final frame of each bilayer simulation was used for further simulations.

Interaction of α-syn with Lipid Bilayers

Micelle-bound α-syn (PDB ID: 1XQ8) was used as the initial protein structure. A coarse-grained structure was generated using the *martinize.py* script and the PDB structure. The coarse-grained α-syn structure was then placed at a CoM distance of 6nm from the bilayer core in a parallel orientation (along the long protein axis) to the bilayer. The system was then solvated in a box of 13x13x18 nm^3 water and 150mM NaCl. The simulation procedure was the same as previously described for bilayers alone, with the exception that the simulation duration was 4μs for each protein-bilayer system.

Interaction of Free α-syn with Membrane-bound α-syn

Simulations with membrane-bound and additional free α-syn were conducted using the last frame of the previous 4 μs simulation and adding another α-syn at a CoM distance of 6nm from the membrane-bound α-syn. Orientation of the free α-syn was parallel to the bilayer using the same protein conformation as the initial α-syn-bilayer simulation. Simulations for both POPC and POPS were carried out for 2μs each using the previously described parameters.

6.2.3 Analysis of Bilayer

The area per lipid (APL) for each of the simulated systems was calculated using Dirichlet tessellation to obtain Voronoi diagrams. The GridMAT-MD approach was used to perform the tessellation every ns, using the PO4 groups of each bilayer as the reference, and with a resolution (grid spacing) of 1Å (196). In addition, membrane thickness was also calculated based on the same reference group.

6.3 Results

6.3.1 Experimental AFM studies of α-syn Aggregation on Lipid Bilayers

Lipid bilayers were prepared on freshly cleaved mica, allowing for direct visualization, with AFM, of interactions between the protein and bilayer over many hours. Based on their prevalence in neuronal cellular membranes, two types of bilayers were used (**Figure 6.1A**): POPC and POPS. POPS shares hydrocarbon chains with POPC but has a serine head group that at physiological pH, renders the surface negatively charged, unlike POPC which has a net neutral charge.

Aggregation of 10nM α-syn on supported bilayers was investigated over a period of 5 hours and the data is shown in **Figure 6.1**. Aggregates on POPC and POPS surfaces at the end of the experiments are shown in **Figure 6.1C** and **D**, respectively. The number of aggregates and the aggregate sizes (volumes) were quantified and are plotted in **Figure 6.1E** and **F**, respectively. The data show that both parameters gradually increase over time, with aggregation on POPS being faster and more pronounced. Aggregates formed on the SLBs are very dynamic and are able to appear, grow, and dissociate from the membrane surface, **Figure 6.2**. Importantly, the surface remains undamaged. Thus, aggregates assembled on the surface can dissociate back into solution, suggesting that aggregates
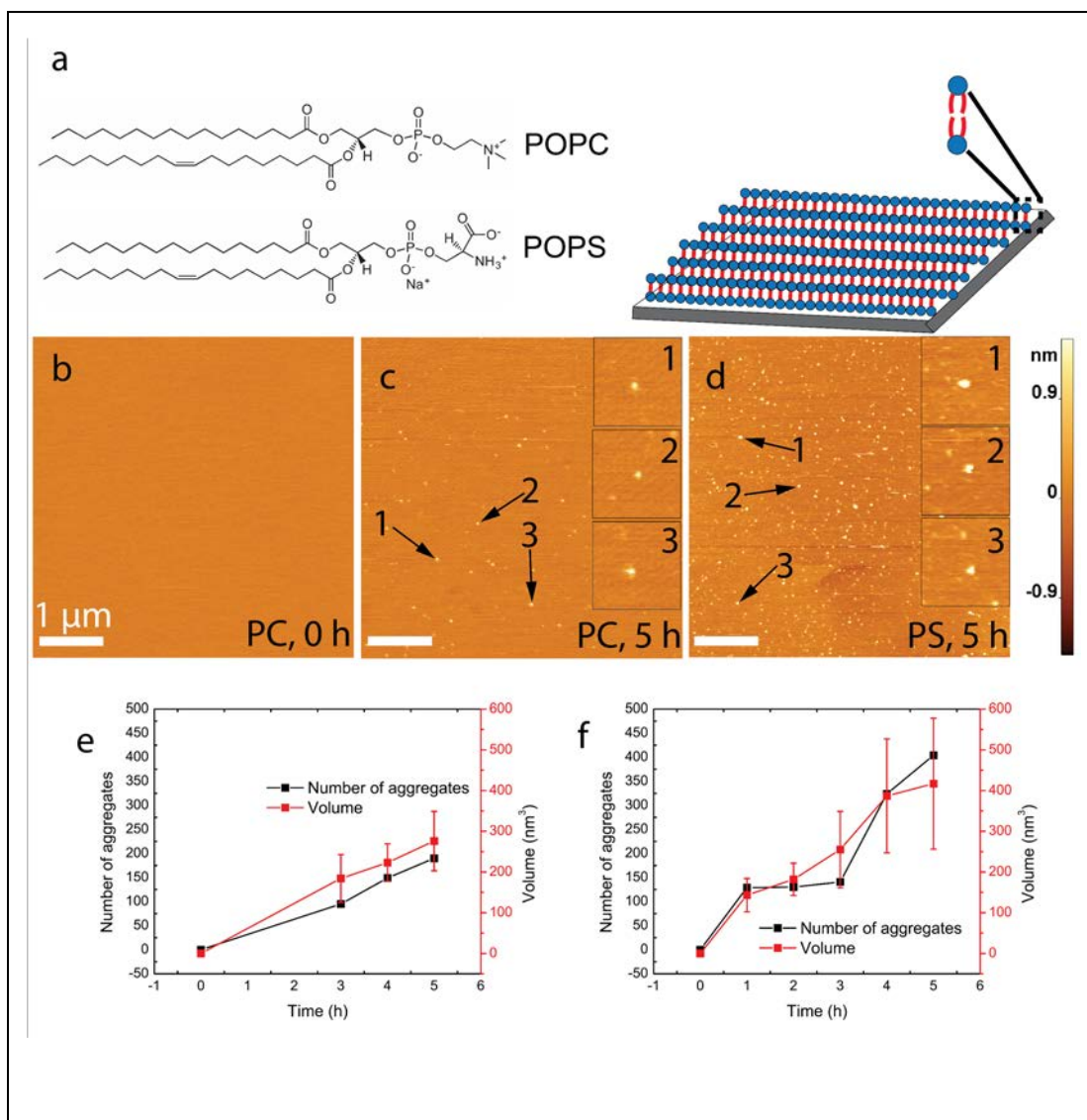
Figure 6.1. Time-lapse AFM images to characterize α-syn aggregation on supported POPC lipid bilayer. **(a)** Chemical structures for POPC and POPS are shown (left). Schematic of a supported lipid bilayer on freshly cleaved mica (right). **(b)** Image of the POPC SLB surface immediately after buffer exchange with 10nM α-syn solution. Images of α-syn aggregates after 5hrs incubation on POPC **(c)** and POPS **(d)** SLBs. Insets show zoomed images of three representative aggregates. The Z-scale is shown to the right of panel **(d)**. **(e)** and **(f)** show the evolution of aggregate quantity and mean volume on POPC and POPS, respectively. The data are shown as the mean ± STD.
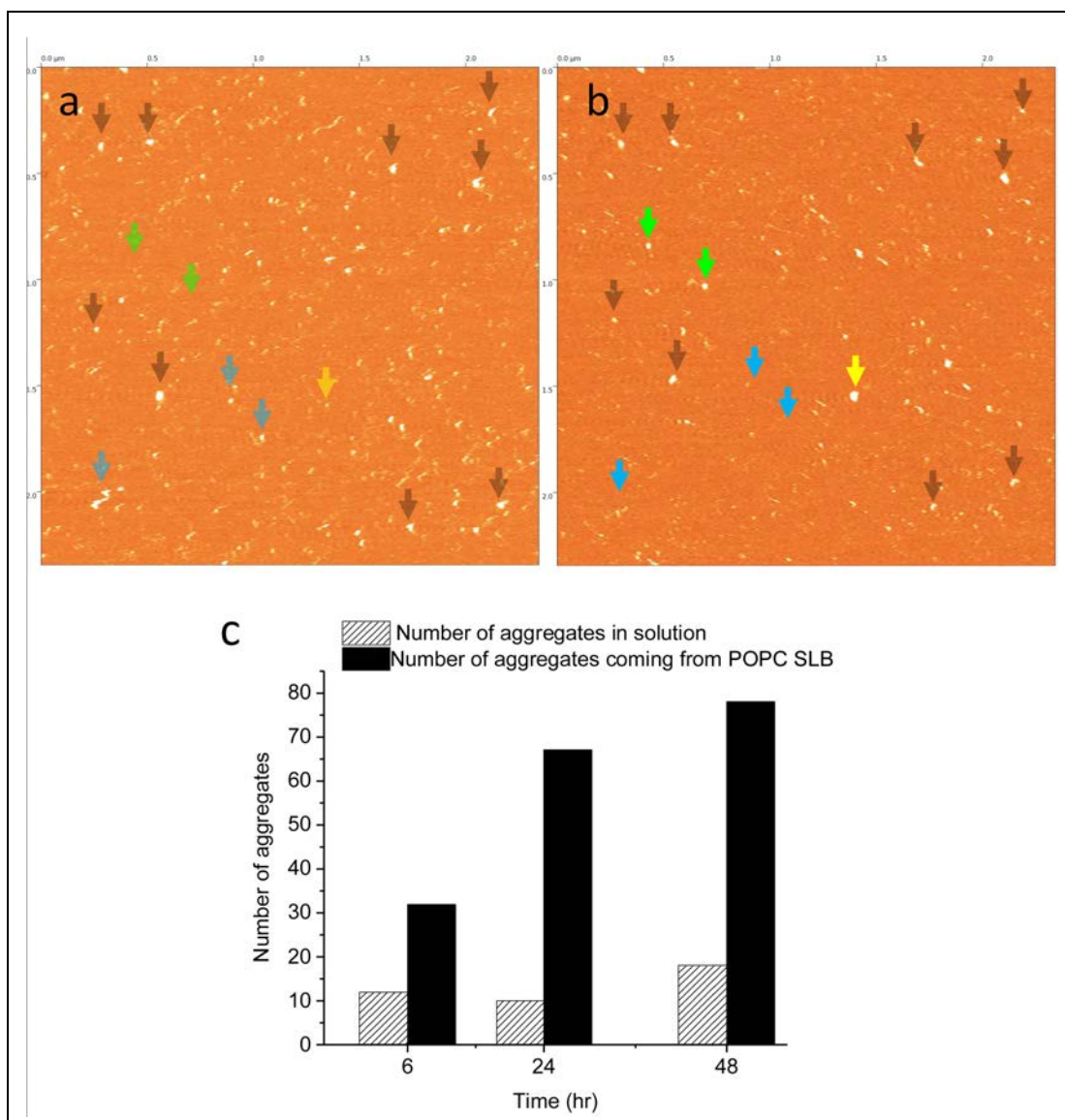
Figure 6.2. Dynamics of α-syn aggregates on SLBs. α-Syn aggregates after 6hrs **(a)** and 6.5hrs **(b)** on POPS SLB. Features that did not change between frames are marked with black arrows. Blue arrows correspond to aggregates that have dissociated in panel **(b)**, while new aggregates that appeared are highlighted with green arrow. A growing aggregate is highlighted in yellow. **(c)** A 10nM α-syn solution was incubated in the presence of a POPC SLB. 5μl of the solution was removed at different time-points (6 h, 24 h, 48 h) and analyzed by AFM. Solid black bars show the number of aggregates, which appeared in the bulk from the POPC SLB, at different times. In a parallel experiment, a 10nM α-syn solution was incubated in a test tube, and an aliquot of 5μl was taken out at the same time-points and analyzed by AFM to check aggregation in the absence of a POPC SLB (striped bars). Aggregates were counted in 2μm × 2μm AFM images.

should appear in the bulk solution above the bilayer. This assumption was tested by direct measurement of the time-dependent accumulation of α-syn aggregates in solution above the bilayer surface, **Figure 6.2C**. The data show that the presence of a bilayer produces significantly more aggregates (solid black bars) compared to the control (dashed bars) supporting the conclusion about dissociating aggregates assembled on the lipid bilayer. Note that similar effect were observed in our recent paper (191), in which the assembly of α-syn aggregates on mica surface was studied.

6.3.2 Computational Modeling of Interaction of α-syn with Lipid Bilayers

Interaction of α-syn Monomer and Lipid Bilayers

To obtain insight into the underlying molecular mechanism of α-syn aggregation on the bilayer surface, we conducted molecular dynamics simulations of interactions of α-syn with the POPC and POPS bilayers. Briefly, a monomer of α-syn was placed 6nm above the center of a 13nm x13nm bilayer patch (512 lipids), and interactions with the bilayer were then simulated. A few selected snapshots illustrating the dynamics of the interaction of α-syn with the POPC bilayer are shown in **Figure 6.3**. According to **Figure 6.3**, α-syn initially binds to the POPC membrane through its N-terminal segment (1420ns). Over time, the length of the segment of the protein in contact with the POPC surface increases, so that the NAC (non-amyloid component, residues 61-95) segment approaches the surface as well (1444-1500ns). Graphically this change in binding is illustrated by the kymograph shown in **Figure 6.4**. In fact, α-syn undergoes multiple association-dissociation events, as evidenced by the fluctuations of the number of contacts over time (**Figure 6.5A**).
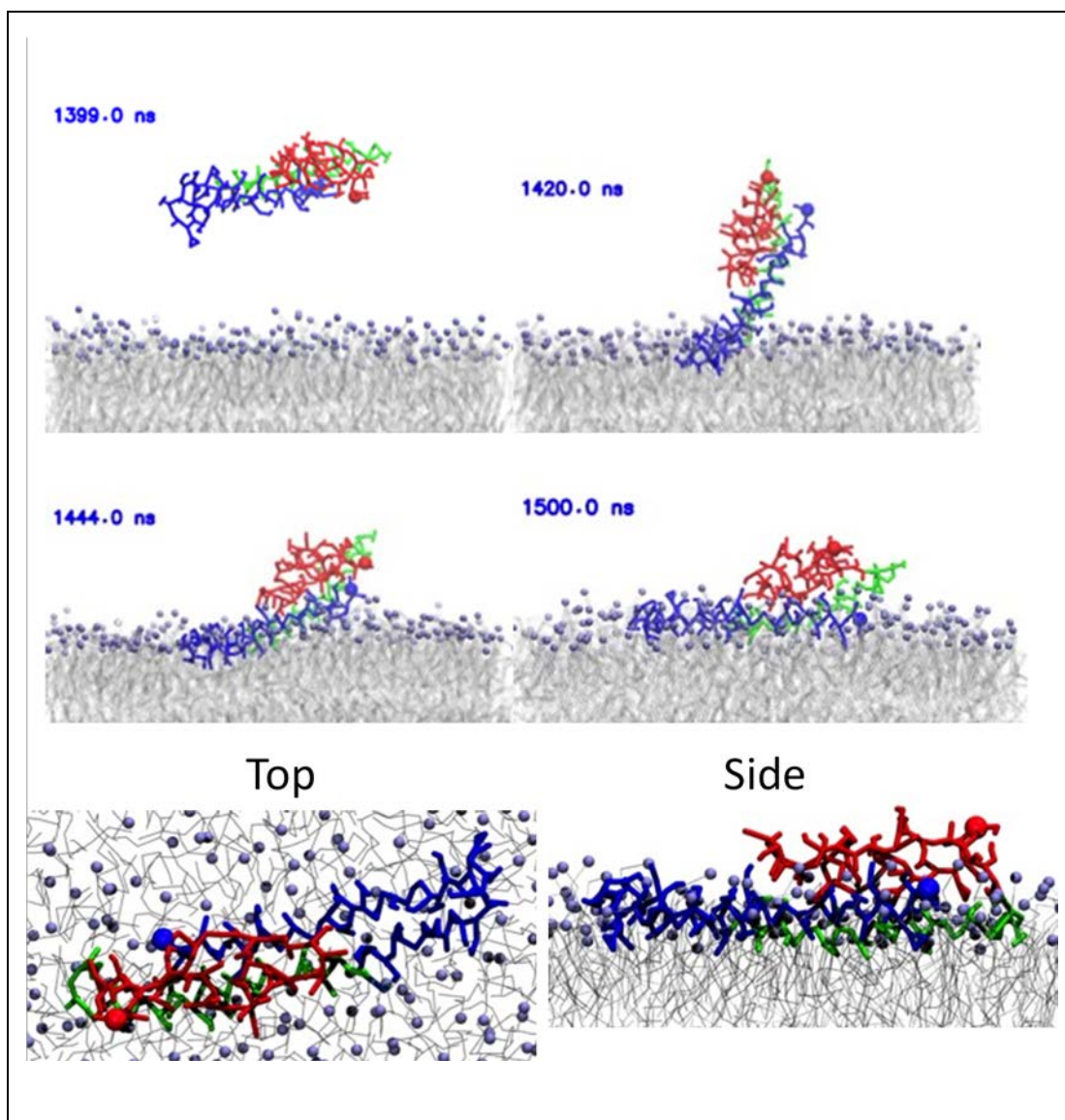
Figure 6.3. Molecular dynamics simulations of α-syn monomer interacting with POPC bilayer. The top four panels show the time resolved stable binding event. Initial interactions happen through the N-terminal, Lys rich, 36-56 segment, following which insertion into the lipid head regions is observed. The bottom two panel, show top and side view snapshots of the last frame, at 4μs, of the MD simulation. The α-syn N-terminal segment is colored blue, the NAC region is in green, and the C-terminal segment is in red. N- and C-terminal residues are highlighted with a sphere. Lipid tails are in grey while the POPC headgroups are in purple.
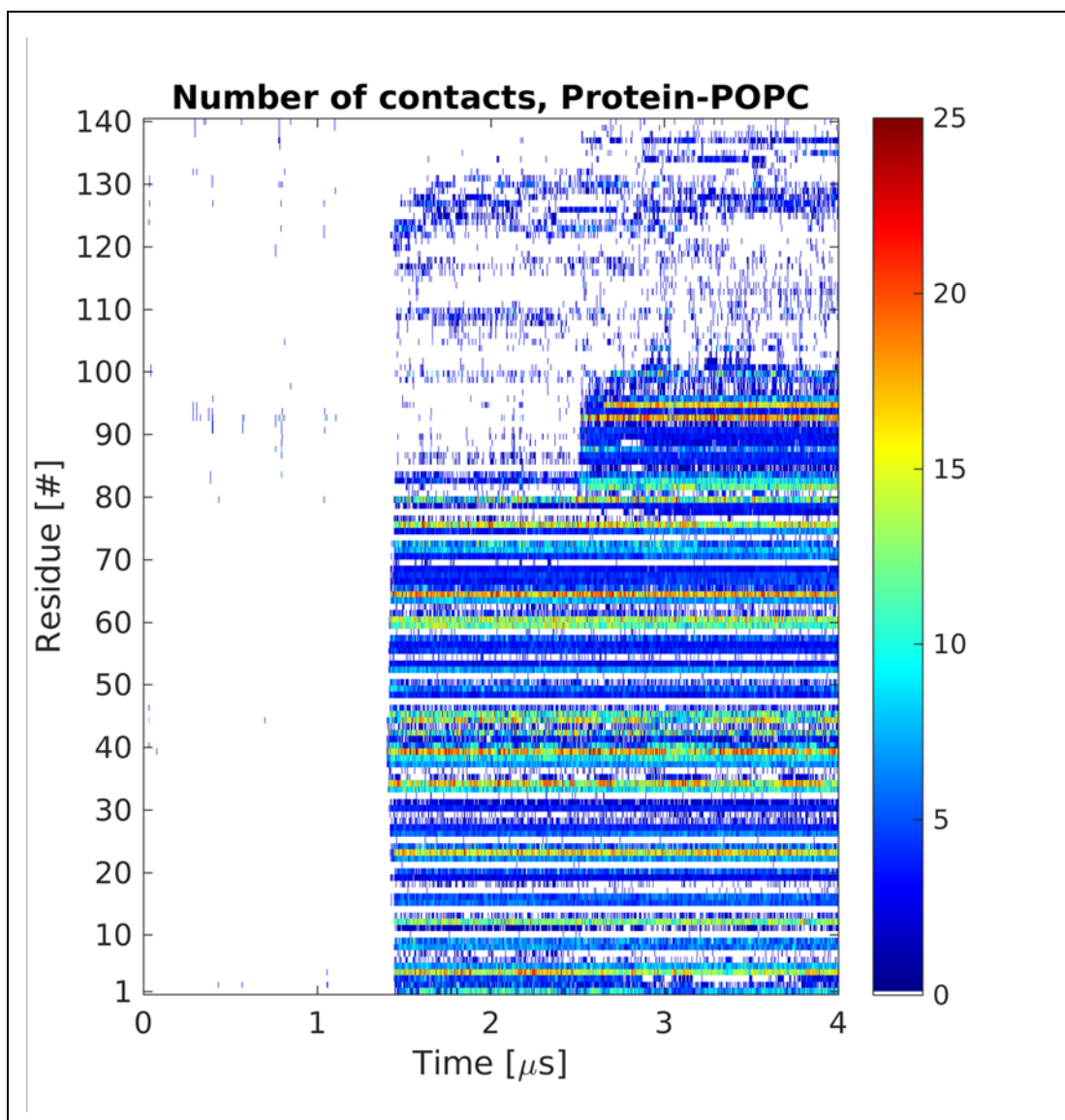
Figure 6.4. Kymograph based om molecular dynamics simulation of α-syn interaction with POPC bilayer, showing the time dependent residue-wise interaction with the bilayer. The colorbar represents number of contacts that each residue of the protein makes with the bilayer.
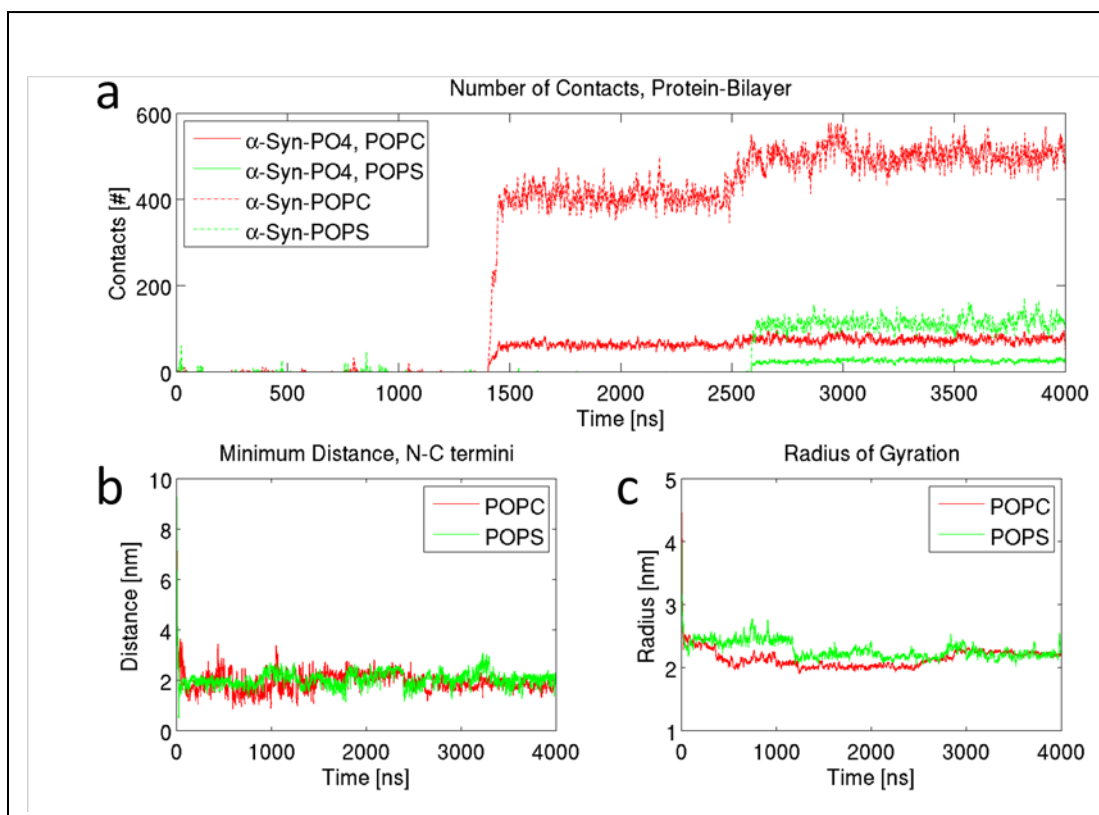
Figure 6.5. Molecular dynamics simulation of α-syn interaction with lipid bilayers. **(a)** Graphical representation of α-syn total contacts (distance <0.6 nm, dashed lines) and contacts with PO4 groups (solid lines) of the membranes. **(b)** Minimum distance between the N- and C-termini of α-syn vs time. **(c)** Time-dependent change in radius of gyration of α-syn.

Eventually (after ~1.5 µs, seen as a jump in the graph and increased contact in the kymograph), the protein strongly interacts with the bilayer, is inserted in the interfacial region, and stays bound to the bilayer for the remainder of the simulation. Throughout the simulation the end-to-end distance and the radius of gyration of the α-syn molecule experience minor fluctuations (**Figure 6.5B** and **C**).

A similar analysis was performed for α-syn monomer interacting with a POPS bilayer. A few selected frames are shown in **Figure 6.6**. Similar to the data obtained for the POPC bilayer, the N-terminal segment of α-syn binds to the membrane surface, but unlike POPC, the interaction with POPS is limited to a short central region (G36-K58) of the protein, graphically illustrated by **Figure 6.7**. As a result, once stably interacting with the surface, the protein remains extended out of the plane of the POPS surface throughout the simulation. This is dramatically different compared to the interaction with POPC bilayer, as can be seen by the number of interactions with the bilayer, **Figure 6.5A**. However, the overall geometry of the conformation of the α-syn monomer is not significantly different on the two bilayer surfaces, as measured by N-C distance and the radius of gyration, **Figure 6.5B** and **C**.

We then analyzed if interaction of α-syn monomer with the bilayers caused any change in the bilayer itself by measuring the area per lipid as well as the thickness of the bilayer during the simulations, **Figure 6.8** through **Figure 6.10**. Prior to the interaction with α-syn monomer the POPC bilayer has an APL of ~65.5Å^2, however this changed once the monomer is interacting with the bilayer, **Figure 6.8 top left**. For the leaflet that is interacting with the monomer, the APL experiences a compression of up to ~8Å^2 while for
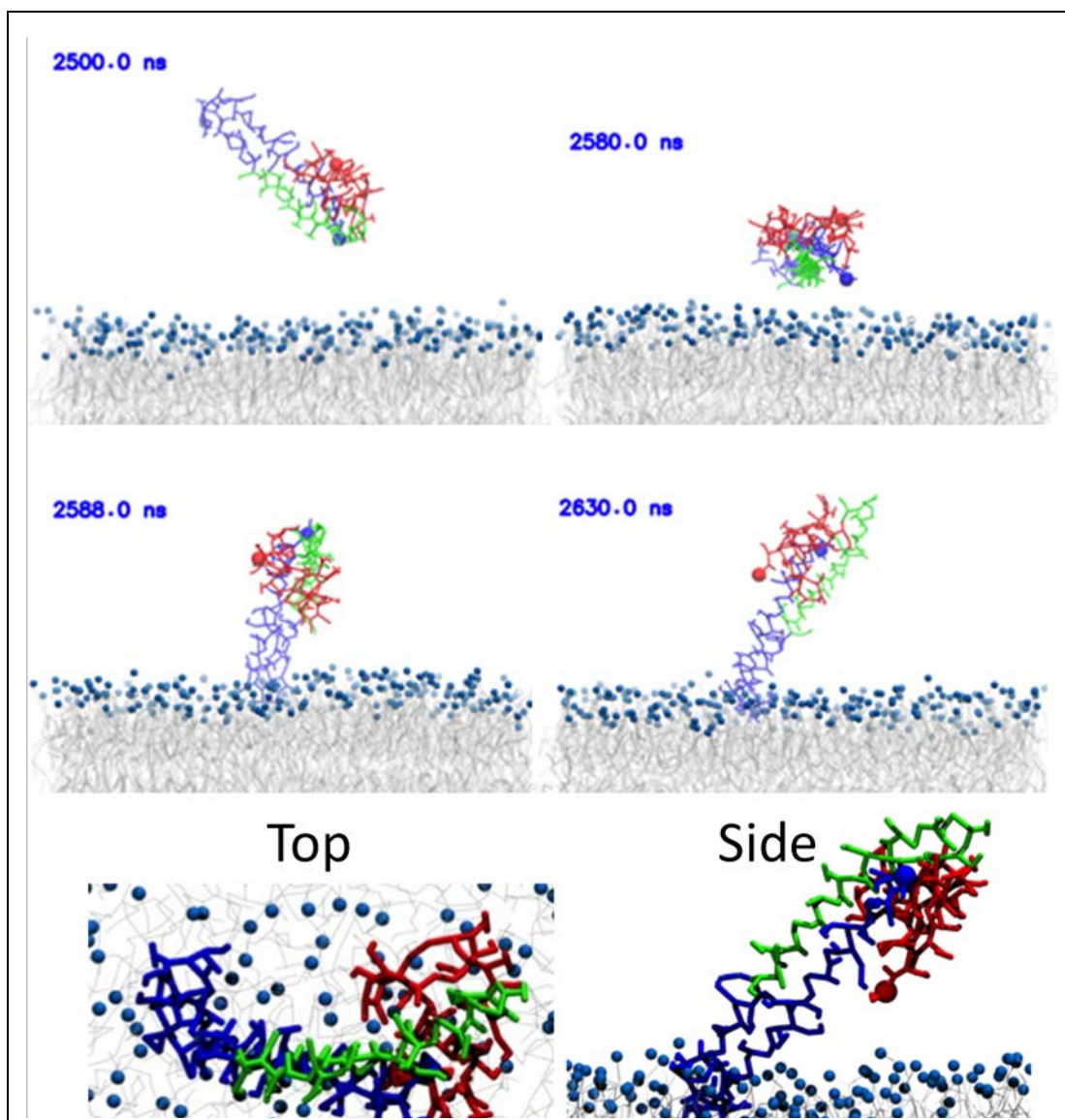
Figure 6.6. Molecular dynamics simulations of α-syn monomer interacting with POPS bilayer. The top four panels show the stable binding event to POPS. Initial interactions happen through the N-terminal, Lys rich, 36-56 segment, following which the protein is oriented in an extended conformation away from the bilayer surface. The bottom two panel, show top and side view snapshots of the last frame, at 4μs, of the MD simulation. The α-syn N-terminal segment is colored blue, the NAC region is in green, and the C-terminal segment is in red. N- and C-terminal residues are highlighted with a sphere. Lipid tails are in grey while the POPS headgroups are in blue.
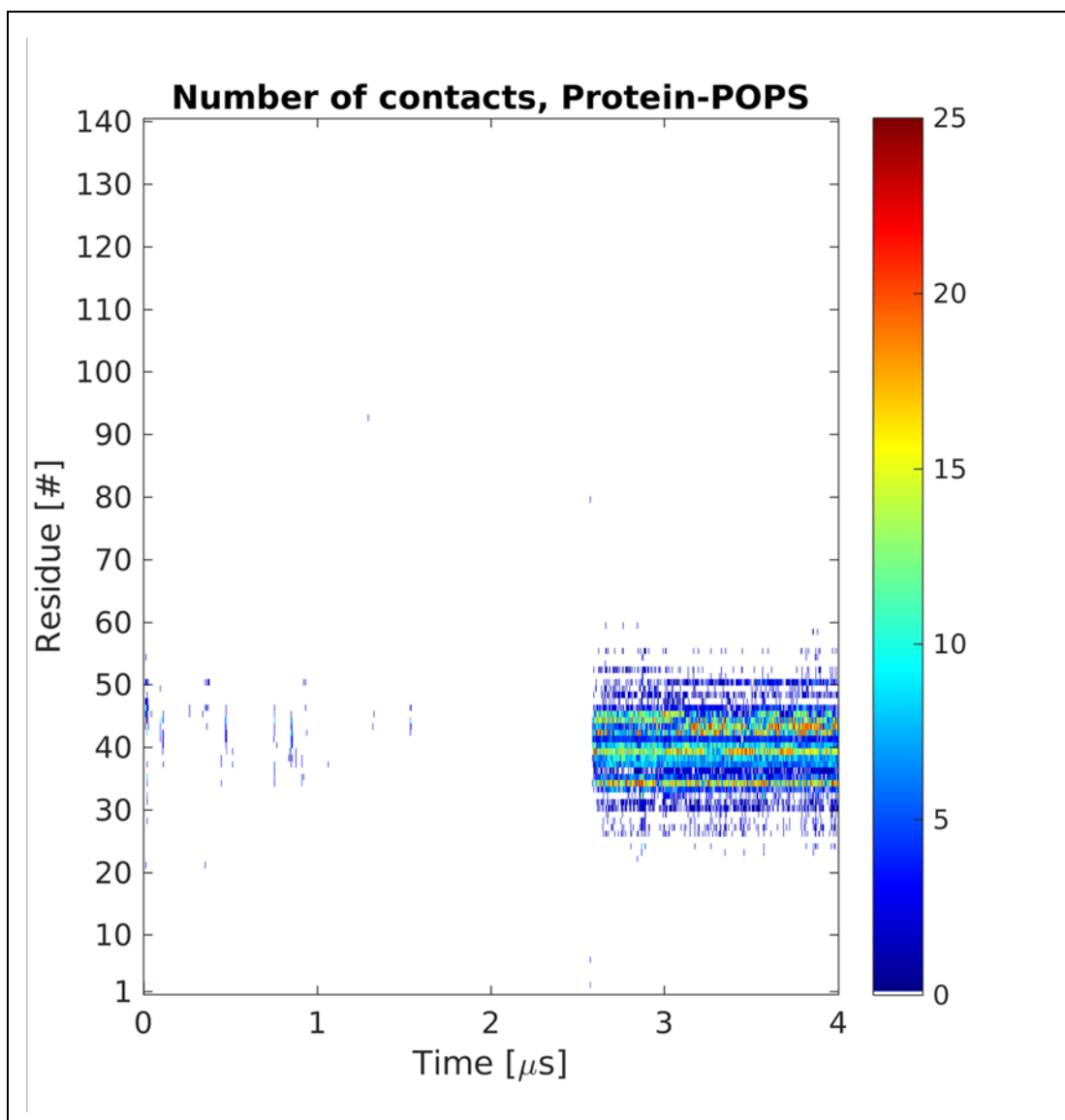
Figure 6.7. Kymograph based on molecular dynamics simulation of α-syn interaction with POPS bilayer, showing the time dependent residue-specific interactions with the bilayer. The colorbar represents number of contacts that each residue of the protein makes with the bilayer.
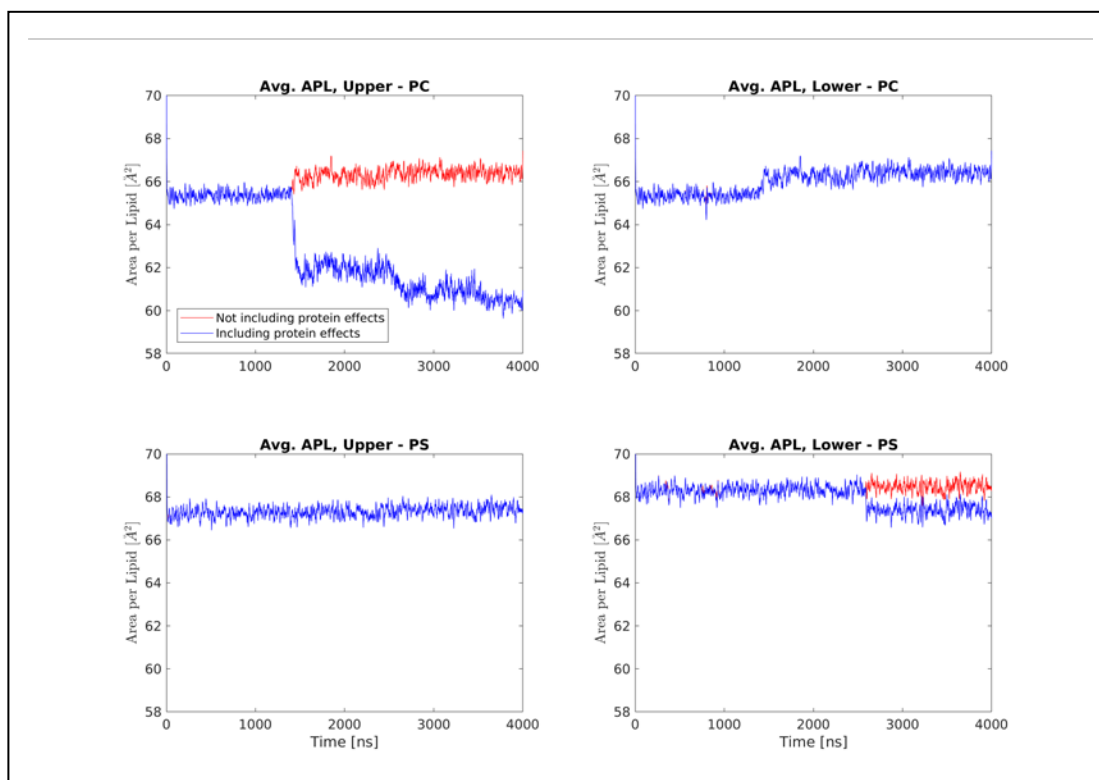
Figure 6.8. Effect of α-syn monomer interactions on the area per lipid for bilayers. Data for individual leaflets of POPC, **top**, and POPS bilayers, **bottom**, are plotted. **Right column** shows the upper leaflets while **left column** the lower. Red curves represent the APL without considering protein interactions while blue curves take into account protein interactions, curves were obtained using GridMAT-MD.

the lower leaflet, not interacting with the monomer, the APL sees an increase of approximately ~2Å^2, **Figure 6.8 top**. Similar compressive behavior is seen for the leaflet of POPS bilayer that interacts with α-syn monomer albeit smaller change compared to POPC, **Figure 6.8 bottom**.

The thickness of the bilayer is another important property that can be used to measure the effect of α-syn monomer interactions. The POPC bilayer thickness experiences a change in thickness of approximately 0.45nm during the simulation, **Figure 6.9**. Comparing the results of the thickness analysis when including protein interactions, **bottom**, and not including protein interactions, **top**, it is clear that the change in the bilayer thickness is localized in the area directly interacting with the α-syn monomer. As was the case for the change in APL, the POPS bilayer does not experience a large change in thickness, **Figure 6.10**.

Interaction of two α-syn Monomers with Lipid Bilayers

To investigate the effect of the different binding modalities of α-syn monomer on the aggregation properties, we modeled the interaction of membrane-bound α-syn with a second free α-syn molecule; the results are shown in **Figure 6.11**. At the start of the simulation the second protein is floating around the bound α-syn on POPC, but later it moves away from the bound protein and binds to the other side of the bilayer, gradually increasing the number of segments interacting with the bilayer as shown in frames 45ns to 75ns; reminiscent of the initial interaction of the monomer with the bilayer. Simulations with POPS bilayer produce entirely different results. According to **Figure 6.12**, a free protein very rapidly binds to membrane-bound α-syn, and the dimer is formed rapidly after only 15ns via interactions involving the two protein molecules' NAC segments and via
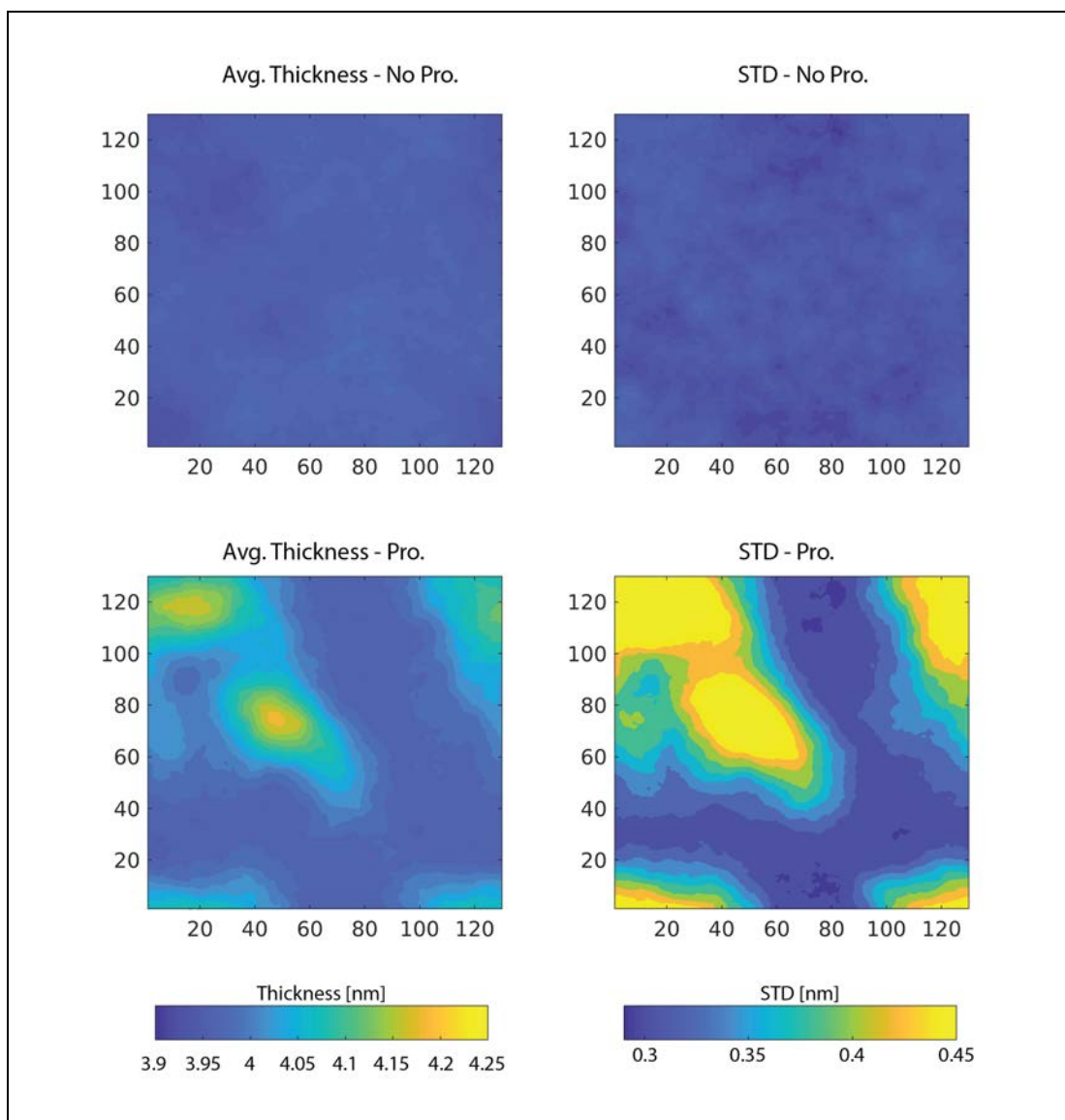
Figure 6.9. Bilayer thickness for POPC membrane interacting with α-syn monomer. **Left column** shows the mean thickness of the bilayer without considering protein interactions, **top**, and considering protein interactions, **bottom**, obtained from 4μs simulations. **Right** shows the standard deviation for the thickness measurements.
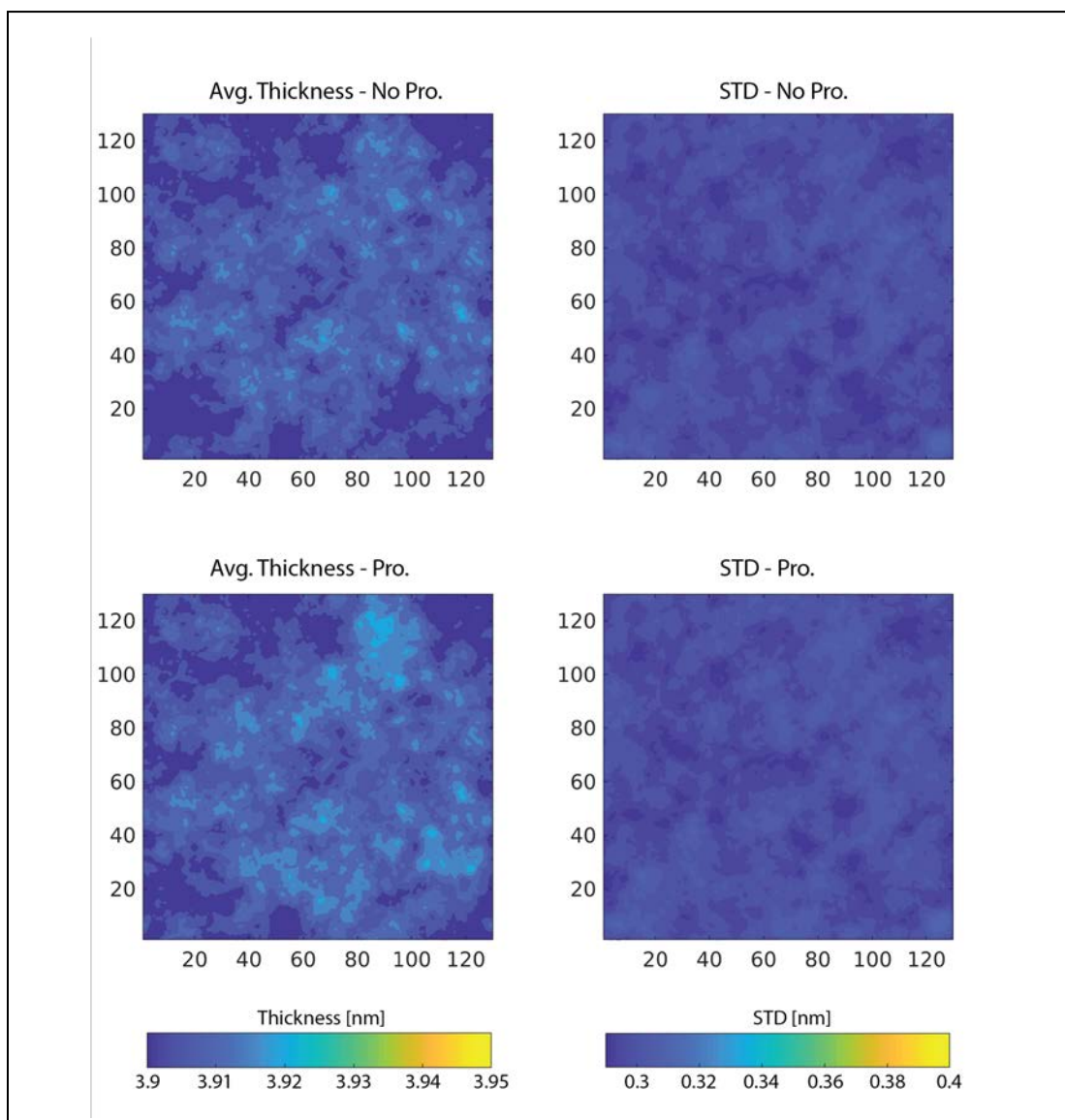
Figure 6.10. Bilayer thickness for POPS membrane interacting with α-syn monomer. **Left column**: shows the mean thickness of the bilayer without considering protein interactions, **top**, and considering protein interactions, **bottom**, obtained from 4μs simulations. **Right column**: shows the standard deviation for the thicknesses measurements.
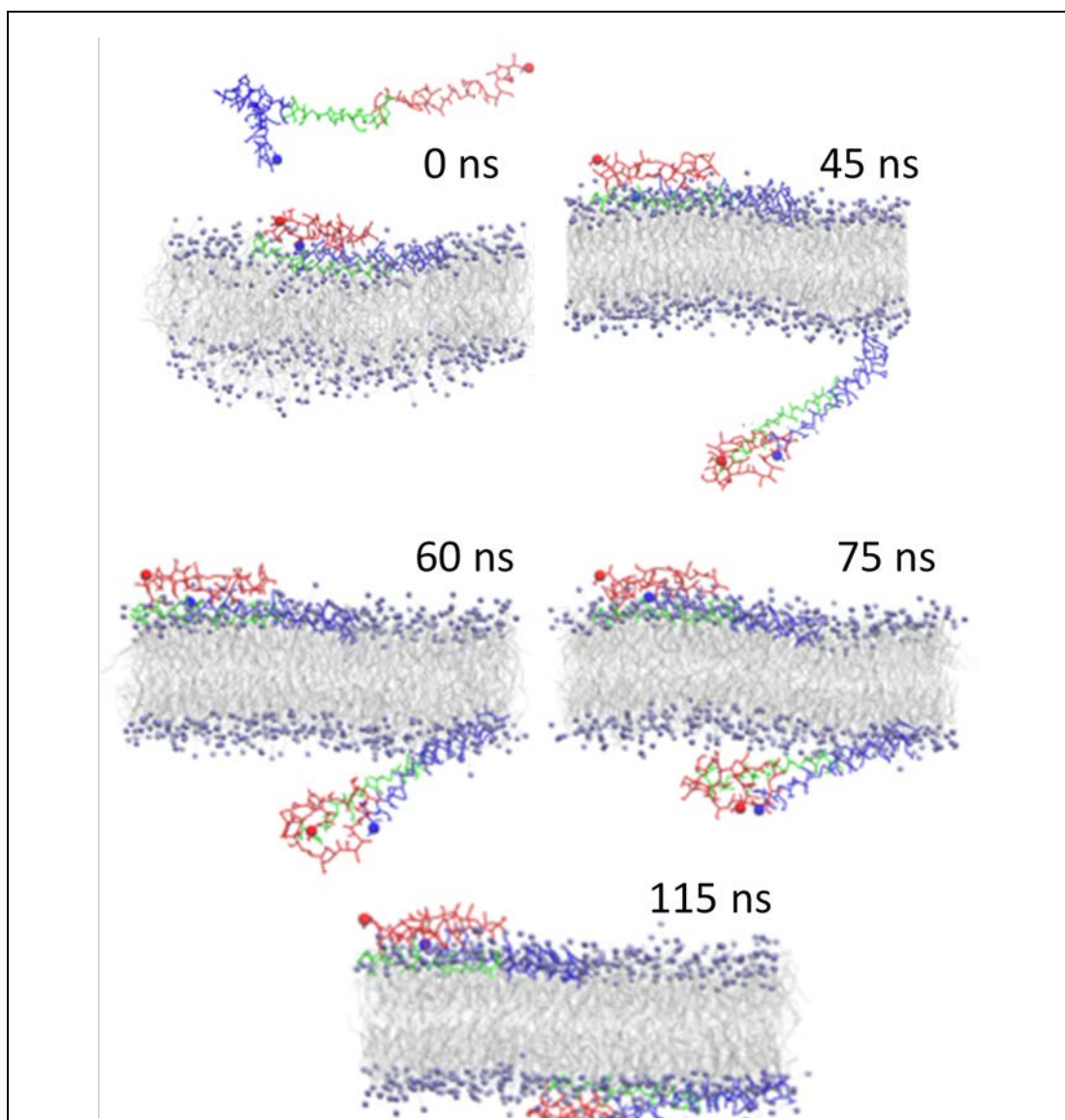
Figure 6.11. Results of MD simulations on POPC, showing interaction between a free and a membrane-bound α-syn. Binding of a free α-syn to the POPC membrane; the free α-syn traverses through the periodic boundary to the inner leaflet and stably binds; mode of interaction is similar to the initial α-syn interaction in **Figure 6.3**. The α-syn N-terminal segment is colored blue, the NAC region is in green, and the C-terminal segment is in red. N- and C-terminal residues are highlighted with a sphere. Lipid tails are in grey while the POPC headgroups are in purple.
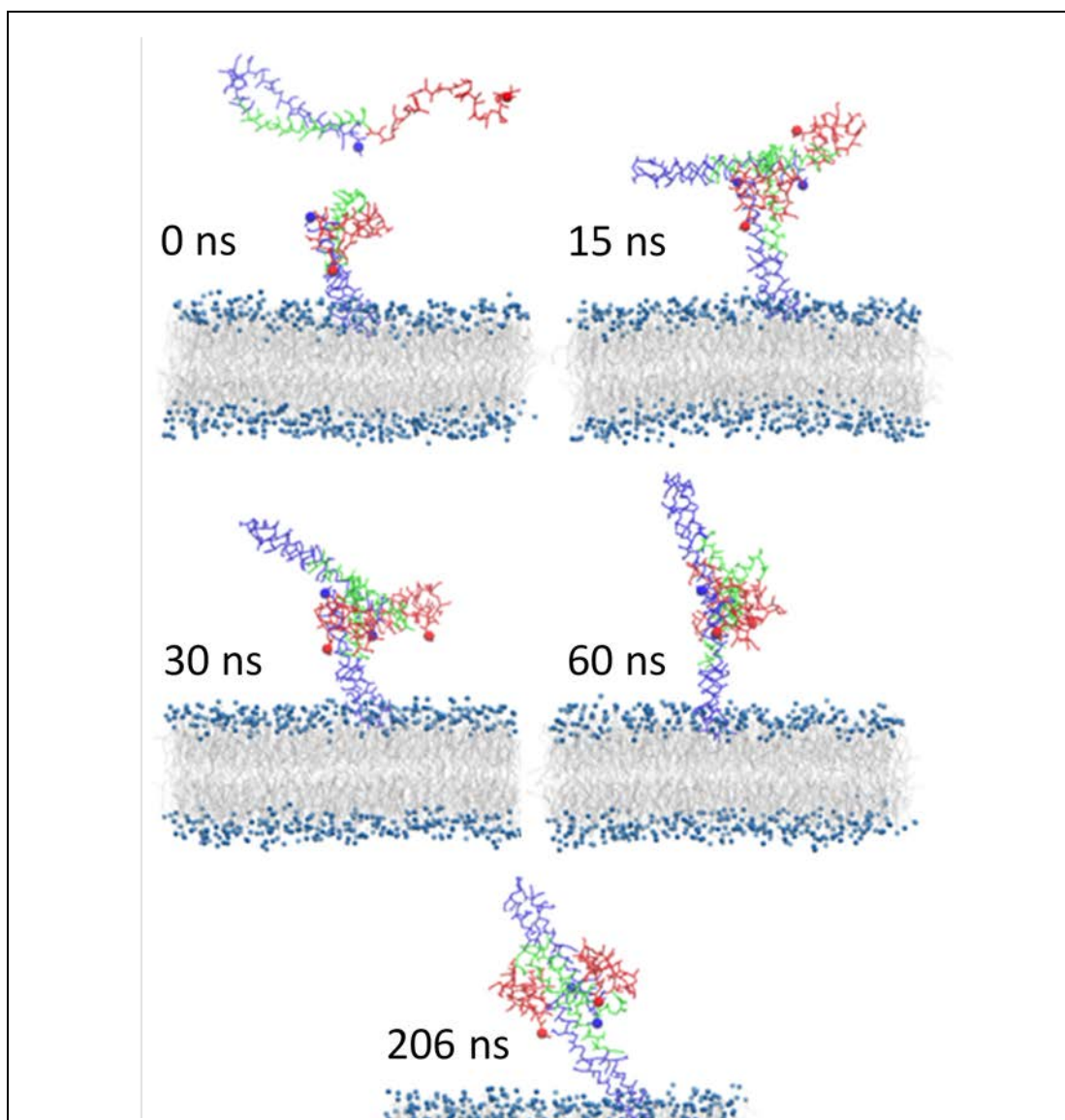
Figure 6.12. MD simulations, on POPS, of interaction between a free and a membrane-bound α-syn protein. The free α-syn rapidly binds membrane-bound α-syn through NAC-NAC and NAC-C-terminal interactions. The dimer then undergoes conformational change and finally adopts an extended shape with N-terminal helices extended away from the bilayer surface. The α-syn N-terminal segment is colored blue, the NAC region is in green, and the C-terminal segment is in red. N- and C-terminal residues are highlighted with a sphere. Lipid tails are in grey while the POPS headgroups are in blue.
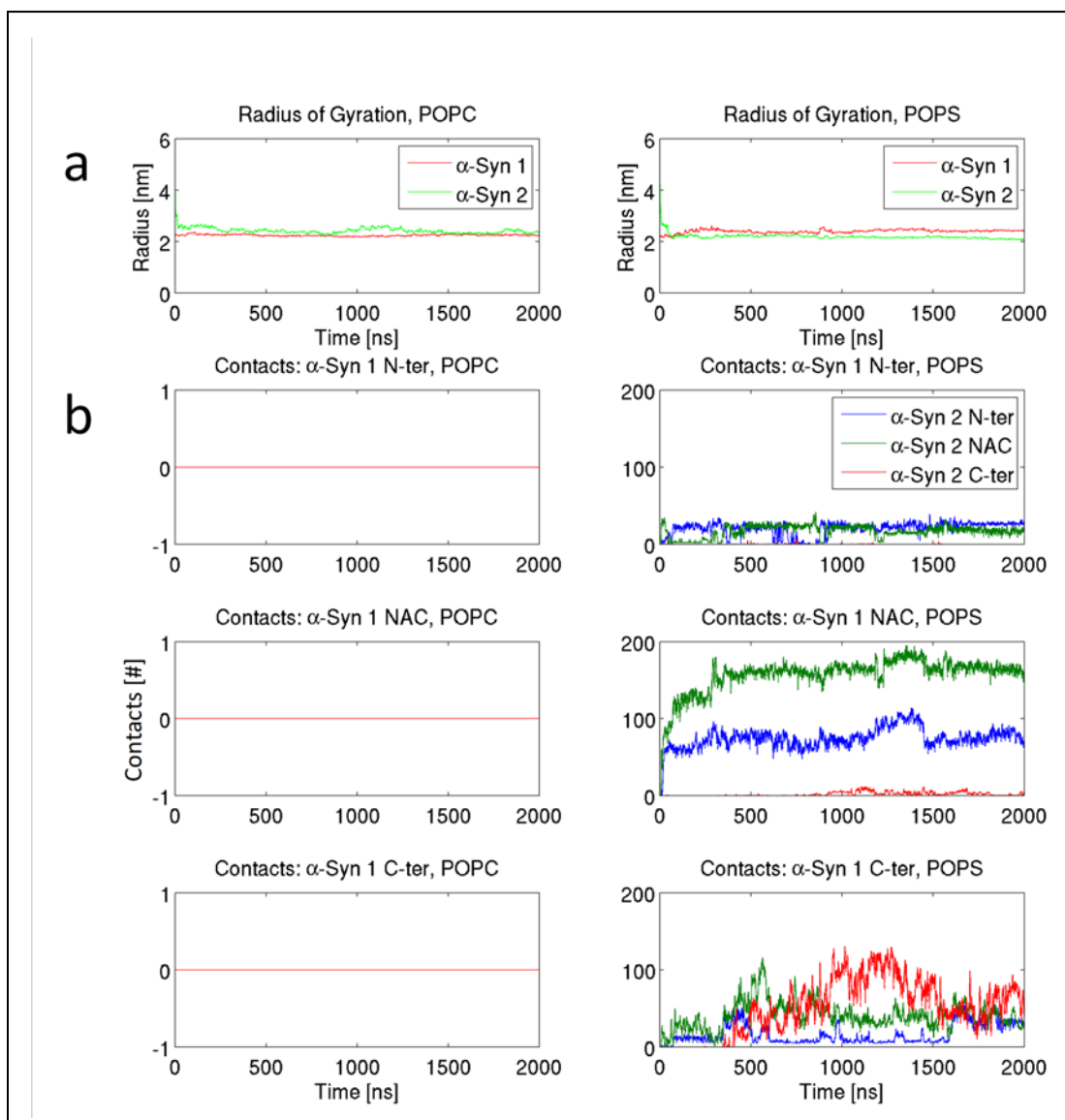
Figure 6.13. MD simulation of a free α-syn molecule interacting with membrane-bound α-syn. **(a)** Radius of gyration for membrane-bound (α-Syn 1) and free (α-Syn 2) α-syn molecules in the POPC (**left**) and POPS (**right**) systems. **(b)** Inter-peptide contacts for the α-syn molecules in the POPC (**left**) and POPS (**right**) systems. Number of contacts (distance <0.6 nm) are plotted for membrane bound α-syn (1 N-ter, 1 NAC, and 1 C-ter) and segments of the free α-syn (denoted 2) molecules.

NAC-C-terminal interactions. The proteins then undergo re-arrangement to a parallel orientation with an extended NAC-NAC interaction interface (30ns-60ns), and the dimer remains stable for the remainder of the simulation. Comparing the radii of gyration for the monomers interacting with POPC and POPS does not show a significant difference in their behavior, however that is not the case when other metrics are compared, **Figure 6.13**. The number of contacts between the two monomers interacting with POPC and POPS show that, on POPS, the dimer is formed and quickly stabilizes, while on POPC the two monomers do not interact at all. Furthermore, on POPS the interactions within the dimer primarily occur between the NAC and C-terminal segments of the membrane-bound protein and the second free α-syn molecule.

6.4 Discussion

Our studies demonstrate that phospholipid bilayers promote α-syn aggregation at conditions where no aggregates are assembled in bulk solution. The aggregation process was directly observed using time-lapse AFM, showing the number and size of aggregates increasing proportionally with incubation time. The efficient assembly of aggregates on phospholipid bilayers is in line with other studies (204, 212) in which acceleration of α-syn fibrils formation on phospholipid vesicles was reported. Moreover, we showed that the aggregation efficiency depends on the phospholipid composition, with general aggregation propensity on surfaces being greater for POPS compared to POPC. Furthermore, computational simulations revealed a number of important features of this self-assembly process catalyzed by the membrane bilayers.

First, simulations revealed that lysine residues are critically involved in the initial interaction with the membrane surface, suggesting that electrostatic interactions contribute

positively to the aggregation propensity, in line with (219). This also explains the data

obtained for aggregation on POPS, which shows greater aggregation propensity compared

to POPC. Moreover, bilayer composition also contributes to the α-syn conformation,

inserted into the membrane interfacial region on POPC and extending out from the

membrane on POPS, which then affects the aggregation propensity of the protein. This is

evident from the simulations with membrane-bound and free α-syn molecules; in particular

for POPS, the extended α-syn protein acts as an attachment point for free proteins to rapidly

assemble the dimer (**Figure 6.12**). This extended arrangement is in line with recent

structural data (220), according to which, three regions of membrane-bound α-syn exhibit

distinct structural and dynamic properties. Thus, that α-syn has differential binding modes

on different lipid bilayers, which may alter the overall protein structure and contribute to a

change in aggregation propensity of the protein.

Second, it is widely accepted that interaction of amyloid proteins, including α-

syn, with lipid bilayers is accompanied with the change of the bilayer structure and even

disruption of the bilayer (221-223). The formation of channel-like features assembled by

amyloid proteins oligomers is reported in (224, 225). We have not observed such changes

in the bilayer structure in the present study. In fact, simulations showed that α-syn

interaction with POPC and POPS bilayers occur through the lipid head groups and in the

interfacial region of the head groups. Moreover, while changes to the APL and thickness

of the membranes were observed, the changes did not affect the stability of the bilayers

significantly and where of a nature not associated with membrane disruption, i.e. thinning

of the membrane or insertion into the lipid tail regions. Furthermore, the absence of defects

on the SLBs, during aggregation studies and following dissociation of aggregates, suggests

Chapter 6: Interaction of *α*-synuclein with lipid bilayers

that in our experiments α-syn oligomers are not inserted into the bilayer. Explanation can be found in the concentration of amyloid protein used. For example, the α-syn pores in (224) were assembled with α-syn concentration three orders of magnitude higher than in our simulation and aggregation experiments. Another explanation can be found in the membrane structure, α-syn aggregates are reported to sense packing defects and induce lateral expansion of lipid molecules, by insertion of α-syn into the membranes (226). In our study, the bilayers were assembled defect-free and remained so during the entire time-lapse experiment, similarly the simulated bilayers were extensively equilibrated before simulations with α-syn. This is in line with data from Chaudhary and coworkers (227), in which homogeneous bilayers remain intact despite the formation of α-syn oligomers.

Third, our combined experimental and computer modeling approaches demonstrate that the on-surface aggregation is a dynamic process, so the assembled aggregate can dissociate from the surface to the bulk solution. As a result, the dissociated aggregates can play roles of seeds for aggregation in the bulk solution or act as neurotoxic agents. Both processes lead to neurodegeneration. Importantly, we found that aggregates formed on the surface are oligomers, which are considered to be the most neurotoxic amyloid aggregates.

One of critical properties of the on-surface aggregation process is the fact that aggregates form at concentrations as low as the nanomolar range, which corresponds to the typical physiological concentrations of endogenous proteins such as α-syn (214). Spontaneous assembly of aggregates in the bulk solution require concentrations several orders of magnitude higher (228). The problem of the high concentration is alleviated if the assembly occurs on the membrane bilayers. The second important feature of the on-

surface aggregation is that the composition of the bilayer contributes to the surface aggregation propensity – namely, a higher anionic lipid content favors α-syn-membrane interactions and lipid-induced α-syn aggregation. Previously reported findings suggest that the levels of anionic lipids in the brain increases with aging (229) and that the ratio of acidic to zwitterionic phospholipids increases in PD brain (230). Based on these data, our aggregation experiments, and the mechanism revealed by simulations, we hypothesize that amyloidogenic aggregates of α-syn assemble on cellular membrane and the membrane composition is the factor that controls the aggregation process (213, 231). For membranes with normal composition, assembled aggregates are unstable and dissociate as observed by computational modeling. A change in the membrane composition, such as switch from POPC rich to POPS rich, leads to a dramatic increase of stability of the dimers, facilitating the assembly of higher order oligomers. Therefore, we posit that changes in membrane composition leads to an increase in affinity of α-syn for the cell surfaces and favors the formation of stable oligomers, and thereby triggers development of the disease.

We propose the model of amyloid aggregate assembly catalyzed by cellular membranes schematically shown in **Figure 6.14**. Interaction of the protein with the membrane changes the protein conformation (panel B), facilitating the interaction with other proteins and assembly of the oligomer (panel C). The process repeats as more proteins appear leading to the assembly of larger oligomers (panel D). The assembled oligomer can dissociate from the surface to the intracellular space starting the neurodegeneration effect (panel E). In the framework of our model, the protein concentration is not a critical parameter. The property of the membrane, such as its ability to facilitate the aggregate assembly mediated by the membrane composition is the factor that defines the disease
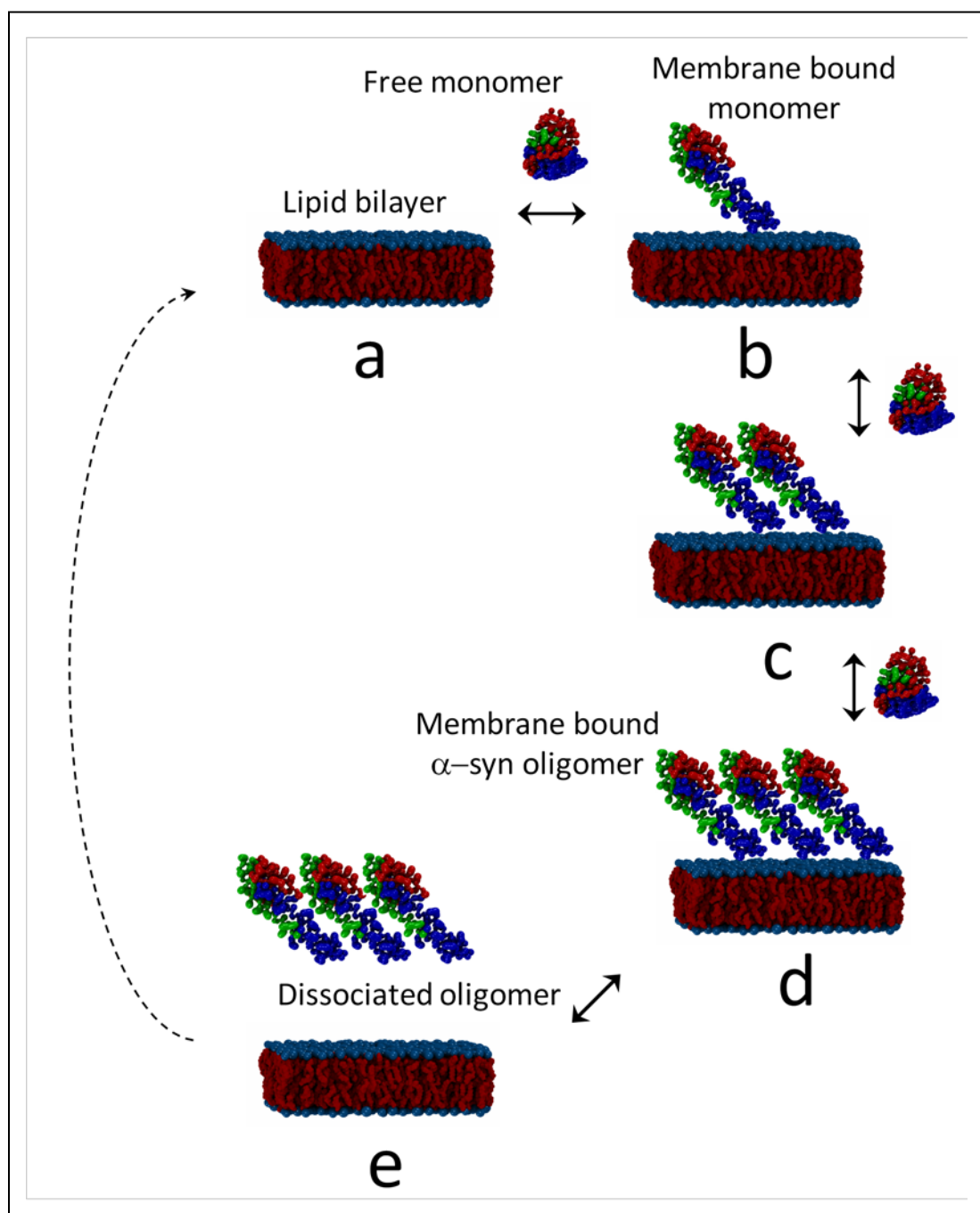
Figure 6.14. Model for membrane-mediated amyloid aggregation process. **(a)** A lipid bilayer with free α-syn monomers far from the membrane surface. **(b)** Interaction with membrane induces conformation change in the α-syn monomer. **(c)**-**(d)** The membrane-bound monomer acts as an anchor and attracts free monomers, leading to the formation of oligomers. This process can repeat multiple times, for each repeat the oligomer grows. **(e)** Oligomer dissociates from the membrane to the bulk solution.

Chapter 6: Interaction of **α**-synuclein with lipid bilayers

state, suggesting that preventions and treatments should be focused on the control the membrane composition that can be achieved by controlling the lipid metabolism.

6.5 Conclusions

We demonstrated that phospholipid bilayers dramatically facilitate aggregation of α-syn on surface, with the aggregates forming at concentrations as low as the nanomolar range. Simulations revealed that the composition of the bilayer affects the membrane-bound α-syn conformation, which contributes to the on-surface aggregation propensity. On POPS, α-syn protrudes out from the membrane surface and is able to rapidly recruit a free monomer and form a stable dimer. Furthermore, α-syn monomers were not inserted into the POPC and POPS bilayers, nor did they introduce membrane defects or thinning. Based on these observations, we propose that the interaction of amyloidogenic polypeptides with cellular membranes play a key role in the early stages of disease-prone aggregation process.

Although the data presented in this chapter were obtained for α-syn, the membrane aggregation model can be extended to other amloidogenic proteins and hence to other diseases. The support comes from our recent paper (191) in which aggregation of α-syn along with the full-size amyloid beta protein (Aβ) on mica surfaces were performed. For both proteins, interaction with the surface dramatically facilitated the aggregation process. Our preliminary data on aggregation of Aβ42 protein revealed a similar property for aggregation on both POPC and POPS bilayers and support our membrane-mediated model for amyloid aggregation as the molecular mechanism of development of neurodegenerative diseases.

Chapter 7.   CONCLUSIONS

The research described in this thesis provide a number of important contributions to understanding the molecular mechanism of early stages of amyloid self-assembly.

We first demonstrated that the hairpin fold, a structure found in the early folding intermediates of amyloid β, induces morphological and stability changes in the aggregates of Aβ(14-23) peptide. While monomers form fibrillar aggregates, the hairpin only produces spherical structures. Meanwhile, AFM force spectroscopy measurements demonstrated that the strength of hairpin-monomer interaction is considerably higher than that of hairpin-hairpin. This trend was also observed for the lifetime measurements, which showed that the hairpin-monomer complex has a longer lifetime compared to the hairpin-hairpin. We structurally characterized the interactions of the two peptides using extended MD simulations, which revealed a novel intercalated type complex for the hairpin-monomer. Monte Carlo simulations of the AFM pulling experiments further demonstrated that the intercalated assembly produces a high dissociation force that is in good agreement with experiments. Together these finding suggest that the initial folding pattern of amyloid proteins define the aggregation pathway.

We then used computational analysis to characterize the aggregation of Aβ40 into dimers and reveal their dynamic properties and compared these dimers to dimers of Aβ42. Aβ42 dimer did not show parallel in-register β-sheet structures, as one may expect based on the known structures of Aβ42 fibrils, rather dimers are stabilized by hydrophobic interactions in the central hydrophobic regions (L17-A21). Similarly, dimer structure for Aβ40, that best reproduce the experimentally observed data, are stabilized by interactions

in the N-terminal regions, and to a small extent the CHC segments. Comparison between Aβ40 and Aβ42 showed that overall, the dimers of both alloforms exhibit similar interaction strengths. However, the interaction maps, and more importantly the patterns, clearly show differences.

To further characterize the initial aggregation stages, we investigated the aggregation of amyloid β peptides and α-syn in presence of functionalized mica surfaces, based on previous observation of dimerization of α-syn on a PEG surface. All amyloid β peptides, Aβ(14-23) and full-length Aβ42, as well as α-syn exhibited dramatic increase in aggregation in presence of the surface while virtually no aggregation was observed in the absence of surface, at nanomolar concentrations. Computational analysis showed that interaction of a monomer with the surface is accompanied by the structural transition of the monomer; another monomer can then bind to the surface-bound monomer, form a dimer in which both monomers undergo structural transition. As a result, the interaction with the surface accelerates the formation of dimers. Compared to our previous data for dimer formation in the absence of surface, we observed an almost five-fold faster structural transition. Furthermore, on-surface aggregation is a dynamic process and aggregates can dissociate from the surface. Dissociated oligomers can play roles as seeds for aggregation in the bulk solution or start a neurotoxic effect such as phosphorylation of Tau protein to initiate its misfolding and aggregation followed by neurodegeneration. The inclusion of surface-mediated aggregation in the amyloid hypothesis eliminates the problems in translating knowledge from *in vitro* aggregation studies to spontaneous appearance of aggregates in the AD brain, due to the discrepancy between concentrations of

amyloidogenic polypeptides *in vivo* versus *in vitro*. Furthermore, our model does not require an elevation of amyloid synthesis.

Building on the previous results obtained for surface-mediated aggregation, we investigated the aggregation behavior of α-syn on supported lipid bilayers, acting as a model cell membrane. Our studies demonstrate that phospholipid bilayers promote α-syn aggregation at conditions where no aggregates are assembled in bulk solution. The aggregation efficiency depends on the phospholipid composition, with general aggregation propensity on surfaces being higher for POPS compared to POPC. Computational studies revealed that lysine residues play a role in the initial interaction with the membrane surface. Moreover, we found that membrane composition has an effect on the protein orientation; in particular for POPS, the α-syn protein is extended from the bilayer and acts as an attachment point for free proteins to assemble the dimer. In addition to gradual growth of the aggregates, some of them can dissociate from the surface to the bulk solution; in presence of SLBs, we measured a dramatic increase of aggregates in the solution. As a result, the dissociated aggregates can play roles of seeds for aggregation in the bulk solution or act as neurotoxic agents.

Overall, the studies described in this thesis provide the structural basis for the early stages of misfolding and aggregation process of amyloid proteins and introduces a new pathway of aggregation, the surface-mediated aggregation. Atomistic models of the interactions of amyloids with bilayer membranes lead to the next step in elucidation of the oligomerization process and lay a foundation for the development of prevention and treatments for AD, PD, and other neurodegenerative diseases based on protein aggregation.

7.1 Prospects

The characterization of the assembly process for Aβ dimers and understanding the role of multiple interactions underlying the Aβ self-assembly process provides a fundamental step toward elucidating the Aβ oligomer structures. We found that interactions between monomers, and the structural transition of monomers, are key to the formation of the early dimeric aggregates that exhibit dynamic behavior and lack long β-structures. Furthermore, we discovered the catalytic effect of surfaces, mica and lipid bilayers, enabling the formation of amyloid oligomers at physiological concentration levels. Our findings also eliminate a major problem with understanding the spontaneous appearance of plaques in the AD brain without elevation of the protein concentration. These findings are of utmost importance, as current drug discovery attempts for potential drugs against Aβ oligomers are based on the Aβ structure within highly ordered fibrils, an irrelevant structure for the highly toxic oligomers, and only consider elevation of amyloid protein concentrations as cause of aggregation; this in turn explains the rather modest progress in the AD drug discovery area. Our long-term goals are to elucidate properties of disease-prone states, explain mechanisms of their formation, and identify toxic conformations. With the ultimate goal being translation of this knowledge for development of early diagnostic markers and preventive and therapeutic agents.

In the current project, we presented atomistic models for dimeric conformations of amyloid proteins, validated by AFM-based force spectroscopy, and showed that formation of dimers is greatly enhanced in the presence of mica surfaces and lipid bilayers. However, experimental and computational studies undertaken during this project only probed the aggregation behavior of the wild-type proteins, and in the case of Aβ, only the

Aβ40 and Aβ42 alloforms. Hereditary mutations in α-syn (232) and Aβ (16, 233) have been linked with the early onset of PD and AD, respectively. Furthermore, investigations showed that the aggregation propensities and pathways are different depending on the mutation. Therefore, extension of the current study to include the mutants of α-syn and Aβ is the logical future direction.

In the current study, the novel surface-mediated aggregation pathway was only explored for simple models of cellular membranes, symmetric homogenous lipid bilayers. In the cell a plethora of different membranes with a variety of properties are available and, depending on the cell type, different membrane compositions are also possible (234). Systematic investigation of different homogenous membranes, including important constituents e.g. cholesterol, are needed to characterize the behavior of amyloid proteins in presence of biologically available and important surfaces. Furthermore, investigation of the effect of bilayers formed from lipid mixtures is also an important step towards understanding the mechanism of interaction and aggregation of amyloid proteins on cellular surfaces.

Overall, the combination of single-molecule based methodologies, to quantitatively measure protein-protein and protein-membrane interactions, with the capabilities of molecular dynamics simulations to elucidate the structural characteristics and molecular mechanisms open new venues for pharmaceutical and biomedical research for targeting protein aggregation diseases at the earliest stages of development. In addition, knowledge generated in such endeavors is crucial for the development of early diagnostic markers and preventive and therapeutic agents.

Chapter 8.   REFERENCES

1.   Rosenbaum DM, Rasmussen SG, Kobilka BK. The structure and function of G-protein-coupled receptors. Nature. 2009;459(7245):356-63.

2.   Martinez Cuesta S, Rahman SA, Furnham N, Thornton JM. The Classification and Evolution of Enzyme Function. Biophys J. 2015;109(6):1082-6.

3.   Fischer RS, Fowler VM. Thematic Minireview Series: The State of the Cytoskeleton in 2015. J Biol Chem. 2015;290(28):17133-6.

4.   Selkoe DJ. Cell biology of protein misfolding: the examples of Alzheimer's and Parkinson's diseases. Nat Cell Biol. 2004;6(11):1054-61.

5.   Burdick D, Soreghan B, Kwon M, Kosmoski J, Knauer M, Henschen A, et al. Assembly and aggregation properties of synthetic Alzheimer's A4/beta amyloid peptide analogs. Journal of Biological Chemistry. 1992;267(1):546-54.

6.   Perutz MF, Finch JT, Berriman J, Lesk A. Amyloid fibers are water-filled nanotubes. Proc Natl Acad Sci U S A. 2002;99(8):5591-5.

7.   Lu JX, Qiang W, Yau WM, Schwieters CD, Meredith SC, Tycko R. Molecular structure of beta-amyloid fibrils in Alzheimer's disease brain tissue. Cell. 2013;154(6):1257-68.

8.   Lasagna-Reeves CA, Castillo-Carranza DL, Sengupta U, Guerrero-Munoz MJ, Kiritoshi T, Neugebauer V, et al. Alzheimer brain-derived tau oligomers propagate pathology from endogenous tau. Sci Rep. 2012;2:700.

9.   Irvine GB, El-Agnaf OM, Shankar GM, Walsh DM. Protein aggregation in the brain: the molecular basis for Alzheimer's and Parkinson's diseases. Mol Med. 2008;14(7-8):451-64.

10.   Chiti F, Dobson CM. Protein Misfolding, Functional Amyloid, and Human Disease. Annu Rev Biochem. 2006;75(1):333-66.

11.   Petkova AT, Leapman RD, Guo Z, Yau W-M, Mattson MP, Tycko R. Self-Propagating, Molecular-Level Polymorphism in Alzheimer's ß-Amyloid Fibrils. Science. 2005;307(5707):262-5.

12.   Dobson CM. Protein folding and misfolding. Nature. 2003;426(6968):884-90.

13.   Dobson CM. Principles of protein folding, misfolding and aggregation. Semin Cell Dev Biol. 2004;15(1):3-16.

14.   Ross CA, Poirier MA. Protein aggregation and neurodegenerative disease. Nat Med. 2004;10 Suppl:S10-7.

15.   Selkoe DJ. The molecular pathology of Alzheimer's disease. Neuron. 1991;6(4):487-98.

16.   Selkoe DJ. Alzheimer's disease: genes, proteins, and therapy. Physiol Rev. 2001;81(2):741-66.

17.   Hardy J, Selkoe DJ. The amyloid hypothesis of Alzheimer's disease: progress and problems on the road to therapeutics. Science. 2002;297(5580):353-6.

18.   2014 Alzheimer's disease facts and figures. Alzheimer's & Dementia. 2014;10(2):e47-e92.

19.   Global, regional, and national incidence, prevalence, and years lived with disability for 310 diseases and injuries, 1990–2015: a systematic analysis for the Global Burden of Disease Study 2015. The Lancet. 2016;388(10053):1545-602.

20.   Alzheimer's A. Changing the Trajectory of Alzheimer's Disease: How a Treatment by 2025 Saves Lives and Dollars.

21.   Glenner GG, Wong CW. Alzheimer's disease: Initial report of the purification and characterization of a novel cerebrovascular amyloid protein. Biochemical and Biophysical Research Communications. 1984;120(3):885-90.

22.   Graeber MB, Kösel S, Egensperger R, Banati RB, Müller U, Bise K, et al. Rediscovery of the case described by Alois Alzheimer in 1911: historical, histological and molecular genetic analysis. Neurogenetics. 1997;1(1):73-80.

23.   Kang J, Lemaire HG, Unterbeck A, Salbaum JM, Masters CL, Grzeschik KH, et al. The precursor of Alzheimer's disease amyloid A4 protein resembles a cell-surface receptor. Nature. 1987;325(6106):733-6.

24.   Tomita T, Maruyama K, Saido TC, Kume H, Shinozaki K, Tokuhiro S, et al. The presenilin 2 mutation (N141I) linked to familial Alzheimer disease (Volga German families) increases the secretion of amyloid beta protein ending at the 42nd (or 43rd) residue. Proc Natl Acad Sci U S A. 1997;94(5):2025-30.

25.   O'Nuallain B, Shivaprasad S, Kheterpal I, Wetzel R. Thermodynamics of A beta(1-40) amyloid fibril elongation. Biochemistry. 2005;44(38):12709-18.

26.   Hellstrand E, Boland B, Walsh DM, Linse S. Amyloid beta-protein aggregation produces highly reproducible kinetic data and occurs by a two-phase process. ACS Chem Neurosci. 2010;1(1):13-8.

27.   Vandersteen A, Hubin E, Sarroukh R, De Baets G, Schymkowitz J, Rousseau F, et al. A comparative analysis of the aggregation behavior of amyloid-beta peptide variants. FEBS Lett. 2012;586(23):4088-93.

28.   Murphy MP, LeVine H, 3rd. Alzheimer's disease and the amyloid-beta peptide. J Alzheimers Dis. 2010;19(1):311-23.

29.   Bibl M, Gallus M, Welge V, Lehmann S, Sparbier K, Esselmann H, et al. Characterization of cerebrospinal fluid aminoterminally truncated and oxidized amyloid-beta peptides. Proteomics Clin Appl. 2012;6(3-4):163-9.

30.   Hardy JA, Higgins GA. Alzheimer's disease: the amyloid cascade hypothesis. Science. 1992;256(5054):184.

31.   Luhrs T, Ritter C, Adrian M, Riek-Loher D, Bohrmann B, Dobeli H, et al. 3D structure of Alzheimer's amyloid-beta(1-42) fibrils. Proc Natl Acad Sci U S A. 2005;102(48):17342-7.

32.   Miller LM, Wang Q, Telivala TP, Smith RJ, Lanzirotti A, Miklossy J. Synchrotron-based infrared and X-ray imaging shows focalized accumulation of Cu and Zn co-localized with beta-amyloid deposits in Alzheimer's disease. J Struct Biol. 2006;155(1):30-7.

33.   Xiao Y, Ma B, McElheny D, Parthasarathy S, Long F, Hoshi M, et al. Aβ(1-42) fibril structure illuminates self-recognition and replication of amyloid in Alzheimer's disease. Nat Struct Mol Biol. 2015;22(6):499-505.

34.   Walti MA, Ravotti F, Arai H, Glabe CG, Wall JS, Bockmann A, et al. Atomic-resolution structure of a disease-relevant Abeta(1-42) amyloid fibril. Proc Natl Acad Sci U S A. 2016;113(34):E4976-84.

35.   Bitan G, Kirkitadze MD, Lomakin A, Vollers SS, Benedek GB, Teplow DB. Amyloid beta - protein (Abeta) assembly: Abeta 40 and Abeta 42 oligomerize through distinct pathways. Proc Natl Acad Sci U S A. 2003;100(1):330-5.

36.   Schmidt M, Sachse C, Richter W, Xu C, Fandrich M, Grigorieff N. Comparison of Alzheimer Abeta(1-40) and Abeta(1-42) amyloid fibrils reveals similar protofilament structures. Proc Natl Acad Sci U S A. 2009;106(47):19813-8.

37.   Walsh DM, Lomakin A, Benedek GB, Condron MM, Teplow DB. Amyloid β-Protein Fibrillogenesis: DETECTION OF A PROTOFIBRILLAR INTERMEDIATE. Journal of Biological Chemistry. 1997;272(35):22364-72.

38.   Glabe CG. Structural classification of toxic amyloid oligomers. J Biol Chem. 2008;283(44):29639-43.

39.   Teplow DB. Structural and kinetic features of amyloid β-protein fibrillogenesis. Amyloid. 1998;5(2):121-42.

Chapter 8: References

40.   Lyubchenko YL, Sherman S, Shlyakhtenko LS, Uversky VN. Nanoimaging for protein misfolding and related diseases. J Cell Biochem. 2006;99(1):52-70.

41.   Hoyer W, Cherny D, Subramaniam V, Jovin TM. Rapid self-assembly of alpha-synuclein observed by in situ atomic force microscopy. J Mol Biol. 2004;340(1):127-39.

42.   Watanabe-Nakayama T, Ono K, Itami M, Takahashi R, Teplow DB, Yamada M. High-speed atomic force microscopy reveals structural dynamics of amyloid beta1-42 aggregates. Proc Natl Acad Sci U S A. 2016;113(21):5835-40.

43.   Sachse C, Fandrich M, Grigorieff N. Paired beta-sheet structure of an Abeta(1-40) amyloid fibril revealed by electron microscopy. Proc Natl Acad Sci U S A. 2008;105(21):7462-6.

44.   Jimenez JL, Guijarro JI, Orlova E, Zurdo J, Dobson CM, Sunde M, et al. Cryo-electron microscopy structure of an SH3 amyloid fibril and model of the molecular packing. EMBO J. 1999;18(4):815-21.

45.   Gremer L, Scholzel D, Schenk C, Reinartz E, Labahn J, Ravelli RBG, et al. Fibril structure of amyloid-beta(1-42) by cryo-electron microscopy. Science. 2017;358(6359):116-9.

46.   Colvin MT, Silvers R, Ni QZ, Can TV, Sergeyev I, Rosay M, et al. Atomic Resolution Structure of Monomorphic Abeta42 Amyloid Fibrils. J Am Chem Soc. 2016;138(30):9663-74.

47.   Landreh M, Sawaya MR, Hipp MS, Eisenberg DS, Wuthrich K, Hartl FU. The formation, function and regulation of amyloids: insights from structural biology. J Intern Med. 2016;280(2):164-76.

48.   Kajava AV, Baxa U, Steven AC. Beta arcades: recurring motifs in naturally occurring and disease-related amyloid fibrils. FASEB J. 2010;24(5):1311-9.

49.   Crescenzi O, Tomaselli S, Guerrini R, Salvadori S, D'Ursi AM, Temussi PA, et al. Solution structure of the Alzheimer amyloid β-peptide (1–42) in an apolar microenvironment. Euro J Biochem. 2002;269(22):5642-8.

50.   Sgourakis NG, Merced-Serrano M, Boutsidis C, Drineas P, Du Z, Wang C, et al. Atomic-Level Characterization of the Ensemble of the Aβ(1–42) Monomer in Water Using Unbiased Molecular Dynamics Simulations and Spectral Algorithms. J Mol Biol. 2011;405(2):570-83.

51.   Vivekanandan S, Brender JR, Lee SY, Ramamoorthy A. A partially folded structure of amyloid-beta(1-40) in an aqueous environment. Biochem Biophys Res Commun. 2011;411(2):312-6.

52.   Jaroniec CP, MacPhee CE, Bajaj VS, McMahon MT, Dobson CM, Griffin RG. High-resolution molecular structure of a peptide in an amyloid fibril determined by magic angle spinning NMR spectroscopy. Proc Natl Acad Sci U S A. 2004;101(3):711-6.

53.   Parthasarathy S, Inoue M, Xiao Y, Matsumura Y, Nabeshima Y, Hoshi M, et al. Structural Insight into an Alzheimer's Brain-Derived Spherical Assembly of Amyloid beta by Solid-State NMR. J Am Chem Soc. 2015;137(20):6480-3.

54.   Xu L, Nussinov R, Ma B. Allosteric stabilization of the amyloid-beta peptide hairpin by the fluctuating N-terminal. Chemical communications (Cambridge, England). 2016;52(8):1733-6.

55.   Abelein A, Abrahams JP, Danielsson J, Graslund A, Jarvet J, Luo J, et al. The hairpin conformation of the amyloid beta peptide is an important structural motif along the aggregation pathway. Journal of biological inorganic chemistry : JBIC : a publication of the Society of Biological Inorganic Chemistry. 2014;19(4-5):623-34.

56.   Selkoe DJ, Hardy J. The amyloid hypothesis of Alzheimer's disease at 25 years. EMBO Mol Med. 2016;8(6):595-608.

57.   Ahmed M, Davis J, Aucoin D, Sato T, Ahuja S, Aimoto S, et al. Structural conversion of neurotoxic amyloid-beta(1-42) oligomers to fibrils. Nat Struct Mol Biol. 2010;17(5):561-7.

58.   Benilova I, Karran E, De Strooper B. The toxic Abeta oligomer and Alzheimer's disease: an emperor in need of clothes. Nat Neurosci. 2012;15(3):349-57.

Chapter 8: References

59.   Zhao LN, Long H, Mu Y, Chew LY. The toxicity of amyloid beta oligomers. Int J Mol Sci. 2012;13(6):7303-27.

60.   Glabe CG. Common mechanisms of amyloid oligomer pathogenesis in degenerative disease. Neurobiol Aging. 2006;27(4):570-5.

61.   Yu L, Edalji R, Harlan JE, Holzman TF, Lopez AP, Labkovsky B, et al. Structural Characterization of a Soluble Amyloid β-Peptide Oligomer. Biochemistry. 2009;48(9):1870-7.

62.   Laganowsky A, Liu C, Sawaya MR, Whitelegge JP, Park J, Zhao M, et al. Atomic view of a toxic amyloid small oligomer. Science. 2012;335(6073):1228-31.

63.   Liu P, Reed MN, Kotilinek LA, Grant MK, Forster CL, Qiang W, et al. Quaternary Structure Defines a Large Class of Amyloid-beta Oligomers Neutralized by Sequestration. Cell Rep. 2015;11(11):1760-71.

64.   Zhang Y, McLaughlin R, Goodyer C, LeBlanc A. Selective cytotoxicity of intracellular amyloid beta peptide1-42 through p53 and Bax in cultured primary human neurons. J Cell Biol. 2002;156(3):519-29.

65.   Rajasekhar K, Chakrabarti M, Govindaraju T. Function and toxicity of amyloid beta and recent therapeutic interventions targeting amyloid beta in Alzheimer's disease. Chemical communications (Cambridge, England). 2015;51(70):13434-50.

66.   Nagy Z, Esiri MM, Smith AD. The cell division cycle and the pathophysiology of Alzheimer's disease. Neuroscience. 1998;87(4):731-9.

67.   Snyder EM, Nong Y, Almeida CG, Paul S, Moran T, Choi EY, et al. Regulation of NMDA receptor trafficking by amyloid-beta. Nat Neurosci. 2005;8(8):1051-8.

68.   Shankar GM, Bloodgood BL, Townsend M, Walsh DM, Selkoe DJ, Sabatini BL. Natural oligomers of the Alzheimer amyloid-beta protein induce reversible synapse loss by modulating an NMDA-type glutamate receptor-dependent signaling pathway. J Neurosci. 2007;27(11):2866-75.

69.   Hsieh H, Boehm J, Sato C, Iwatsubo T, Tomita T, Sisodia S, et al. AMPAR removal underlies Abeta-induced synaptic depression and dendritic spine loss. Neuron. 2006;52(5):831-43.

70.   Serra-Batiste M, Ninot-Pedrosa M, Bayoumi M, Gairi M, Maglia G, Carulla N. Abeta42 assembles into specific beta-barrel pore-forming oligomers in membrane-mimicking environments. Proc Natl Acad Sci U S A. 2016;113(39):10866-71.

71.   Lashuel HA, Hartley D, Petre BM, Walz T, Lansbury PT, Jr. Neurodegenerative disease: amyloid pores from pathogenic mutations. Nature. 2002;418(6895):291.

72.   Tougu V, Tiiman A, Palumaa P. Interactions of Zn(II) and Cu(II) ions with Alzheimer's amyloid-beta peptide. Metal ion binding, contribution to fibrillization and toxicity. Metallomics. 2011;3(3):250-61.

73.   Ramamoorthy A, Lim MH. Structural characterization and inhibition of toxic amyloid-beta oligomeric intermediates. Biophys J. 2013;105(2):287-8.

74.   LaFerla FM, Green KN, Oddo S. Intracellular amyloid-beta in Alzheimer's disease. Nat Rev Neurosci. 2007;8(7):499-509.

75.   Choi JS, Braymer JJ, Nanga RP, Ramamoorthy A, Lim MH. Design of small molecules that target metal-A{beta} species and regulate metal-induced A{beta} aggregation and neurotoxicity. Proc Natl Acad Sci U S A. 2010;107(51):21990-5.

76.   Kayed R, Pensalfini A, Margol L, Sokolov Y, Sarsoza F, Head E, et al. Annular protofibrils are a structurally and functionally distinct type of amyloid oligomer. J Biol Chem. 2009;284(7):4230-7.

77.   Harper JD, Lieber CM, Lansbury PT. Atomic force microscopic imaging of seeded fibril formation and fibril branching by the Alzheimer's disease amyloid-β protein. Chemistry & Biology. 1997;4(12):951-9.

Chapter 8: References

78.	Bernstein SL, Wyttenbach T, Baumketner A, Shea JE, Bitan G, Teplow DB, et al. Amyloid beta-protein: monomer structure and early aggregation states of Abeta42 and its Pro19 alloform. J Am Chem Soc. 2005;127(7):2075-84.

79.	Walsh DM, Klyubin I, Fadeeva JV, Rowan MJ, Selkoe DJ. Amyloid-beta oligomers: their production, toxicity and therapeutic inhibition. Biochem Soc Trans. 2002;30(4):552-7.

80.	Podlisny MB, Ostaszewski BL, Squazzo SL, Koo EH, Rydell RE, Teplow DB, et al. Aggregation of secreted amyloid beta-protein into sodium dodecyl sulfate-stable oligomers in cell culture. J Biol Chem. 1995;270(16):9564-70.

81.	Necula M, Kayed R, Milton S, Glabe CG. Small molecule inhibitors of aggregation indicate that amyloid beta oligomerization and fibrillization pathways are independent and distinct. J Biol Chem. 2007;282(14):10311-24.

82.	Chromy BA, Nowak RJ, Lambert MP, Viola KL, Chang L, Velasco PT, et al. Self-assembly of Abeta(1-42) into globular neurotoxins. Biochemistry. 2003;42(44):12749-60.

83.	Shankar GM, Li S, Mehta TH, Garcia-Munoz A, Shepardson NE, Smith I, et al. Amyloid-beta protein dimers isolated directly from Alzheimer's brains impair synaptic plasticity and memory. Nat Med. 2008;14(8):837-42.

84.	Walsh DM, Tseng BP, Rydel RE, Podlisny MB, Selkoe DJ. The Oligomerization of Amyloid β-Protein Begins Intracellularly in Cells Derived from Human Brain. Biochemistry. 2000;39(35):10831-9.

85.	Ono K, Condron MM, Teplow DB. Structure-neurotoxicity relationships of amyloid beta-protein oligomers. Proc Natl Acad Sci U S A. 2009;106(35):14745-50.

86.	Sarkar B, Mithu VS, Chandra B, Mandal A, Chandrakesan M, Bhowmik D, et al. Significant structural differences between transient amyloid-beta oligomers and less-toxic fibrils in regions known to harbor familial Alzheimer's mutations. Angew Chem Int Ed Engl. 2014;53(27):6888-92.

87.	Bhowmik D, Mote KR, MacLaughlin CM, Biswas N, Chandra B, Basu JK, et al. Cell-Membrane-Mimicking Lipid-Coated Nanoparticles Confer Raman Enhancement to Membrane Proteins and Reveal Membrane-Attached Amyloid-β Conformation. ACS Nano. 2015;9(9):9070-7.

88.	Hoyer W, Gronwall C, Jonsson A, Stahl S, Hard T. Stabilization of a beta-hairpin in monomeric Alzheimer's amyloid-beta peptide inhibits amyloid formation. Proc Natl Acad Sci U S A. 2008;105(13):5099-104.

89.	Doran TM, Anderson EA, Latchney SE, Opanashuk LA, Nilsson BL. An azobenzene photoswitch sheds light on turn nucleation in amyloid-beta self-assembly. ACS Chem Neurosci. 2012;3(3):211-20.

90.	Lazo ND, Grant MA, Condron MC, Rigby AC, Teplow DB. On the nucleation of amyloid beta-protein monomer folding. Protein Sci. 2005;14(6):1581-96.

91.	Bernstein SL, Dupuis NF, Lazo ND, Wyttenbach T, Condron MM, Bitan G, et al. Amyloid-beta protein oligomerization and the importance of tetramers and dodecamers in the aetiology of Alzheimer's disease. Nat Chem. 2009;1(4):326-31.

92.	Orte A, Birkett NR, Clarke RW, Devlin GL, Dobson CM, Klenerman D. Direct characterization of amyloidogenic oligomers by single-molecule fluorescence. Proceedings of the National Academy of Sciences. 2008;105(38):14424-9.

93.	Yu H, Dee DR, Liu X, Brigley AM, Sosova I, Woodside MT. Protein misfolding occurs by slow diffusion across multiple barriers in a rough energy landscape. Proceedings of the National Academy of Sciences. 2015;112(27):8308-13.

94.	Calamai M, Pavone FS. Single Molecule Tracking Analysis Reveals That the Surface Mobility of Amyloid Oligomers Is Driven by Their Conformational Structure. Journal of the American Chemical Society. 2011;133(31):12001-8.

95.   Brucale M, Schuler B, Samorì B. Single-Molecule Studies of Intrinsically Disordered Proteins. Chemical Reviews. 2014;114(6):3281-317.

96.   Kim B-H, Palermo NY, Lovas S, Zaikova T, Keana JFW, Lyubchenko YL. Single-Molecule Atomic Force Microscopy Force Spectroscopy Study of Aβ-40 Interactions. Biochemistry. 2011;50(23):5154-62.

97.   Lv Z, Roychaudhuri R, Condron MM, Teplow DB, Lyubchenko YL. Mechanism of amyloid beta-protein dimerization determined using single-molecule AFM force spectroscopy. Sci Rep. 2013;3:2880.

98.   Krasnoslobodtsev AV, Volkov IL, Asiago JM, Hindupur J, Rochet JC, Lyubchenko YL. alpha-Synuclein misfolding assessed with single molecule AFM force spectroscopy: effect of pathogenic mutations. Biochemistry. 2013;52(42):7377-86.

99.   Kim BH, Lyubchenko YL. Nanoprobing of misfolding and interactions of amyloid beta 42 protein. Nanomedicine. 2014;10(4):871-8.

100.   Lovas S, Zhang Y, Yu J, Lyubchenko YL. Molecular Mechanism of Misfolding and Aggregation of Aβ(13–23). J Phys Chem B. 2013;117(20):6175-86.

101.   Lv Z, Krasnoslobodtsev AV, Zhang Y, Ysselstein D, Rochet J-C, Blanchard SC, et al. Direct Detection of α-Synuclein Dimerization Dynamics: Single-molecule Fluorescence Analysis. Biophysical Journal. 2015;108(8):2038-47.

102.   Lv Z, Krasnoslobodtsev AV, Zhang Y, Ysselstein D, Rochet JC, Blanchard SC, et al. Effect of acidic pH on the stability of alpha-synuclein dimers. Biopolymers. 2016;105(10):715-24.

103.   Narayan P, Orte A, Clarke RW, Bolognesi B, Hook S, Ganzinger KA, et al. The extracellular chaperone clusterin sequesters oligomeric forms of the amyloid-beta(1-40) peptide. Nat Struct Mol Biol. 2011;19(1):79-83.

104.   Breydo L, Uversky VN. Structural, morphological, and functional diversity of amyloid oligomers. FEBS Lett. 2015;589(19 Pt A):2640-8.

105.   Bemporad F, Chiti F. Protein misfolded oligomers: experimental approaches, mechanism of formation, and structure-toxicity relationships. Chem Biol. 2012;19(3):315-27.

106.   Baumketner A, Bernstein SL, Wyttenbach T, Bitan G, Teplow DB, Bowers MT, et al. Amyloid beta-protein monomer structure: a computational and experimental study. Protein Sci. 2006;15(3):420-8.

107.   Sgourakis NG, Yan Y, McCallum SA, Wang C, Garcia AE. The Alzheimer's peptides Abeta40 and 42 adopt distinct conformations in water: a combined MD / NMR study. J Mol Biol. 2007;368(5):1448-57.

108.   Zhang Y, Lyubchenko YL. The structure of misfolded amyloidogenic dimers: computational analysis of force spectroscopy data. Biophys J. 2014;107(12):2903-10.

109.   Jang S, Shin S. Computational study on the structural diversity of amyloid Beta Peptide (abeta(10-35)) oligomers. J Phys Chem B. 2008;112(11):3479-84.

110.   Fisher CK, Ullman O, Stultz CM. Comparative studies of disordered proteins with similar sequences: application to Abeta40 and Abeta42. Biophys J. 2013;104(7):1546-55.

111.   Klimov DK, Thirumalai D. Dissecting the assembly of Abeta16-22 amyloid peptides into antiparallel beta sheets. Structure. 2003;11(3):295-307.

112.   Srivastava A, Balaji PV. Molecular events during the early stages of aggregation of GNNQQNY: An all atom MD simulation study of randomly dispersed peptides. J Struct Biol. 2015;192(3):376-91.

113.   Matthes D, Gapsys V, de Groot BL. Driving forces and structural determinants of steric zipper peptide oligomer formation elucidated by atomistic simulations. J Mol Biol. 2012;421(2-3):390-416.

Chapter 8: References

114.   Cheon M, Chang I, Mohanty S, Luheshi LM, Dobson CM, Vendruscolo M, et al. Structural reorganisation and potential toxicity of oligomeric species formed during the assembly of amyloid fibrils. PLoS Comput Biol. 2007;3(9):1727-38.

115.   Zheng J, Jang H, Ma B, Tsai CJ, Nussinov R. Modeling the Alzheimer Abeta17-42 fibril architecture: tight intermolecular sheet-sheet association and intramolecular hydrated cavities. Biophys J. 2007;93(9):3046-57.

116.   Cruz L, Urbanc B, Borreguero JM, Lazo ND, Teplow DB, Stanley HE. Solvent and mutation effects on the nucleation of amyloid beta-protein folding. Proc Natl Acad Sci U S A. 2005;102(51):18258-63.

117.   Flock D, Colacino S, Colombo G, Di Nola A. Misfolding of the amyloid beta-protein: a molecular dynamics study. Proteins. 2006;62(1):183-92.

118.   Yang M, Teplow DB. Amyloid beta-protein monomer folding: free-energy surfaces reveal alloform-specific differences. J Mol Biol. 2008;384(2):450-64.

119.   Urbanc B, Cruz L, Yun S, Buldyrev SV, Bitan G, Teplow DB, et al. In silico study of amyloid beta-protein folding and oligomerization. Proc Natl Acad Sci U S A. 2004;101(50):17345-50.

120.   Urbanc B, Betnel M, Cruz L, Bitan G, Teplow DB. Elucidation of amyloid beta-protein oligomerization mechanisms: discrete molecular dynamics study. J Am Chem Soc. 2010;132(12):4266-80.

121.   Frenkel D, Smit B. Understanding molecular simulation : from algorithms to applications. 2nd ed. San Diego: Academic Press; 2002. xxii, 638 p. p.

122.   Piana S, Klepeis JL, Shaw DE. Assessing the accuracy of physical models used in protein-folding simulations: quantitative evidence from long molecular dynamics simulations. Curr Opin Struct Biol. 2014;24:98-105.

123.   Piana S, Lindorff-Larsen K, Shaw DE. How robust are protein folding simulations with respect to force field parameterization? Biophys J. 2011;100(9):L47-9.

124.   Skeby KK, Andersen OJ, Pogorelov TV, Tajkhorshid E, Schiott B. Conformational Dynamics of the Human Islet Amyloid Polypeptide in a Membrane Environment: Toward the Aggregation Prone Form. Biochemistry. 2016;55(13):2031-42.

125.   Moradi M, Tajkhorshid E. Mechanistic picture for conformational transition of a membrane transporter at atomic resolution. Proceedings of the National Academy of Sciences. 2013;110(47):18916.

126.   Wagener M, Vlieg J, Nabuurs SB. Flexible protein-ligand docking using the Fleksy protocol. J Comput Chem. 2012;33(12):1215-7.

127.   Dittrich M, Hayashi S, Schulten K. On the Mechanism of ATP Hydrolysis in F(1)-ATPase. Biophysical Journal. 2003;85(4):2253-66.

128.   Nguyen PH, Li MS, Stock G, Straub JE, Thirumalai D. Monomer adds to preformed structured oligomers of Abeta-peptides by a two-stage dock-lock mechanism. Proc Natl Acad Sci U S A. 2007;104(1):111-6.

129.   Lindorff-Larsen K, Maragakis P, Piana S, Eastwood MP, Dror RO, Shaw DE. Systematic validation of protein force fields against experimental data. PLoS One. 2012;7(2):e32131.

130.   Smith MD, Rao JS, Segelken E, Cruz L. Force-Field Induced Bias in the Structure of Abeta21-30: A Comparison of OPLS, AMBER, CHARMM, and GROMOS Force Fields. J Chem Inf Model. 2015;55(12):2587-95.

131.   Ball KA, Phillips AH, Wemmer DE, Head-Gordon T. Differences in beta-strand populations of monomeric Abeta40 and Abeta42. Biophys J. 2013;104(12):2714-24.

132.   Kahler A, Sticht H, Horn AH. Conformational stability of fibrillar amyloid-beta oligomers via protofilament pair formation - a systematic computational study. PLoS One. 2013;8(7):e70521.

133.   Rosenman DJ, Connors CR, Chen W, Wang C, Garcia AE. Abeta monomers transiently sample oligomer and fibril-like configurations: ensemble characterization using a combined MD/NMR approach. J Mol Biol. 2013;425(18):3338-59.

134.   Roychaudhuri R, Yang M, Deshpande A, Cole GM, Frautschy S, Lomakin A, et al. C-terminal turn stability determines assembly differences between Abeta40 and Abeta42. J Mol Biol. 2013;425(2):292-308.

135.   Daly S, Kulesza A, Poussigue F, Simon A-L, Choi CM, Knight G, et al. Conformational changes in amyloid-beta (12–28) alloforms studied using action-FRET, IMS and molecular dynamics simulations. Chem Sci. 2015;6(8):5040-7.

136.   Nguyen PH, Li MS, Derreumaux P. Effects of all-atom force fields on amyloid oligomerization: replica exchange molecular dynamics simulations of the Abeta(16-22) dimer and trimer. Phys Chem Chem Phys. 2011;13(20):9778-88.

137.   Lindorff-Larsen K, Piana S, Palmo K, Maragakis P, Klepeis JL, Dror RO, et al. Improved side-chain torsion potentials for the Amber ff99SB protein force field. Proteins. 2010;78(8):1950-8.

138.   Best RB, Zheng W, Mittal J. Balanced Protein-Water Interactions Improve Properties of Disordered Proteins and Non-Specific Protein Association. J Chem Theory Comput. 2014;10(11):5113-24.

139.   Krone MG, Hua L, Soto P, Zhou R, Berne BJ, Shea JE. Role of water in mediating the assembly of Alzheimer amyloid-beta Abeta16-22 protofilaments. J Am Chem Soc. 2008;130(33):11066-72.

140.   Thirumalai D, Reddy G, Straub JE. Role of water in protein aggregation and amyloid polymorphism. Acc Chem Res. 2012;45(1):83-92.

141.   Fichou Y, Schiro G, Gallat FX, Laguri C, Moulin M, Combet J, et al. Hydration water mobility is enhanced around tau amyloid fibers. Proc Natl Acad Sci U S A. 2015;112(20):6365-70.

142.   Lee M, Chang HJ, Park JY, Shin J, Park JW, Choi JW, et al. Conformational changes of Abeta (1-42) monomers in different solvents. J Mol Graph Model. 2016;65:8-14.

143.   Yang C, Li J, Li Y, Zhu X. The effect of solvents on the conformations of Amyloid β-peptide (1–42) studied by molecular dynamics simulation. Journal of Molecular Structure: THEOCHEM. 2009;895(1-3):1-8.

144.   Somavarapu AK, Kepp KP. The Dependence of Amyloid-beta Dynamics on Protein Force Fields and Water Models. Chemphyschem. 2015;16(15):3278-89.

145.   Jorgensen WL, Chandrasekhar J, Madura JD, Impey RW, Klein ML. Comparison of simple potential functions for simulating liquid water. The Journal of Chemical Physics. 1983;79(2):926-35.

146.   Monticelli L, Kandasamy SK, Periole X, Larson RG, Tieleman DP, Marrink SJ. The MARTINI Coarse-Grained Force Field: Extension to Proteins. J Chem Theory Comput. 2008;4(5):819-34.

147.   Marrink SJ, Risselada HJ, Yefimov S, Tieleman DP, de Vries AH. The MARTINI force field: coarse grained model for biomolecular simulations. J Phys Chem B. 2007;111(27):7812-24.

148.   Seo M, Rauscher S, Pomes R, Tieleman DP. Improving Internal Peptide Dynamics in the Coarse-Grained MARTINI Model: Toward Large-Scale Simulations of Amyloid- and Elastin-like Peptides. J Chem Theory Comput. 2012;8(5):1774-85.

149.   Yu H, Han W, Ma W, Schulten K. Transient beta-hairpin formation in alpha-synuclein monomer revealed by coarse-grained molecular dynamics simulation. J Chem Phys. 2015;143(24):243142.

150.   Sørensen J, Periole X, Skeby KK, Marrink S-J, Schiøtt B. Protofibrillar Assembly Toward the Formation of Amyloid Fibrils. The Journal of Physical Chemistry Letters. 2011;2(19):2385-90.

151.   Hamelberg D, Mongan J, McCammon JA. Accelerated molecular dynamics: a promising and efficient simulation method for biomolecules. J Chem Phys. 2004;120(24):11919-29.

152.   Pierce LC, Salomon-Ferrer R, Augusto FdOC, McCammon JA, Walker RC. Routine Access to Millisecond Time Scale Events with Accelerated Molecular Dynamics. J Chem Theory Comput. 2012;8(9):2997-3002.

153.   Irback A, Mohanty S. PROFASI: A Monte Carlo simulation package for protein folding and aggregation. J Comput Chem. 2006;27(13):1548-55.

154.   Jonsson SAE, Mitternacht S, Irback A. Mechanical resistance in unstructured proteins. Biophys J. 2013;104(12):2725-32.

155.   Querfurth HW, LaFerla FM. Alzheimer's Disease. New England Journal of Medicine. 2010;362(4):329-44.

156.   Trojanowski JQ, Mattson MP. Overview of protein aggregation in single, double, and triple neurodegenerative brain amyloidoses. NeuroMolecular Medicine. 2003;4(1):1-5.

157.   Haass C, Selkoe DJ. Soluble protein oligomers in neurodegeneration: lessons from the Alzheimer's amyloid [beta]-peptide. Nat Rev Mol Cell Biol. 2007;8(2):101-12.

158.   Wang Q, Wang Y, Lu HP. Revealing the secondary structural changes of amyloid β peptide by probing the spectral fingerprint characters. Journal of Raman Spectroscopy. 2013;44(5):670-4.

159.   Ji SR, Wu Y, Sui SF. Study of the correlation of secondary structure of beta-amyloid peptide (Abeta40) with the hydrophobic exposure under different conditions. General physiology and biophysics. 2002;21(4):415-27.

160.   Liu L, Li Q, Zhang S, Wang X, Hoffmann SV, Li J, et al. Identification of a Novel Parallel β-Strand Conformation within Molecular Monolayer of Amyloid Peptide. Advanced Science. 2016;3(6):1500369-n/a.

161.   Maity S, Hashemi M, Lyubchenko YL. Nano-assembly of amyloid beta peptide: role of the hairpin fold. Sci Rep. 2017;7(1):2344.

162.   Shaw DE, Deneroff MM, Dror RO, Kuskin JS, Larson RH, Salmon JK, et al. Anton, a special-purpose machine for molecular dynamics simulation. Commun ACM. 2008;51(7):91-7.

163.   Case DA, Cheatham TE, 3rd, Darden T, Gohlke H, Luo R, Merz KM, Jr., et al. The Amber biomolecular simulation programs. J Comput Chem. 2005;26(16):1668-88.

164.   Mu Y, Nguyen PH, Stock G. Energy landscape of a small peptide revealed by dihedral angle principal component analysis. Proteins. 2005;58(1):45-52.

165.   Touw WG, Baakman C, Black J, te Beek TAH, Krieger E, Joosten RP, et al. A series of PDB-related databanks for everyday needs. Nucleic Acids Research. 2015;43(D1):D364-D8.

166.   Portillo A, Hashemi M, Zhang Y, Breydo L, Uversky VN, Lyubchenko YL. Role of monomer arrangement in the amyloid self-assembly. Biochimica et biophysica acta. 2015;1854(3):218-28.

167.   Sandberg A, Luheshi LM, Sollvander S, Pereira de Barros T, Macao B, Knowles TP, et al. Stabilization of neurotoxic Alzheimer amyloid-beta oligomers by protein engineering. Proc Natl Acad Sci U S A. 2010;107(35):15595-600.

168.   Tjernberg LO, Tjernberg A, Bark N, Shi Y, Ruzsicska BP, Bu Z, et al. Assembling amyloid fibrils from designed structures containing a significant amyloid beta-peptide fragment. The Biochemical journal. 2002;366(Pt 1):343-51.

169.   Selivanova OM, Glyakina AV, Gorbunova EY, Mustaeva LG, Suvorina MY, Grigorashvili EI, et al. Structural model of amyloid fibrils for amyloidogenic peptide from Bgl2p-glucantransferase of S. cerevisiae cell wall and its modifying analog. New morphology of amyloid fibrils. Biochimica et biophysica acta. 2016;1864(11):1489-99.

170.   Misra P, Kodali R, Chemuru S, Kar K, Wetzel R. Rapid α-oligomer formation mediated by the Aβ C terminus initiates an amyloid assembly pathway. Nature Communications. 2016;7:12419.

171.   Dasari M, Espargaro A, Sabate R, Lopez del Amo JM, Fink U, Grelle G, et al. Bacterial inclusion bodies of Alzheimer's disease beta-amyloid peptides can be employed to study native-like aggregation intermediate states. Chembiochem. 2011;12(3):407-23.

172.   Hilbich C, Kisters-Woike B, Reed J, Masters CL, Beyreuther K. Substitutions of hydrophobic amino acids reduce the amyloidogenicity of Alzheimer's disease βA4 peptides. Journal of Molecular Biology. 1992;228(2):460-73.

173.   Wood SJ, Wetzel R, Martin JD, Hurle MR. Prolines and Aamyloidogenicity in Fragments of the Alzheimer's Peptide .beta./A4. Biochemistry. 1995;34(3):724-30.

174.   Zhang Y, Hashemi M, Lv Z, Lyubchenko YL. Self-assembly of the full-length amyloid Abeta42 protein in dimers. Nanoscale. 2016;8(45):18928-37.

175.   Hess B, Kutzner C, van der Spoel D, Lindahl E. GROMACS 4: Algorithms for Highly Efficient, Load-Balanced, and Scalable Molecular Simulation. J Chem Theory Comput. 2008;4(3):435-47.

176.   Reddy G, Straub JE, Thirumalai D. Dynamics of locking of peptides onto growing amyloid fibrils. Proc Natl Acad Sci USA. 2009;106(29):11948-53.

177.   Humphrey W, Dalke A, Schulten K. VMD: visual molecular dynamics. J Mol Graph Model. 1996;14(1):33-8, 27-8-33-8, 27-8.

178.   Krieger E, Vriend G. New ways to boost molecular dynamics simulations. Journal of Computational Chemistry. 2015;36(13):996-1007.

179.   Brandes U, Wagner D. Analysis and Visualization of Social Networks. In: Jünger M, Mutzel P, editors. Graph Drawing Software. Mathematics and Visualization: Springer Berlin Heidelberg; 2004. p. 321-40.

180.   Hunter JD. Matplotlib: A 2D Graphics Environment. Comput Sci Eng. 2007;9(3):90-5.

181.   Oliphant TE. Python for Scientific Computing. Comput Sci Eng. 2007;9(3):10-20.

182.   Daura X, Gademann K, Jaun B, Seebach D, van Gunsteren WF, Mark AE. Peptide Folding: When Simulation Meets Experiment. Angew Chem Int Ed Engl. 1999;38(1-2):236-40.

183.   Roche J, Shen Y, Lee JH, Ying J, Bax A. Monomeric Abeta(1-40) and Abeta(1-42) Peptides in Solution Adopt Very Similar Ramachandran Map Distributions That Closely Resemble Random Coil. Biochemistry. 2016;55(5):762-75.

184.   Tarus B, Tran TT, Nasica-Labouze J, Sterpone F, Nguyen PH, Derreumaux P. Structures of the Alzheimer's Wild-Type Abeta1-40 Dimer from Atomistic Simulations. J Phys Chem B. 2015;119(33):10478-87.

185.   Man VH, Nguyen PH, Derreumaux P. High-Resolution Structures of the Amyloid-beta 1-42 Dimers from the Comparison of Four Atomistic Force Fields. J Phys Chem B. 2017.

186.   Musiek ES, Holtzman DM. Three dimensions of the amyloid hypothesis: time, space and 'wingmen'. Nat Neurosci. 2015;18(6):800-6.

187.   Sevigny J, Chiao P, Bussiere T, Weinreb PH, Williams L, Maier M, et al. The antibody aducanumab reduces Abeta plaques in Alzheimer's disease. Nature. 2016;537(7618):50-6.

188.   Hu X, Crick SL, Bu G, Frieden C, Pappu RV, Lee JM. Amyloid seeds formed by cellular uptake, concentration, and aggregation of the amyloid-beta peptide. Proc Natl Acad Sci U S A. 2009;106(48):20324-9.

189.   Grimmer T, Riemenschneider M, Forstl H, Henriksen G, Klunk WE, Mathis CA, et al. Beta amyloid in Alzheimer's disease: increased deposition in brain is reflected in reduced concentration in cerebrospinal fluid. Biol Psychiatry. 2009;65(11):927-34.

190.   Rabe M, Soragni A, Reynolds NP, Verdes D, Liverani E, Riek R, et al. On-surface aggregation of alpha-synuclein at nanomolar concentrations results in two distinct growth mechanisms. ACS Chem Neurosci. 2013;4(3):408-17.

Chapter 8: References

191.   Banerjee S, Hashemi M, Lv Z, Maity S, Rochet JC, Lyubchenko YL. A novel pathway for amyloids self-assembly in aggregates at nanomolar concentration mediated by the interaction with surfaces. Sci Rep. 2017;7:45592.

192.   Mackerell AD, Jr., Feig M, Brooks CL, 3rd. Extending the treatment of backbone energetics in protein force fields: limitations of gas-phase quantum mechanics in reproducing protein conformational distributions in molecular dynamics simulations. J Comput Chem. 2004;25(11):1400-15.

193.   Heinz H, Suter UW. Surface structure of organoclays. Angew Chem Int Ed Engl. 2004;43(17):2239-43.

194.   Heinz H, Lin TJ, Mishra RK, Emami FS. Thermodynamically consistent force fields for the assembly of inorganic, organic, and biological nanostructures: the INTERFACE force field. Langmuir : the ACS journal of surfaces and colloids. 2013;29(6):1754-65.

195.   Jämbeck JPM, Lyubartsev AP. An Extension and Further Validation of an All-Atomistic Force Field for Biological Membranes. Journal of Chemical Theory and Computation. 2012;8(8):2938-48.

196.   Allen WJ, Lemkul JA, Bevan DR. GridMAT-MD: a grid-based membrane analysis tool for use with molecular dynamics. J Comput Chem. 2009;30(12):1952-8.

197.   Kabsch W, Sander C. Dictionary of protein secondary structure: Pattern recognition of hydrogen-bonded and geometrical features. Biopolymers. 1983;22(12):2577-637.

198.   Kucerka N, van Oosten B, Pan J, Heberle FA, Harroun TA, Katsaras J. Molecular structures of fluid phosphatidylethanolamine bilayers obtained from simulation-to-experiment comparisons and experimental scattering density profiles. J Phys Chem B. 2015;119(5):1947-56.

199.   Jacoby G, Cohen K, Barkan K, Talmon Y, Peer D, Beck R. Metastability in lipid based particles exhibits temporally deterministic and controllable behavior. Sci Rep. 2015;5:9481.

200.   Toledo JB, Shaw LM, Trojanowski JQ. Plasma amyloid beta measurements - a desired but elusive Alzheimer's disease biomarker. Alzheimers Res Ther. 2013;5(2):8.

201.   Potter R, Patterson BW, Elbert DL, Ovod V, Kasten T, Sigurdson W, et al. Increased in vivo amyloid-beta42 production, exchange, and loss in presenilin mutation carriers. Science translational medicine. 2013;5(189):189ra77.

202.   Keaney J, Walsh DM, O'Malley T, Hudson N, Crosbie DE, Loftus T, et al. Autoregulated paracellular clearance of amyloid-beta across the blood-brain barrier. Science advances. 2015;1(8):e1500472.

203.   Matsuzaki K. How do membranes initiate Alzheimer's Disease? Formation of toxic amyloid fibrils by the amyloid beta-protein on ganglioside clusters. Acc Chem Res. 2014;47(8):2397-404.

204.   Galvagnion C, Brown JW, Ouberai MM, Flagmeier P, Vendruscolo M, Buell AK, et al. Chemical properties of lipids strongly affect the kinetics of the membrane-induced aggregation of alpha-synuclein. Proc Natl Acad Sci U S A. 2016;113(26):7065-70.

205.   Grey M, Dunning CJ, Gaspar R, Grey C, Brundin P, Sparr E, et al. Acceleration of alpha-synuclein aggregation by exosomes. J Biol Chem. 2015;290(5):2969-82.

206.   Vácha R, Linse S, Lund M. Surface Effects on Aggregation Kinetics of Amyloidogenic Peptides. Journal of the American Chemical Society. 2014;136(33):11776-82.

207.   Villemagne VL, Perez KA, Pike KE, Kok WM, Rowe CC, White AR, et al. Blood-borne amyloid-beta dimer correlates with clinical markers of Alzheimer's disease. J Neurosci. 2010;30(18):6315-22.

208.   Diao J, Burre J, Vivona S, Cipriano DJ, Sharma M, Kyoung M, et al. Native alpha-synuclein induces clustering of synaptic-vesicle mimics via binding to phospholipids and synaptobrevin-2/VAMP2. Elife. 2013;2:e00592.

209.   Davidson WS, Jonas A, Clayton DF, George JM. Stabilization of alpha-synuclein secondary structure upon binding to synthetic membranes. J Biol Chem. 1998;273(16):9443-9.

210.   Venda LL, Cragg SJ, Buchman VL, Wade-Martins R. alpha-Synuclein and dopamine at the crossroads of Parkinson's disease. Trends Neurosci. 2010;33(12):559-68.

211.   Lee H-J, Choi C, Lee S-J. Membrane-bound α-synuclein has a high aggregation propensity and the ability to seed the aggregation of the cytosolic form. J Biol Chem. 2002;277:671-8.

212.   Galvagnion C, Buell AK, Meisl G, Michaels TC, Vendruscolo M, Knowles TP, et al. Lipid vesicles trigger alpha-synuclein aggregation by stimulating primary nucleation. Nat Chem Biol. 2015;11(3):229-34.

213.   Ysselstein D, Joshi M, Mishra V, Griggs AM, Asiago JM, McCabe GP, et al. Effects of impaired membrane interactions on alpha-synuclein aggregation and neurotoxicity. Neurobiology of disease. 2015;79:150-63.

214.   Wang Y, Shi M, Chung KA, Zabetian CP, Leverenz JB, Berg D, et al. Phosphorylated alpha-synuclein in Parkinson's disease. Science translational medicine. 2012;4(121):121ra20.

215.   Shlyakhtenko LS, Gall AA, Lyubchenko YL. Mica functionalization for imaging of DNA and protein-DNA complexes with atomic force microscopy. Methods Mol Biol. 2013;931:295-312.

216.   de Jong DH, Singh G, Bennett WF, Arnarez C, Wassenaar TA, Schafer LV, et al. Improved Parameters for the Martini Coarse-Grained Protein Force Field. J Chem Theory Comput. 2013;9(1):687-97.

217.   Yesylevskyy SO, Schafer LV, Sengupta D, Marrink SJ. Polarizable water model for the coarse-grained MARTINI force field. PLoS Comput Biol. 2010;6(6):e1000810.

218.   Abraham MJ, Murtola T, Schulz R, Páll S, Smith JC, Hess B, et al. GROMACS: High performance molecular simulations through multi-level parallelism from laptops to supercomputers. SoftwareX. 2015;1–2:19-25.

219.   Pfefferkorn CM, Jiang Z, Lee JC. Biophysics of alpha-synuclein membrane interactions. Biochimica et biophysica acta. 2012;1818(2):162-71.

220.   Fusco G, De Simone A, Gopinath T, Vostrikov V, Vendruscolo M, Dobson CM, et al. Direct observation of the three regions in alpha-synuclein that determine its membrane-bound behaviour. Nature communications. 2014;5:3827.

221.   Jo E, McLaurin J, Yip CM, St George-Hyslop P, Fraser PE. alpha-Synuclein membrane interactions and lipid specificity. The Journal of biological chemistry. 2000;275(44):34328-34.

222.   Yip CM, McLaurin J. Amyloid-beta peptide assembly: a critical step in fibrillogenesis and membrane disruption. Biophysical journal. 2001;80(3):1359-71.

223.   Yip CM, Darabie AA, McLaurin J. Abeta42-peptide assembly on lipid bilayers. Journal of molecular biology. 2002;318(1):97-107.

224.   Quist A, Doudevski I, Lin H, Azimova R, Ng D, Frangione B, et al. Amyloid ion channels: a common structural link for protein-misfolding disease. Proceedings of the National Academy of Sciences of the United States of America. 2005;102(30):10427-32.

225.   Stockl MT, Zijlstra N, Subramaniam V. alpha-Synuclein oligomers: an amyloid pore? Insights into mechanisms of alpha-synuclein oligomer-lipid interactions. Mol Neurobiol. 2013;47(2):613-21.

226.   Ouberai MM, Wang J, Swann MJ, Galvagnion C, Guilliams T, Dobson CM, et al. alpha-Synuclein senses lipid packing defects and induces lateral expansion of lipids leading to membrane remodeling. The Journal of biological chemistry. 2013;288(29):20883-95.

227.   Chaudhary H, Iyer A, Subramaniam V, Claessens MM. alpha-Synuclein Oligomers Stabilize Pre-Existing Defects in Supported Bilayers and Propagate Membrane Damage in a Fractal-Like Pattern. Langmuir : the ACS journal of surfaces and colloids. 2016;32(45):11827-36.

228.   Bousset L, Pieri L, Ruiz-Arlandis G, Gath J, Jensen PH, Habenstein B, et al. Structural and functional characterization of two alpha-synuclein strains. Nat Commun. 2013;4:2575.

229.   Giusto NM, Salvador GA, Castagnet PI, Pasquaré SJ, Ilincheta de Boschero MG. Age-Associated Changes in Central Nervous System Glycerolipid Composition and Metabolism. Neurochemical Research. 2002;27(11):1513-23.

230.   Riekkinen P, Rinne UK, Pelliniemi T, Sonninen V. Interaction between dopamine and phospholipids: Studies of the substantia nigra in parkinson disease patients. Archives of Neurology. 1975;32(1):25-7.

231.   Ysselstein D, Dehay B, Costantino IM, McCabe GP, Frosch MP, George JM, et al. Endosulfine-alpha inhibits membrane-induced alpha-synuclein aggregation and protects against alpha-synuclein neurotoxicity. Acta Neuropathol Commun. 2017;5(1):3.

232.   Kasten M, Klein C. The many faces of alpha-synuclein mutations. Mov Disord. 2013;28(6):697-701.

233.   Luheshi LM, Tartaglia GG, Brorsson AC, Pawar AP, Watson IE, Chiti F, et al. Systematic in vivo analysis of the intrinsic determinants of amyloid Beta pathogenicity. PLoS Biol. 2007;5(11):e290.

234.   van Meer G, Voelker DR, Feigenson GW. Membrane lipids: where they are and how they behave. Nat Rev Mol Cell Biol. 2008;9(2):112-24.